Title
MECHANICAL AND TRIBOLOGICAL PROPERTIES OF SKIN STUDIED BY MICROSCALE INDENTATION AND SCRATCHING TECHNIQUES

Author
Jee, Taekwon

Publication Date
2013

Peer reviewed|Thesis/dissertation

Mechanical and Tribological Properties of Skin Studied by Microscale Indentation and Scratching Techniques

By

Taekwon Jee

A dissertation submitted in partial satisfaction of the requirements

for the degree of

Doctor of Philosophy

in

Engineering – Mechanical Engineering

in the

Graduate Division

of the

University of California, Berkeley

Committee in charge:

Professor Kyriakos Komvopoulos
Professor Lisa Pruitt
Professor Dorian Liepmann

Fall 2013

Mechanical and Tribological Properties of Skin Studied by Microscale Indentation and Scratching Techniques

Abstract

Mechanical and Tribological Properties of Skin Studied by Microscale Indentation and Scratching Techniques

by

Taekwon Jee

Doctor of Philosophy in Mechanical Engineering

University of California, Berkeley

Professor Kyriakos Komvopoulos, Chair

Knowledge of the mechanical response and deformation behavior of individual skin layers during microprobe penetration is of high clinical and societal importance. In this thesis, the elastic behavior of stratum corneum, viable epidermis, dermis, and whole multilayer skin were investigated by combining micro/nanoindentation and microscratching techniques. Statistical analysis shows insignificant differences in reduced elastic modulus of skin samples obtained from three different porcine breeds. The reduced elastic modulus of stratum corneum is shown to be about three orders of magnitude higher than that of dermis. For relatively shallow and deep indentation depths, skin elasticity is controlled by that of stratum corneum and dermis, respectively. Skin indentation mechanics are interpreted in the context of a layered structure model consisting of a stiff and hard layer supported by a compliant and soft substrate, derived on the basis of microscopy observations and indentation measurements.

Time-dependent deformation of porcine skin was also studied *in vitro*. The deformation behavior of stratum corneum, dermis, and whole skin tissue are examined in the context of measurements of creep strain, elastic stiffness, and viscoelastic constants obtained for different values of hold time, loading/unloading rate, and maximum indentation depth (load). It is shown that dermis viscoelasticity significantly affects the time-dependent deformation of skin up to a critical indentation depth (load) beyond which, the viscoelastic behavior of skin is controlled by the outermost hard epidermis, particularly stratum corneum. A conceptual deformation model that explains skin viscoelastic behavior under constant load (creep) and zero load (stress

relaxation) conditions is developed on the basis of the phenomenological observations and experimental trends of this study.

Representative friction and wear results of skin subjected to unidirectional and reciprocal (cyclic) scratching are interpreted in terms of sliding speed, normal load, and scratch cycles to illustrate the effects of stratum corneum, cellular epidermis, and dermis on the skin friction and wear characteristics. Depending on the applied normal load and scratch time (cycles) various friction mechanisms (adhesion, plowing, and squeeze film lubrication) and wear processes (surface plasticity/plowing, bulk shearing, cohesive failure, tearing, and delamination) control shear-induced skin damage. The obtained results provide insight into microscale friction and wear processes influencing the mechanical response of skin to normal and shear surface tractions.

To my wife,

Young Kyung

For her dedicated support

And

To my lovely sons,

Eun and Sue

Table of Contents

List of Figures

List of figures

Acknowledgments

I would like to express my sincere appreciation to my PhD research advisor, Professor Kyriakos Komvopoulos. His unique way of teaching and mentoring my PhD study will have significant influence on my entire research career and philosophy. His assistance was not only limited to the preparation of this manuscript but also extended to problem identification, idea development, problem approach methodology, and solution seeking. He always gave me great encouragement and inspiration, especially at times when my research was not moving forward. As a dissertation committee chair, he also helped me a lot with the writing of my dissertation. His professional criticism and suggestions based on scientific arguments were critical to the improvement of my dissertation. I am grateful to him for his dedication and support throughout my PhD studies at UC Berkeley. I also thank my dissertation committee members, Professor Lisa A. Pruitt and Professor Dorian Liepmann, for their proofreading of my thesis and helpful suggestions.

I would also like to thank my PhD qualifying exam committee, Professor Hari Dharan, Professor David A. Dornfeld, Professor Zi Q. Qiu, and Professor Junquao Wu. Their helpful suggestions and criticism were invaluable to my PhD research. Many thanks are due to Dr. Youngho Seo and Dong W. Gao from the School of Medicine, University of California, San Francisco, for the donation of the porcine samples, Professor Song Li and Falei Yuan from the Bioengineering Department, University of California, Berkeley, for helpful discussions and assistance in the staining of the porcine samples, respectively, and Bruker (Campbell, CA) for the donation of the capacitance displacement sensor. Special thanks to all of my laboratory colleagues for their helpful discussions on several aspects of my research.

In addition, I also wish to express my appreciation to Intel Co., Center for Information Technology Research in the Interest of Society (CITRIS), and Department of Mechanical Engineering for providing funding for my PhD studies. It would have been impossible to continue my PhD study without this financial support.

Finally, I would like to express my most gratitude to my family, my wife Young Kyung Kim, my older son Eun Hyeok Jee, my younger son David (Sue Hyeok) Jee, my father Kukhwan Jee, my mother Hyesuk Kim, my father-in-law Byungyun Kim, my mother-in-law Myunghee Lee, my brother Ilkwon Jee, and my sister Myunghee Jee, for their dedicated support, encouragement, and sincere love. I also thank my Mokjang member, Taeho Um, Youngju Jun, Dan Kang, Kwisook Lee, John Kim, and Allicia Kim, for their pray and Christian fellowship. Many thanks to all members of the Korean Emmanuel Presbyterian Church. Special thanks to SALT, the Bible study group, especially Peter Song, Hyunjoon Shim, Taeksoon Lee, Hyunjin Moon, Younghwan Chang, and Eunpa Kim for their pray and Christian fellowship. Above all, I thank God and Jesus Christ, who makes my dreams come true again.

Chapter 1. Introduction

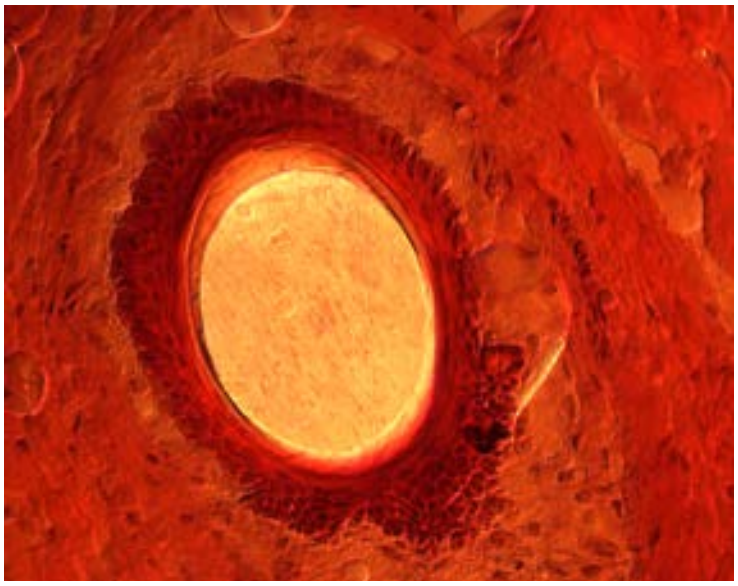

Chapter Opening Photo: In-plane view image of a hair follicle (American Yorkshire skin sample) captured with an optical microscope at 40× magnification. Hematoxylin and eosin (H&E) staining was used for histology analysis. The base of a hair follicle is located in the dermis layer. Surrounding cells near the hair are sebaceous glands, which are responsible for lubrication and waterproof of the skin and hair.

Biomechanics is the discipline of applied mechanics concerned with the structure and function of biological systems, such as humans, animals, and plants. In vertebrates, skin is of great importance in the field of biomechanics because is the outmost and largest organ. Skin interacts with many different outside objects in everyday life – some are positive (necessary) contact events whereas others are negative (unwanted) contact events. For example, gentle touching of the hands and faces of mammals is usually interpreted as friendly expression and affection. Tool handling is a required contact event for productive human life. Alternatively, hand or tool smashing

and violent claw or nail scratching are negative contact events because they result in damage of the skin and inside organs. Virus or bacteria intrusion through skin openings represents undesirable contact events for the vertebrates. Thus, the study of skin in the biomechanics field is of critical importance because it is closely linked to everyday life activity.

In this chapter, the motivation of this study using microprobe-based indentation and scratching technique is presented. A brief background of the human skin structure and functionality is given, followed by a discussion of previous mechanical testing methods of skin. Finally, the main objectives of this research are presented.

1.1 Motivation

Skin is the soft outer layer of vertebrates and the very first protective organ encountering various outside objects. Its functional importance is not limited to the vital protection of tissue and cells against external intruders, but also to cutaneous neurovascular interactions involved in sensation and skin regeneration as well as the perception of pain, thermoregulation, dehydration, transmission of mechanical stress, and absorption of radiation (McGrath and Uitto, 2010). Maintaining the physiological conditions of skin during mechanical testing is important to accurate measurement of both skin mechanical stiffness and elasticity. However, medical or cosmetic treatments, physical or psychological trauma, and various skin diseases caused by environmental and generic conditions often lead to mechanical imbalance of the skin (McGrath and Uitto, 2010). Thus, information of the mechanical response of healthy skin under physiologically relevant conditions is indispensable to skin biomechanics and their applications.

Skin is a heterogeneous multilayered tissue composed of several different layers. Over the years, however, most studies of the mechanical properties of skin have ignored this multi-layered structure. Thus, knowledge of the mechanical, viscoelastic, and tribological properties of individual skin layers is essential for understanding the mechanical response of skin to various external factors and of high importance in many clinical and cosmetic applications, such as biomedical microdevices comprising microneedle arrays for transdermal drug delivery, blood sampling, and in situ diagnosis. Knowledge of micro/nanoscale skin penetration mechanics is critical to effective, painless, and controllable administration of medication by microneedles. Despite significant progress in the fabrication of various types of microneedles, knowledge of the mechanical response of individual skin layers during penetration is mostly empirical. Consequently, microneedle failures due to the buckling and fracture have often been encountered even before insertion in the skin (Figure 1.1, Park et al., 2009; Parker et al., 2007; Davis et al., 2004). Another example is cosmetic products, such as creams, make-up cleansing brushes, and shaving blades (Figure 1.2). Skin viscoelasticity and friction play key roles in the evaluation of cosmetic products and detection of aging (Tang and Bhushan, 2010). The effectiveness of such products to improve skin elasticity, softness, and smoothness can be

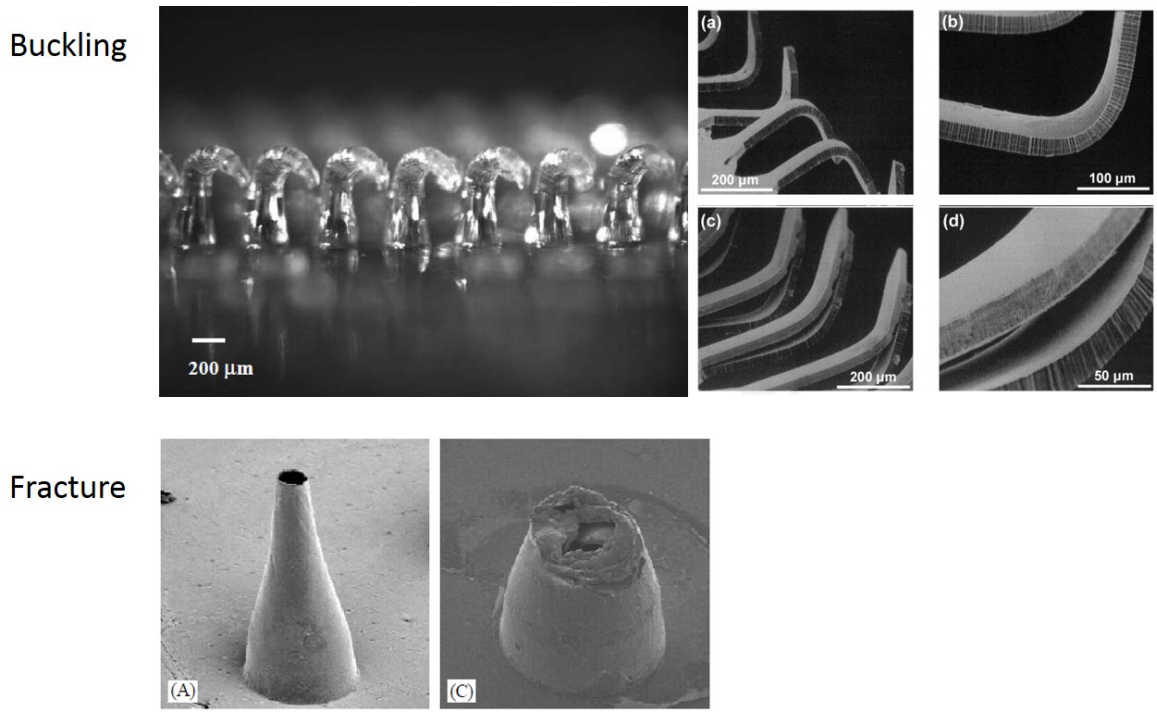

Figure 1.1 Microneedle failure due to the buckling and fracture (Park et al., 2009; Parker et al., 2007; Davis et al., 2004).

inspected using micro/nanomechanical testing methods. Another clinical example is pressure ulcer due to repeated normal or shear stress applied to the skin, causing either completely or partially restricted blood flow (Bouten et al., 2003). Therefore, studies of individual skin layer mechanical properties and friction characteristics under repeated (cyclic) stress conditions are important for understanding the mechanism of pressure ulcer of skin. Artificial skin studies, humanoid robots, high-performance clothing, and highly sensitive touch-pad devices are other possible applications that can greatly benefit from fundamental knowledge of skin mechanics (Figure 1.2).

Despite valuable insight into skin mechanical behavior obtained from previous studies, information about skin properties has been mainly obtained for the entire multi-layer skin structure. Thus, understanding of the mechanical behavior of individual skin layers is still limited. To obtain such knowledge, it is necessary to use microprobe-based methods, such as micro/nanoindentation and microscratching techniques, which can objectively measure the mechanical response of individual skin layers. Before presenting the objectives of this dissertation, it is instructive to provide a brief background of the skin structure and functions as well as an overview of previous testing methods of skin.

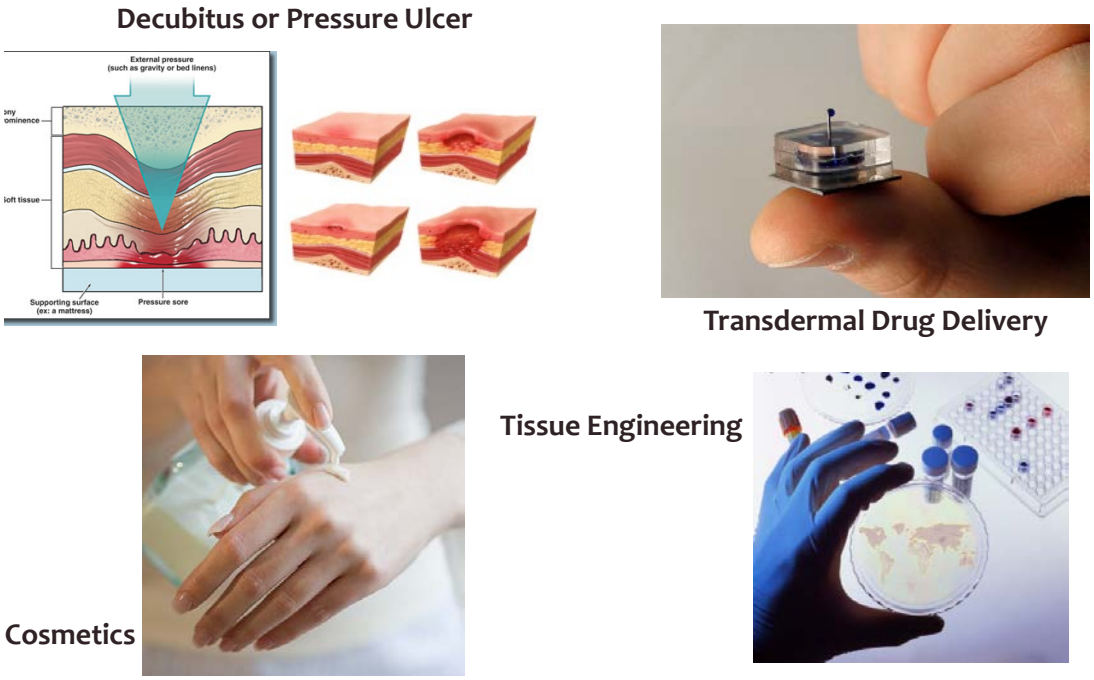

Figure 1.2 Applications for skin mechanics study – pressure ulcer (top left), transdermal drug delivery (top right), cosmetic product (bottom left), and tissue engineering (bottom right). Licensed images paid by the author.

1.2 Overview of skin structure and functions

Aside from teeth, cornea, hair, and nails, all human surfaces consist of epithelial tissue. The outer epithelial layer (epidermis), commonly referred to as the skin, is the largest organ of the human body, providing vital protection to tissue and cells against external intruders, such as bacteria, virus, and fungi, and preventing the loss of water (McGrath and Uitto, 2010; Archer, 2010). Other critical functional properties of the skin include body temperature regulation, transmission of mechanical stresses, and absorption of radiation. Skin consists of multiple layers of connective tissues and is well organized in the through-thickness direction. Depending on the body location, human skin may exhibit different thickness and function. One example is the hairy skin, characterized by the presence of many hair follicles, of the arms, legs, and head that regulates temperature and humidity. In contrast, the skin in inward or backward sites is usually hairless and thinner. Thicker and wrinkled skin can be found on the palms and the soles of the feet.

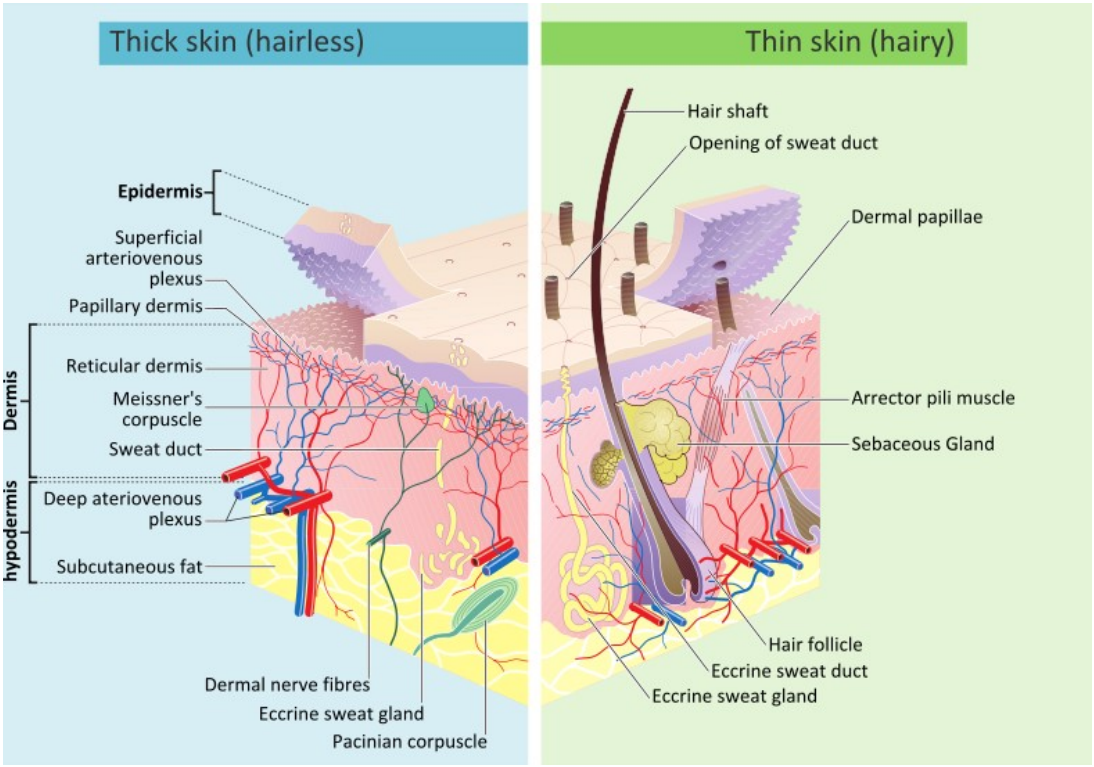

Figure 1.3 Schematics of skin layer without hair (left) and with hair (right). Courtesy of Wikimedia Commons.

Skin provides flexibility and mobility to the joints. The thinnest skin in the human body is under the eyes and around the eyelids.

Skin possesses a multilayered structure consisting of the epidermis, dermis, and hypodermis (Figure 1.3). Epidermis (~100 µm thick) is the main physical barrier and its protective and impermeable (or selectively permeable) properties are controlled by the hard stratum corneum (10–20 µm thick) surface layer mainly consisting of dead cells. The compact tissue of viable epidermis is relatively stronger than any other soft tissue and provides continuous replenishment to the aging stratum corneum (Archer, 2010). Dermis (0.5–5 mm thick) is a highly elastic matrix of high water capacity containing mechanoreceptor and nerve ends, including blood vessels, sweat glands, and hair follicles. Hypodermis is a fatty layer of several millimeters in thickness, providing insulation and restoring energy between the dermis and the muscles (McGrath and Uitto, 2010).

1.2.1 Epidermis

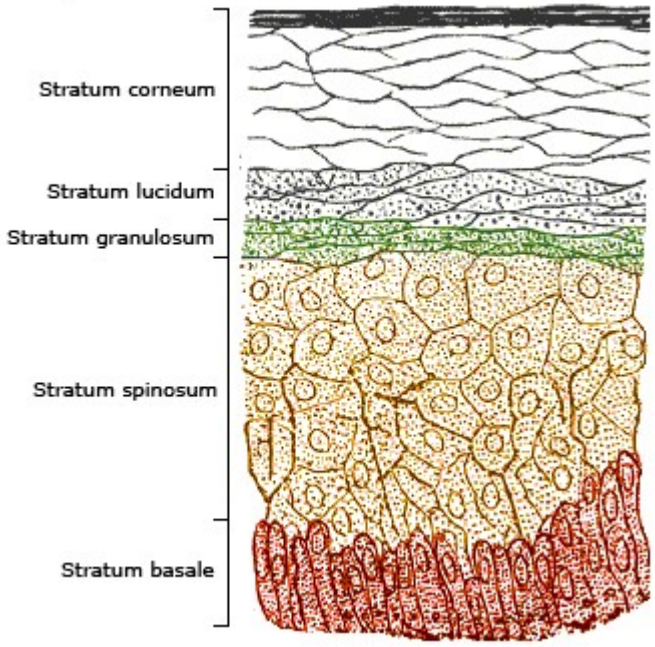

Figure 1.4 Schematic illustration of epidermis (Clemente, 1985).

Epidermis is mainly composed of keratinocytes and its thickness is normally between 50 and 100 μm. Keratin and filaggrin comprise 80–90% of the epidermis mass. Epidermis exhibits a layered structure comprising a thin and hard surface layer consisting of dead cells arranged in a brick-mortar structure of flattened corneocytes filled with keratin (bricks) and surrounded by lipids (mortar) (Barry, 1991), known as the stratum corneum, three viscoelastic layers of gradually decreasing density, mostly consisting of living keratinocytes (granulosum, lucidum, and spinosum stratum), collectively known as the cellular (viable) epidermis, and a basal layer where cells differentiate before advancing into the epidermis. (Figure 1.4) Stratum corneum is highly insoluble and its stratified structure is mostly responsible for the stiffness exhibited by the epidermis. Its cells (corneocytes) are devoid of nuclei and cytoplasmic organelles. Other cells in the epidermis are melanocytes, Langerhans' cells, and Merkel cells. Melanocytes are distributed cells of melanin pigment in melanosomes that control skin color. The size and number of melanosomes can affect skin color. The key role of Langerhans' cells is the adaptive immune response of skin. Merkel cells mainly acts as mechanosensory receptors in response to skin contact. Development of tissue from the basal layer to the stratum corneum takes about 30 days, but can be accelerated in diseased skin (e.g., psoriasis).

1.2.2 Dermal-epidermal junction

Adhesion between the viable epidermis and dermis is controlled by a complex network of proteins and glycoproteins. Besides adhesion, the dermal-epidermal junction is responsible for cell migration as well as epithelial-mesenchymal signalling events.

1.2.3 Dermis

The dermis lies beneath the dermal-epidermal junction. It is the thickest skin layer (0.5–5 mm) and home to most of skin's structures, including sweat glands, nerve endings, and capillary loops. Dermis plays an important role in tissue deformation and recovery. It contains elastic and collagen fibrils within a significant amount of ground substance. The elasticity and strength of dermis is mainly due to elastin and collagen fibers, respectively. Ground substances include glycosaminoglycan/proteoglycan macromolecules, which play a crucial role in maintaining skin hydration and are mainly responsible for the viscous behavior of the dermis.

1.2.4 Hypodermis

The hypodermis is basically a fatty layer between the dermis and the muscles. Its thickness is normally several mm, but varies with anatomical site, age, sex, race, and nutritional status of the individual. It is mainly responsible for cushioning the body, insulation, and restoring energy.

1.3 Overview of skin mechanical testing

Skin mechanical properties have been traditionally measured with macroscopic clinical instruments. Medical and clinical studies of the mechanical properties of healthy and injured skin began several decades ago (Glaeser et al., 1965; Ridge and Wright, 1966a-c; Fry et al., 1964; Gibson et al., 1969). The most common test methods for studying the mechanical behavior of skin rely on uniaxial tension (Veronda and Westmann, 1970). Various suction tests have also been used to study in vivo skin elasticity (Grahame, 1969) and its dependence on ageing (Grahame and Holt, 1969), the role of natural tension on the mechanical behavior of skin (Alexander and Cook, 1977), the dependence of skin elastic properties on age, sex, and anatomical region (Cua et al., 1990), the effect of hydration (Auriol et al., 1993) and ageing (Leveque et al., 1980) on skin extensibility, and the influence of fluid volume changes in hemodialysis on the biophysical properties of skin (Brazzelli et al., 1994). An in vivo mechanical model of the human skin (Diridollou et al., 2000) and an analysis of the relative contributions of different skin layers to the overall mechanical behavior of human skin in vivo (Hendriks et al., 2006) have also been presented for skin subjected to suction conditions.

In addition to elastic stretching, the in vivo torsional elastic behavior of human skin has attracted significant research attention (Finlay, 1971; Sanders, 1973; Leveque et al., 1980). Several in vivo studies have been carried out to elucidate the effects of ageing,

stress, sex, and moisturizing treatment on the torsional elasticity of human skin (Agache et al., 1980; Kalis et al., 1990; Salter et al., 1993). Other techniques for measuring the mechanical properties of skin have relied on various specialized instruments, such as tonometer (Warren et al., 1991), portable extensometer (Gunner et al., 1979; Berardesca et al., 1986; Ohura et al., 1980; Sugihara et al., 1991; Khatyr et al., 2004), indenter (Peck and Glick, 1956; Dikstein et al., 1984; Falanga and Bucalo, 1993), combination of suction and ultrasounds (Diridollou et al., 1998, 2000), nondestructive compression in vivo (Bader and Bowker, 1983; Lanir et al., 1990; Falanga and Bucalo, 1993; Delalleau et al., 2006; Jachowicz et al., 2007; Pailler-Mattei et al., 2008), and gas-bearing electrodynamometer (Cooper et al., 1985).

The study of the skin friction and wear properties is further perplexed by skin viscoelasticity, which makes conventional tribology theories not applicable. Despite the important role of the tribological properties of skin on its functionality, microscale tribological studies of skin subjected to surface tractions are limited. Early studies focused on the dependence of skin friction on countersurface material are attributed to Naylor (1955) and Sulzberger et al. (1996). Comaish and Bottoms (1971) studied the effects of hydration and lubrication on skin, while Armstrong (1985), Akers (1985), and Wilkinson (1985) investigated friction-induced skin injuries. Variations in skin friction due to age, sex, and anatomical factors have also been examined (Cua et al., 1990; Elsner, 1990; Zhang & Mak, 1999). More recently, advances in measurement techniques and instrumentation have provided further insight into the tribological properties of skin. A wide range of techniques and devices have been used to measure the tribological properties of skin under different experimental settings (Adams et al., 2007; Bhushan et al., 2005; Derler et al., 2007; Kwiatkowska et al., 2009; LaTorre and Bhushan, 2005; Sivamani et al., 2003a-c; Tang and Bhushan, 2010).

Although the aforementioned studies have provided important insight into the mechanical properties of human skin, very little is known about the mechanical behavior of individual skin layers. Knowledge of the mechanical properties of skin layers is essential for understanding the overall mechanical response of skin due to various external factors. However, obtaining such knowledge requires the use of microprobe-based methods, such as micro/nanoindentation techniques, which can objectively measure the mechanical response of individual skin layers. Indentation has been used to study the elastic behavior of stratum corneum (Yuan and Verma, 2006) and epidermis (Kendall et al., 2007; Geerligs et al., 2011) and to compare the measured skin properties with those of artificial skin models (Jachowicz et al., 2007). However, the former investigations were only focused on measuring the properties of either an individual skin layer or whole skin and did not provide statistical or quantitative analysis of the measured properties.

1.4 Objectives

The literature survey suggests that it is imperative to employ microprobe-based methods

of high spatial resolution capable of providing unbiased measurements of the mechanical properties of individual skin layers. This is not only important for obtaining insight into fundamental skin mechanics but also for developing miniaturized biomedical devices for effective transdermal drug delivery systems, blood sampling, and in situ diagnosis. However, understanding of surface interactions between such microdevices and skin tissue is sparse, particularly at the skin/device interaction scale.

The first objective of this study is to bridge the gap of knowledge in skin mechanics by examining the mechanical behavior of individual skin layers using micro/nanoscale indentation techniques and identifying the contribution of individual skin layers to the overall mechanical behavior of skin.

The second main objective is to elucidate the viscoelastic behavior of skin in the light of results obtained with micro/nanoindentation techniques and to identify the effect of individual layer constituents on the overall viscoelastic response of skin. Time-dependent deformation results yielding information about the elastic stiffness and viscoelastic parameters of the epidermis, dermis, and whole porcine skin are presented for a wide range of loading/unloading rate, hold time, depth rate (indentation speed), and maximum depth (load). These measurements combined with histology results provide new insight into time-dependent deformation intricacies of skin.

A third principal objective is the study of the dependence of deformation and tribological properties of skin on principal skin-layer constituents using a microprobe-based testing protocol which can provide insight into through-thickness variations of skin mechanical and tribological properties. To accomplish this objective, a special micromechanical testing apparatus equipped with calibrated force and displacement sensors was used to examine the response of skin to various loads applied by a diamond-coated tip. Skin friction is discussed in the context of experimental results obtained for varying sliding speed and constant, gradually increasing, or cyclic applied normal load. Information about depth-dependent deformation behavior of skin is extracted from cross-sectional histology results.

Chapter 2. Basic Contact Mechanics and Friction Theories

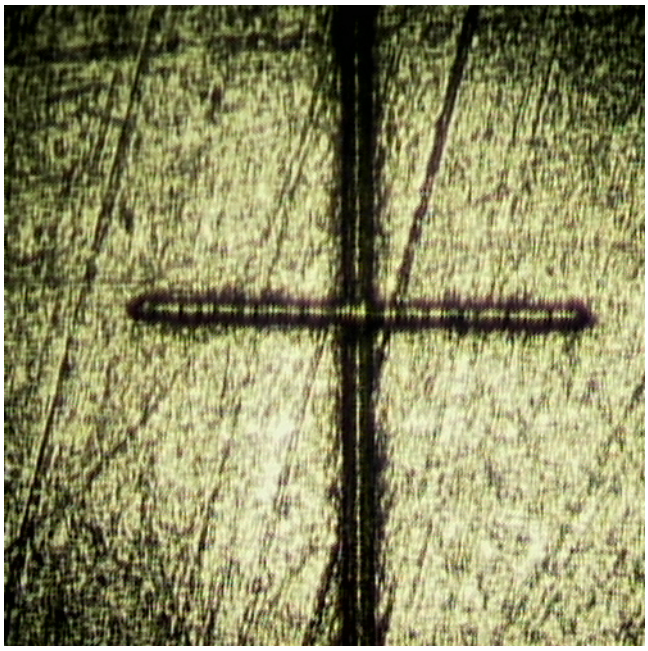

Chapter Opening Photo: Micro/nanoindentation and microscratching tests are common methods for measuring the mechanical and tribological properties of bulk and thin-film materials under compressive loads. The image shows scratch marks on an ultra-high molecular weight polyethylene (UHMWPE) surface produced during friction measurement with the microscratching technique. The high impact resistance, toughness, and biocompatibility make UHMWPE a desirable material for orthopaedic and spine implants.

Basic contact mechanics and friction theories used in the research of this dissertation are summarized in this chapter. Special emphasis is given on spherical indentation mechanics and viscoelasticity theory. In particular, time-dependent deformation analyzed by linear viscoelasticity based on the three-element model (the Kelvin-Voigt model) is presented in conjunction with a brief overview of simple friction theory. Comparative statistical tools for biological sample analysis, such as one-way analysis of variance (ANOVA), are introduced at the end of this chapter.

2.1 Contact mechanics

Contact mechanics is the field concerned with the deformation of contacting solid bodies. Knowledge of the evolution of stresses and strains in contacting elastic solids is of great importance to the undertaking material response due of indentation loading. In this section, the most common elastic contact problem, i.e., contact a rigid sphere with an elastic half-space, is discussed first.

2.1.1 Elastic contact between a rigid sphere and an elastic half-space

Normal contact between a rigid sphere and an elastic half-space is schematically shown in Figure 2.1. The contact radius *a* is related to the normal load *L* applied by the rigid sphere, sphere radius *R*, and effective elastic modulus E_{eff} by a following equation (Hertz, 1896a,b):

$$a^3 = \frac{3}{4}\frac{LR}{E_{eff}} \tag{2.1}$$

The effective elastic modulus E_{eff} is a function of the elastic modulus and Poisson's ratio of the contacting solids and is given by

$$\frac{1}{E_{eff}} = \frac{(1-\nu_1)}{E_1} + \frac{(1-\nu_2)}{E_2} \tag{2.2}$$

where E_1 and ν_1 is the elastic modulus and Poisson's ratio of the sphere and E_2 and ν_2 is the elastic modulus and Poisson's ratio of the half-space, respectively.

The displacement of the original (flat surface h at the center of contact with the rigid sphere is given by,

$$h = \frac{1}{E_{eff}}\frac{3}{2}\frac{L}{4a}\left(2 - \frac{R^2}{a^2}\right) \tag{2.3}$$

If there is a mutual approach for distant points between a rigid sphere and a deformed surface, the distance, δ, can be calculated by the following equation, (Fischer-

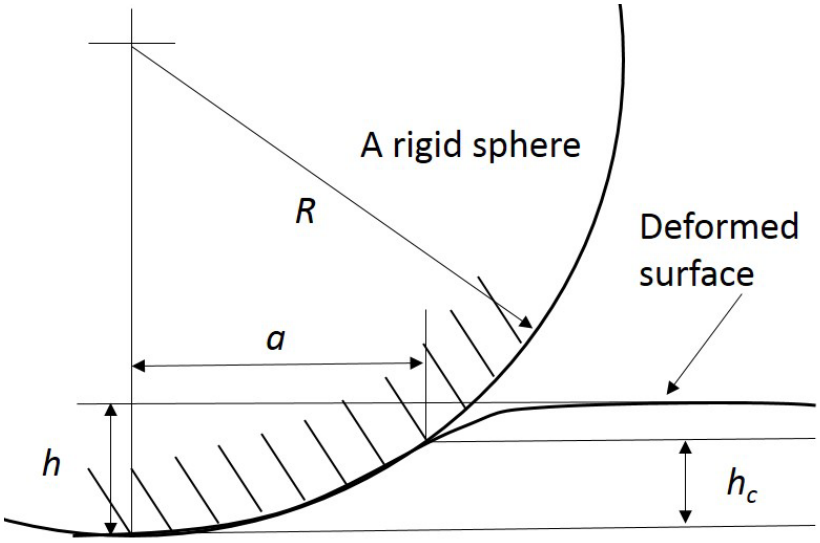

Figure 2.1 Schematic of normal contact between a rigid sphere and an elastic half-space.

Cripps, 2004)

$$\delta^3 = \left(\frac{3}{4E_{eff}}\right)^2 \frac{L^2}{R} \tag{2.4a}$$

or after replacing equation 2.3 into 2.1,

$$\delta = \frac{a^2}{R} \tag{2.4b}$$

If we consider a deformable sphere, the displacement given by equation (2.3) is identical with that given by equation (2.4a); thus equation 2.4a can be rearranged as follows,

$$L = \frac{4}{3} E_{eff} R^{1/2} h^{3/2} \tag{2.5}$$

The mean contact pressure $\bar{p}$ is defined as the ratio of the normal load *L* divided

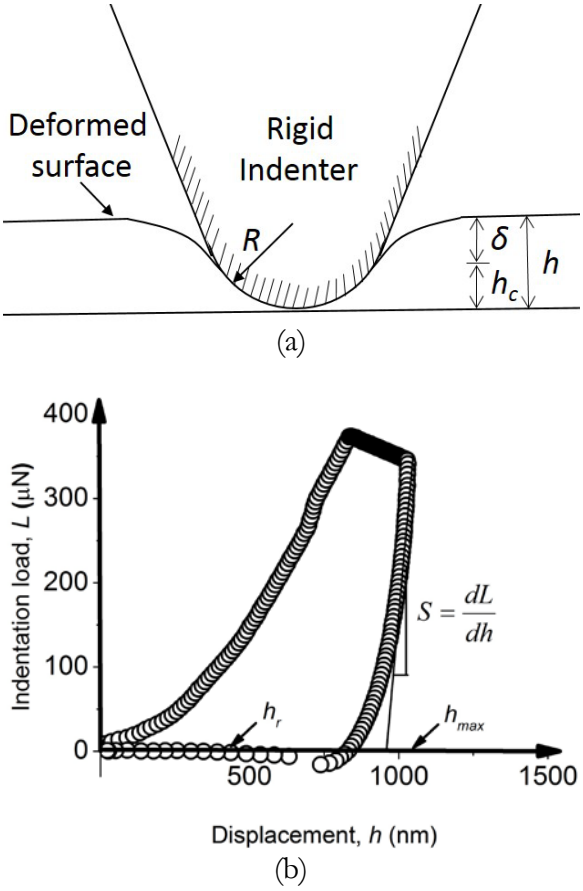

Figure 2.2 (a) Indentation of a deformable substrate by a rigid indenter, and (b) typical indentation load versus displacement response of porcine (American Yorkshire) skin obtained with a conospherical diamond nanoindenter with a radius of curvature equal to 1 μm.

by the apparent contact area, i.e.,

$$\bar{p} = \frac{L}{\pi a^2} \tag{2.6}$$

or

$$\bar{p} = \left(\frac{4E_{eff}}{3\pi}\right)\frac{a}{R} \tag{2.7}$$

The mean contact pressure is often referred to as the "indentation stress" and the

quantity *a/R* as the "indentation strain."

2.1.2 Conospherical indenter

Let's assume that there is a rigid conospherical indenter contacting a flat sample surface (Figure 2.2a). Under an applied load L, the sharp indenter sinks into the sample to a depth h. However, because of the elastic deflection of the sample surface δ, the actual indentation depth (hereafter referred to as the contact depth) is $h_c = h - \delta$. The elastic deflection of the surface is given by $\delta = \varepsilon L/S$, where ε is a constant that depends only on the indenter (tip) shape, e.g., $\varepsilon = 0.72$ and 0.75 for conical and parabolic tip, respectively (Oliver and Pharr, 1992) and S is the elastic stiffness, defined as $S = dL/dh$. Upon full unloading, partial elastic recovery of the sample by h^* yields a residual (plastic) indentation depth $h_r = h_{\max} - h^*$, where $h_{\max}$ is the maximum indentation depth (Figure 2.2b). Thus, the maximum contact depth $h_{c,\max}$ is given by,

$$h_{c,\max} = h_{\max} - \varepsilon \frac{L_{\max}}{\left(\frac{dL}{dh}\right)_{h_{\max}}} \tag{2.8}$$

The reduced elastic modulus E_r can be determined from the elastic stiffness calculated at $h_{\max}$ (Figure 2.2b), using the relation (Oliver and Pharr, 1992):

$$E_r = \frac{1}{2}\left(\frac{\pi}{A_p(h_{c,\max})}\right)^{1/2}\left(\frac{dL}{dh}\right)_{h_{\max}} \tag{2.9}$$

where A_p is a function of $h_{c,\max}$ and is referred to as the projected contact area. A polynomial function A_p can be obtained for each tip by indenting standard calibration samples of known reduced elastic modulus, i.e., quartz of E_r equal to 69.6.

The normal load during unloading is an exponential function of the indentation depth, i.e.,

$$L = C(h - h_r)^m \tag{2.10}$$

where C and m are constants determined by curve fitting the unloading force-depth data. Thus, the unloading stiffness at $h_{\max}$ is obtained as

$$\left(\frac{dL}{dh}\right)_{h_{\max}} = Cm(h_{\max} - h_r)^{m-1} \tag{2.11}$$

From Equation (2.9) and (2.11), the reduced elastic modulus is expressed as

$$E_r = \frac{1}{2} Cm \left(\frac{\pi}{A_p(h_{c,\max})} \right)^{1/2} (h_{\max} - h_r)^{m-1} \tag{2.12}$$

The indentation hardness H is defined as,

$$H = \frac{L_{\max}}{A_p(h_{c,\max})} \tag{2.13}$$

where $L_{\max}$ is the maximum load.

2.2 The three-element model of a linear viscoelasticity

Viscoelastic materials, such as polymers, metals at elevated temperature, and biological tissues, exhibit time-dependent deformation when subjected to a constant stress or strain. The term "viscoelastic" is due to the fact that such materials possess both elastic and viscous properties. In this section, the three-element model of linear viscoelasticity is used to describe the skin system because of its elastic (hard epidermis layer) and viscoelastic (soft dermis layer) characteristics.

The three-element model, shown by Figure 2.3(a), consists of a linear spring (hard epidermis) in series with a linear spring and a viscous dashpot (soft dermis) and is known as the Kelvin-Voigt element. For linear viscoelasticity, the applied stress σ can be expressed as following,

$$\sigma = \sigma_{ep} = E_{ep}\varepsilon_{ep} = E_{de}\varepsilon_{de} + c_{de}\dot{\varepsilon_{de}} = \sigma_{de} \tag{2.14}$$

where *E* is the elastic modulus, ε is the strain, *c* is the viscosity modulus, and subscripts *ep* and *de* denote epidermis and dermis, respectively. Because the overall strain is the sum of each element, that is $\varepsilon = \varepsilon_{ep} + \varepsilon_{de}$, from equation 2.14, the following relation can be obtained (Haddad, 1995):

$$(E_{ep} + E_{de})\sigma + c_{de}\dot{\sigma}(?) = E_{ep}E_{de}\varepsilon + E_{ep}c_{de}\dot{\varepsilon} \tag{2.15}$$

The creep phase is shown by Figure 2.3(b). Since $\sigma(t) = \sigma_0$ when $t > 0$, the solution for equation 2.15 is

$$\varepsilon(t) = \frac{\sigma_0}{\xi_1}\left\{\tau\left[1 - \exp(-\frac{t}{\tau})\right] + \xi_2 \exp(-\frac{t}{\tau})\right\} \tag{2.16}$$

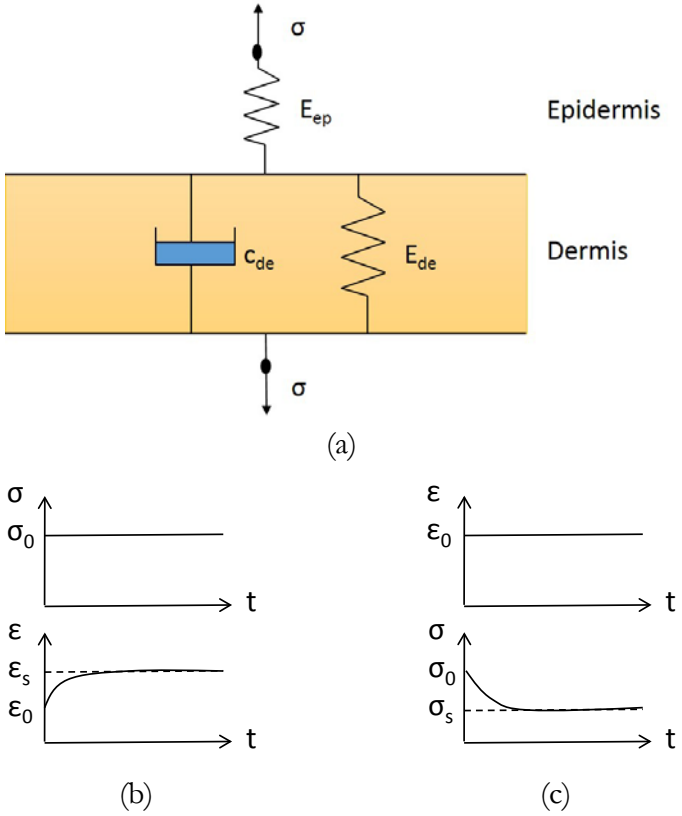

Figure 2.3 (a) Three-element viscoelasticity (Kelvin-Voigt) model (b) creep response constant stress σ_0, and (c) stress relaxation under constant strain ε_0.

where

$$\tau = \frac{c_{de}}{E_{de}}, \xi_1 = \frac{E_{ep}c_{de}}{E_{ep} + E_{de}}, \text{and } \xi_2 = \frac{c_{de}}{E_{ep} + E_{de}} \tag{2.17}$$

Here τ is a characteristic time parameter intrinsic of the creep response of the material. The initial strain ε_0 and steady-state strain ε_s are given by

$$\varepsilon_0 = \varepsilon(0) = \frac{\sigma_0}{E_{ep}} \text{ and } \varepsilon_s = \varepsilon(\infty) = \frac{\sigma_0}{E_s} \tag{2.18}$$

where

$$E_s = \frac{E_{ep}E_{de}}{E_{ep} + E_{de}} \tag{2.19}$$

The relaxation phase is shown in Figure 2.3(c). The stress relaxation response can be obtained by solving the equation 2.15 for the condition $\varepsilon(t) = \varepsilon_0$ when $t > 0$, i.e.,

$$\sigma(t) = E_s\varepsilon_0\left[1 - \exp(-\frac{t}{\lambda})\right] + \sigma_0\exp(-\frac{t}{\lambda}) \tag{2.20}$$

where

$$\lambda = \frac{c_{de}}{E_{ep} + E_{de}} \tag{2.21}$$

Here λ is a characteristic time parameter due to the relaxation response referred as the relaxation time constant. The steady state stress is given by,

$$\sigma_s = \sigma(\infty) = E_s\varepsilon_0 \tag{2.22}$$

2.3 Friction theories

According to classical friction theory of macroscopically smooth surfaces (Rabinowicz, 1995), the friction force is directly proportional to the applied normal load and independent of the apparent area of contact. The skin surface, however, is not perfectly smooth at the microscale, comprising numerous asperities spanning a wide range of length scales and residing on large-wavelength waviness (wrinkles). The study of skin friction and wear is further perplexed by skin viscoelasticity, which makes conventional tribology theories not applicable. However, it is instructive to consider classical friction theories in the presence of various environmental effects to obtain some insight into the complex skin deformation and failure mechanisms resulting from microprobe scratching.

2.3.1 Historical development of friction theories

Friction is the resistance force generated when two surfaces slide against each other. Leonardo da Vinci (1470 a.d.) was the first to observe a correlation between the normal force and the apparent area of contact. He introduced the coefficient of friction as the ratio of the friction force to the applied normal load, that is $\mu = F/L$. Amontons (1699) confirmed da Vinci's friction law and considered the implications of surface roughness in contact. Coulomb (1785) discovered that the friction force is almost proportional to the applied load and independent of the apparent contact area. He considered that the friction force in the sum of two force components – one attributed to an adhesive force

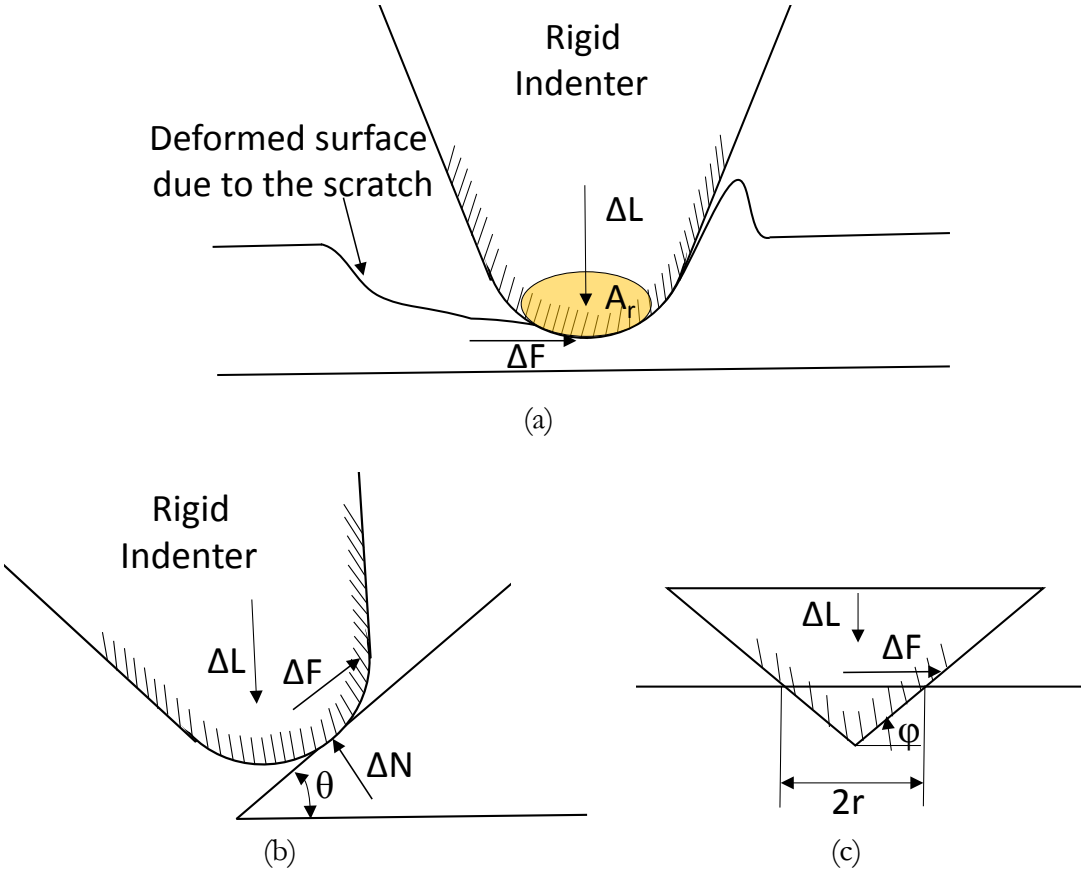

Figure 2.4 Schematics of (a) adhesion, (b) roughness, and (c) plowing friction mechanisms at the asperity level.

and another attributed to a plowing force. Leslie (1766-1830) suggested that deformation of contacting asperities and the surrounding surface would change the surface topography during sliding. Green (1955) developed and adhesion model of friction, while Shaw and Macks (1949) introduced a friction theory that accounts for the effects of adhesion, roughness, and plowing.

2.3.2 Friction due to adhesion

The friction force between two asperities due to the adhesion force component ΔF (Figure 2.4(a)) can be expressed as

$$\Delta F = A_r \tau \tag{2.23}$$

where A_r is the real contact area and τ is a constant average shear stress.

The normal force (load) ΔL is given by

$$\Delta L = A_r p \tag{2.24}$$

where p is a constant average pressure. The coefficient of friction due to adhesion μ_a is then obtained by dividing equation 2.23 by equation 2.24, i.e.,

$$\mu_a = \Delta F/\Delta L = \tau/p \tag{2.25}$$

2.3.3 Friction due to roughness

From the geometry shown in Figure 2.4(b), the friction force ΔF, normal force ΔN, and coefficient of friction due to the roughness effect μ_r can be expressed as:

$$\Delta F = \Delta L sin\theta \tag{2.26}$$

Also,

$$\Delta N = \Delta L cos\theta \tag{2.27}$$

then,

$$\mu_r = \Delta F/\Delta L = tan\theta \tag{2.28}$$

where ΔN is a normal force component on the rough surface and θ is the roughness angle.

2.3.4 Friction due to plowing

Figure 2.4(c) shows a schematic of the plowing friction process. The penetrated area swept out by the rigid asperity is

$$A_p = \frac{1}{2} \cdot 2r \cdot r tan\varphi = r^2 tan\varphi \tag{2.29}$$

where $2r$ is the diameter of projected area swept out and φ is an angle between the conical asperity and the penetrated surface. Then the friction force ΔF, normal force ΔN, and coefficient of friction due to plowing μ_p can be obtained expressed as

$$\Delta F = \pi r^2 \cdot s + r^2 tan\varphi \cdot p \tag{2.30}$$

and

$$\Delta L = \pi r^2 p \tag{2.31}$$

then,

$$\mu_p = \frac{\Delta F}{\Delta L} = \frac{\tau}{p} + \frac{tan\varphi}{\pi} \tag{2.32}$$

where τ is the average shear strength between the surfaces.

Finally, the coefficient of friction due to the all three components μ can be obtained by combining equations 2.25, 2.28, and 2.32:

$$\mu = w_a\mu_a + w_r\mu_r + w_p\mu_p = \frac{\tau}{p} + tan\theta + \frac{s}{p} + \frac{tan\varphi}{\pi} \tag{2.33}$$

where w_a, w_r, and w_p are weighing factors representing the fraction of the real contact area where adhesion, roughness, and plowing friction mechanisms are dominant.

2.4 One-way analysis of variance (ANOVA)

Analysis of variance (ANOVA) is a collection of statistical models used to analyze variations among and between groups with controlled factors. One-way ANOVA is used to examine the validity of the sample size and assumptions invoked in the statistical analysis. Assuming k levels of measured data for a given factor and representing the value of the ith observation ($i = 1, 2, \dots, n_j$) for the jth factor level ($j = 1, 2, \dots, k$) by y_{ij}, where n_j is the total number of data for the jth factor level, the mean $\bar{y}_j$ and standard deviation S_j for jth factor level are given by,

$$\bar{y}_j = \frac{1}{n_j}\sum_{i=1}^{n_j} y_{ij} \tag{2.34}$$

and

$$S_j = \left[\sum_{i=1}^{n_j} \frac{\left(y_{ij} - \bar{y}_j\right)^2}{n_j - 1}\right]^{1/2} \tag{2.35}$$

The ratio F of the mean squares of factors to the mean squares of errors is given by,

$$F = \frac{\frac{1}{k-1}\sum_{j=1}^{k} n_j\left(\bar{y}_j - \bar{y}\right)^2}{\frac{1}{n-k}\sum_{j=1}^{k}\sum_{i=1}^{n_1}\left(y_{ij} - \bar{y}_j\right)^2} \tag{2.36}$$

where n is the total number of measured data, n_1 is the number of data corresponding to the first factor level, and $\bar{y}$ is the mean of all measured data. Thus, p-values can be calculated from the F distribution as the probability satisfying the condition: $F \geq F_{(k-1,n-k,\alpha)}$, where α is the significance level (α = 0.05 in the present analysis). The null hypothesis, i.e., equal mean at all factor levels, is used to examine if the mean values for different factors (e.g., breeds or samples) are statistically different. The null hypothesis is rejected for p < 0.05.

Chapter 3. Experimental Procedures

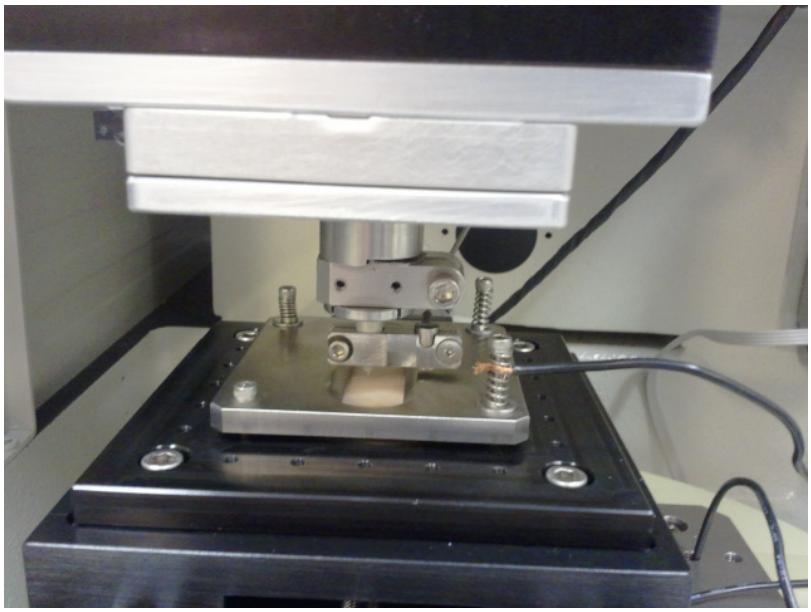

Chapter Opening Photo: Custom-made micromechanical tester used to perform indentation and sliding (scratch) tests under controlled loading and sliding speed conditions. Both normal and lateral (friction) forces were measured by a two-channel load sensor. The apparatus is equipped with two different depth sensors allowing for accurate depth measurement for both shallow and deep indentations and scratches.

Various experiments were performed to measure the mechanical, viscoelastic, and tribological properties of skin. In this chapter, the experimental setup and procedures used in these studies will be discussed. Skin sample preparation procedure is presented first. To examine subsurface deformation, cross-sectional images

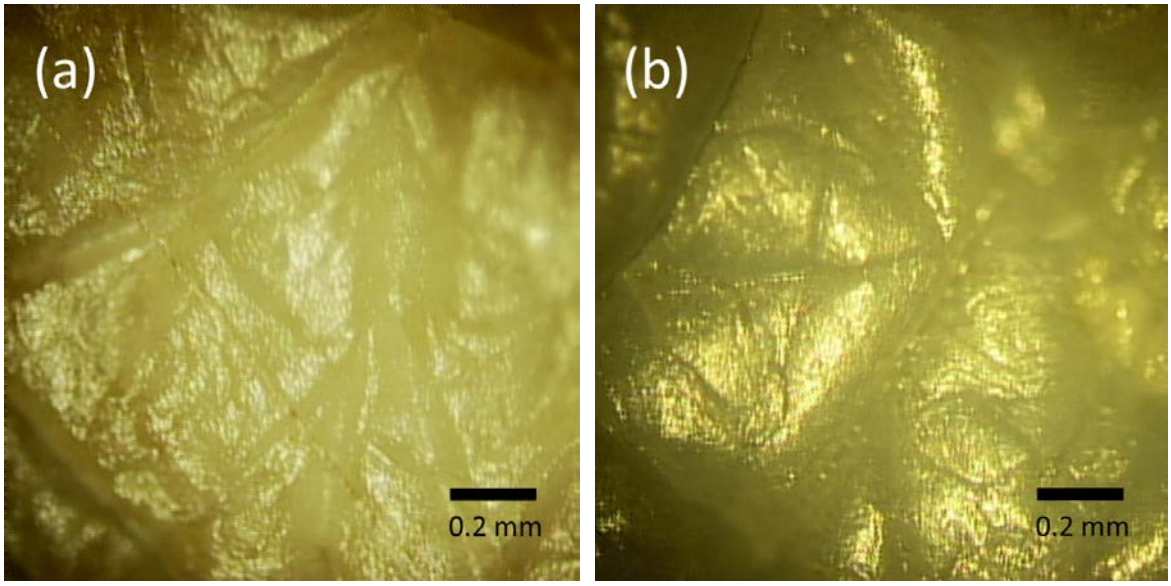

Figure 3.1 Surface morphology of (a) human and (b) porcine (American Yorkshire) skin.

of deformed skin were stained with hematoxylin and eosin (H&E) using a standard protocol for H&E staining. Nano-and micro-mechanical testing devices will be introduced including detail setup schematics. Finally, as a sample surface and cross-section inspection tool, an optical microscope having charge-coupled device (CCD) imaging unit was used.

3.1. Sample preparation

To examine the mechanical, viscoelastic, and tribological behavior of individual skin layers using micro/nanoscale indentation and scratching techniques and identify the contribution of individual skin layers to the overall mechanical behavior of skin, experiments were carried out with porcine skin samples harvested and preserved according to standard protocols. Porcine skin is appropriate for *in vitro* studies because its topology, texture, architecture, metabolic rate, and drug permeability are similar to those of human skin (Schmook et al., 2001). In addition, skin properties are not significantly affected by the lack of a physiological environment provided there is significant moisture (Agner and Serup, 1990). The morphology of porcine skin is similar to that of healthy human skin even after three days from harvesting (Figure 3.1).

Skin samples were harvested from belly parts of 4–12 months old Berkshire and

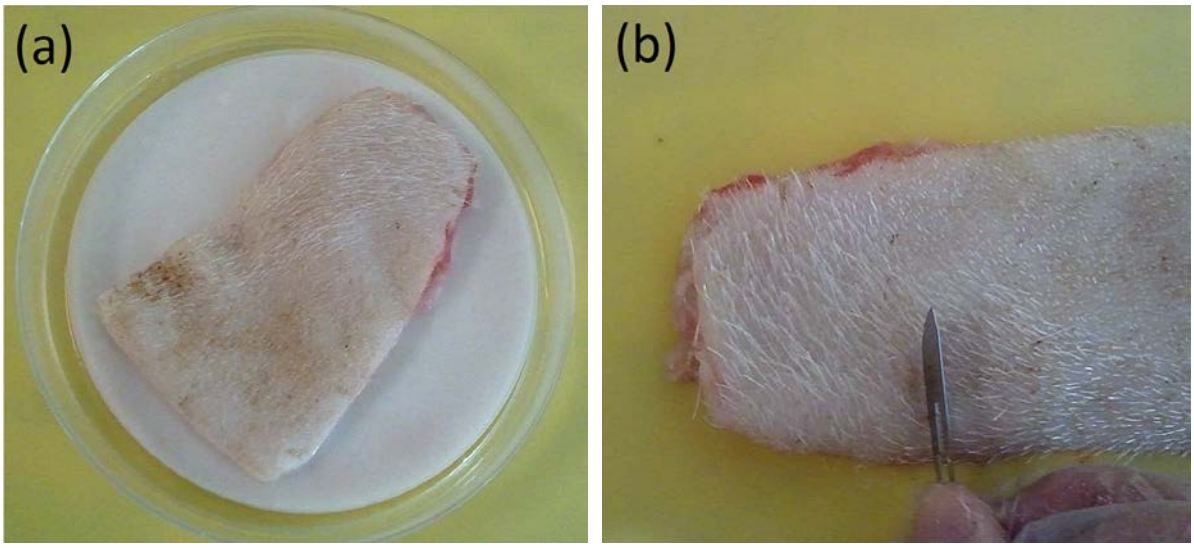

Figure 3.2 Porcine sample preparation: (a) skin samples were placed on Petri dishes covered with filter paper that had been previously soaked in 0.9% NaCl and (b) hairs were carefully removed with a surgical blade and samples were sectioned to sizes needed for testing.

Duroc-Berkshire Cross porcine breeds from a local abattoir within 3 days from sacrifice. In addition, skin samples of American Yorkshire porcine breed of similar age were obtained from the School of Medicine, University of California, San Francisco. To maintain a physiologically similar pH, the skin samples were placed on Petri dishes covered with filter paper that had been previously soaked in 0.9% NaCl or phosphate buffer saline (PBS) solution (Figure 3.2(a)). Testing was performed within 1–2 days from sample acquisition without any chemical treatment. Before testing, hairs were carefully removed with surgical blades and the samples were sectioned to the sizes required for testing (Figure 3.2(b)). To minimize sample dehydration, testing was performed within ~30 min from sample preparation in a clean-air laboratory environment.

Stratum corneum samples were prepared by removing an outer skin layer of a few tens of micrometers with a surgical knife. A chemical method of removing the stratum corneum was not used to prevent any unknown effects on the skin properties. Although the present mechanical method does not ensure the full removal of the viable epidermis, this does not present a problem because the maximum contact depth in micro/nanoindentation testing is only a few micrometers. Dermis samples were prepared by removing the hypodermis and a portion of dermis with a surgical knife and then attaching the obtained sample to Petri dishes covered with filter paper soaked in 0.9%

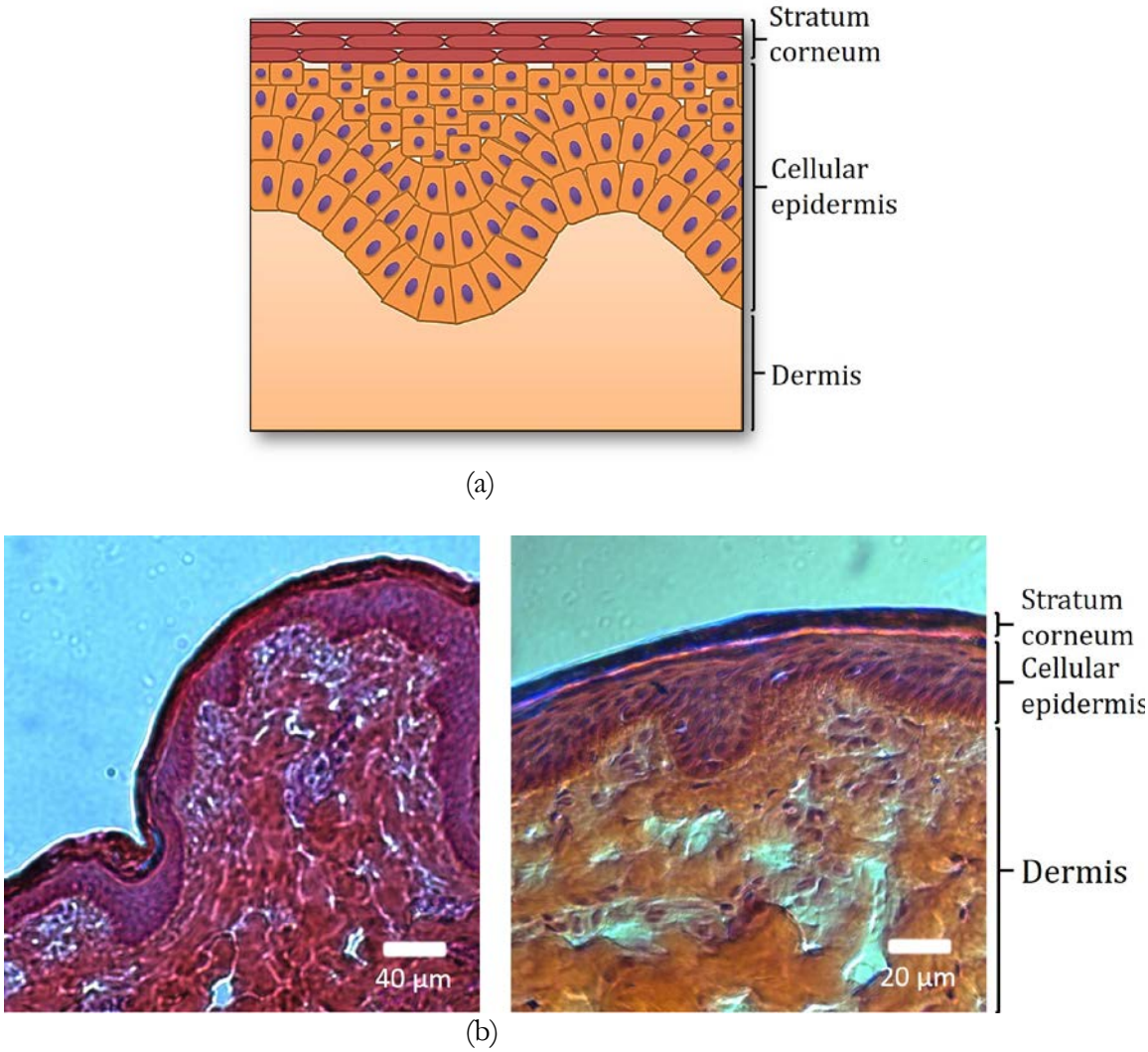

Figure 3.3 (a) Cross-sectional schematic of human skin showing the stratum corneum, cellular epidermis, and dermis layers. (b) Representative cross-sectional optical microscopy images of porcine skin (American Yorkshire) at different magnifications showing stratum corneum (~10 µm thick), viable epidermis (20–100 µm thick), and dermis (a few mm thick).

NaCl or PBS solution, with stratum corneum facing down.

Optical micrographs of the cross-sectional histology of porcine skin obtained before testing (Figure 3.3) showed overall histological features similar to those of human skin (McGrath and Uitto, 2010). The thickness of the darker layer (stratum corneum) is ~10 µm, while that of the underlying tightly packed layer (viable epidermis) varies between 20 and 100 µm. Next is the dermis with a thickness of several millimeters,

followed by the hypodermis, which is beyond the scope of this study.

3.2. Histology

For cross-sectional histology analysis, skin samples were embedded in optimal-cutting-temperature compound (TissueTek, Elkhart, IN) on dry ice and kept refrigerated at a temperature of –62 °C until testing. Subsequently, 10-µm-thick specimens were cut from the skin samples and stained with H&E following a standard protocol.

This procedure is performed with the slides in glass staining racks and the solutions in square glass staining jars/boxes.

1. Distilled H_2O: 2-3 rinses
2. Hematoxylin (Gill's 1X): 5 min
3. Tap Water: rinse slides under running tap water in staining box until the water is no longer colored. (~5 min)
4. Acid Alcohol (1% HCl in 70% ETOH): dunk 2-3 times until the sections turn pink
5. Tap Water: rinse 3-5 min
6. Ammonia water (1 mL NH_4OH in 1 L H_2O): 5-6 slow dunks; the sections should darken noticeably.
7. Tap Water: rinse 3-5 min
8. Eosin Y: 1 min
9. Tap Water: rinse slides 3-4 times under running tap water.
10. 95% EtOH: 2 min
11. 95% EtOH: 2 min
12. 95% EtOH: 2 min
13. 100% EtOH: 2 min
14. 100% EtOH: 2 min
15. 100% EtOH: 2 min
16. 50:50 Xylene/100% EtOH: 2 min
17. 100% Xylene: 2 min
18. 100% Xylene: 2 min
19. 100% Xylene: 2 min

3.3. Nano/micro-indentation and scratching experiments

Nanoindentation tests were performed with an apparatus consisting of an atomic force microscope (AFM) scanner (Nanoscope II, Digital Instruments, Santa Barbara, CA), a three-plate capacitor force-displacement transducer (Triboscope, Hysitron, Minneapolis, MN), and a detector assembly (head) that uses the AFM scanner and the software of a scanning

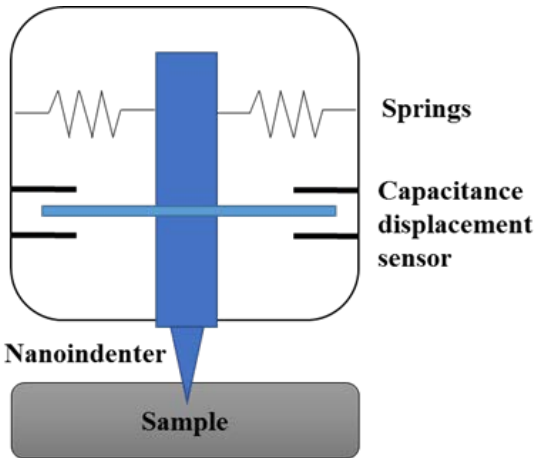

(a)

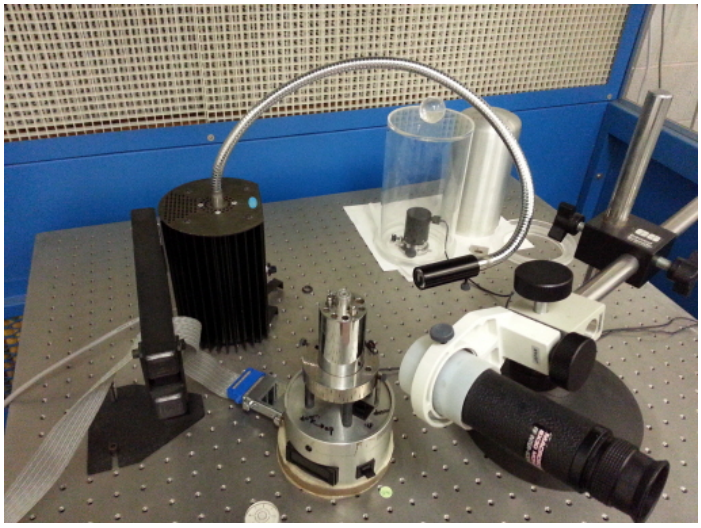

(b)

Figure 3.4 (a) Schematic and (b) photograph of nanoindentation apparatus.

tunneling microscope (Figure 3.4). The normal force exerted to the sample surface by a diamond tip attached to the middle plate of the force capacitor was generated by a voltage applied across the two outer plates and the deflection of the middle plate was

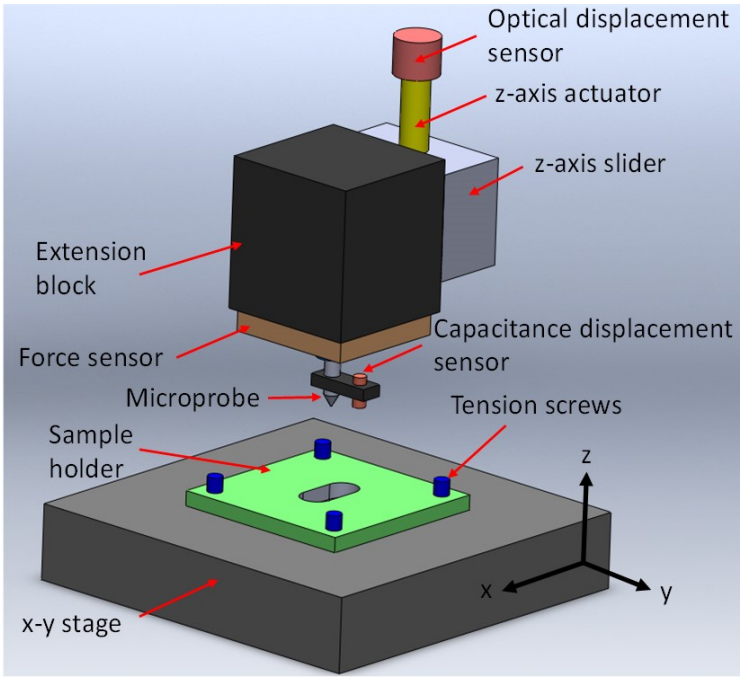

(a)

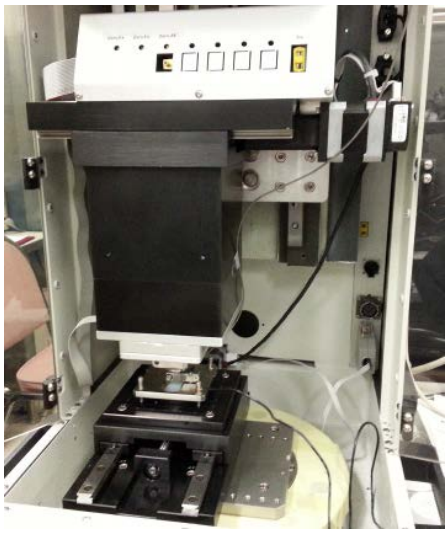

(b)

Figure 3.5 (a) Schematic and (b) photograph of microindentation apparatus.

modulated by an internal feedback loop. The change of the middle-plate position due to the force generated by the indented sample (displaced toward the tip by a piezoelectric actuator) was indirectly determined from capacitance change measurements obtained

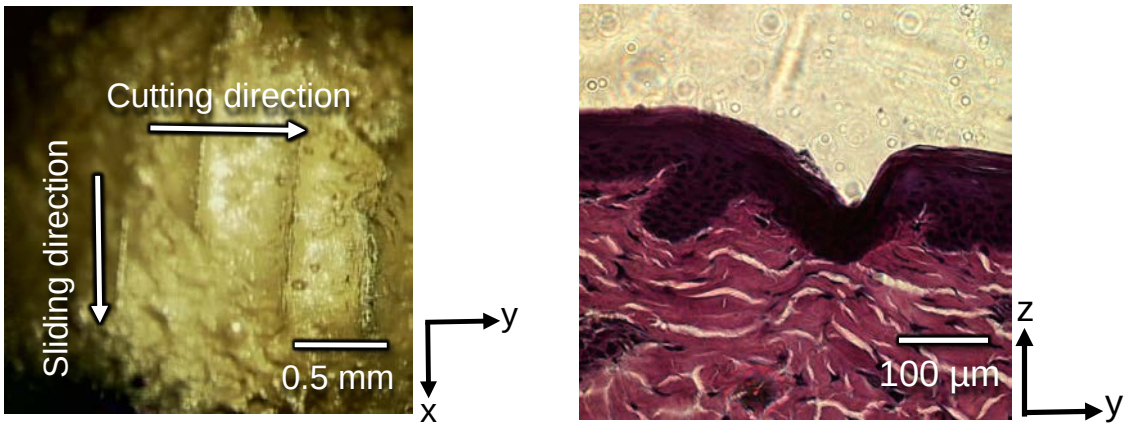

(a) (b)

Figure 3.6 (a) Optical image showing wear scars on a skin surface produced by a normal load of 20, 50, 100, and 400 mN (from left to right), including the sliding (scratching) direction and cutting direction used to obtain cross-sectional samples for histology analysis. (b) Stained cross-sectional sample showing the formation of a permanent groove on the epidermis without the removal of the stratum corneum (normal load = 50 mN).

with a high-resolution capacitance sensor. For load control, the output signal was amplified and the digital readout (acquired by a computer) was feedback to the capacitor transducer. Because of the relatively high roughness of the skin samples (the root-mean-square roughness, measured with the AFM, was found to be in the range of 200–300 nm), a conospherical diamond tip of radius of curvature equal to 1 or 20 µm attached to the middle plate of the capacitor transducer was used in all the nanoindentation experiments. To minimize surface roughness and substrate (viable epidermis/dermis) effects on the measurement of the mechanical properties of stratum corneum, the maximum contact depth was varied between 100 nm and 2 µm. A trapezoidal load profile with loading and unloading rates of 20 µN/s and hold time at maximum load fixed at 40 s was used in all nanoindentation tests.

Because of the large thickness of the dermis and skin samples, microindentation experiments were performed with an apparatus (Bruker, Campbell, CA) with a much larger *z*-range and a load sensor with 0.5 mN load resolution and 4.9 N maximum load capacity (Figure 3.5). This indentation system uses a capacitive displacement sensor to measure contact depths up to ~250 µm with 0.1 µm resolution and an optical displacement sensor to measure contact depths of a few micrometers up to several millimeters with 1 µm resolution. During testing, the skin sample was kept under a mild tensile stress by a clamp steel plate attached to the sample holder by four screws. Horizontal leveling of the sample was achieved with a level bubble. Indentation testing

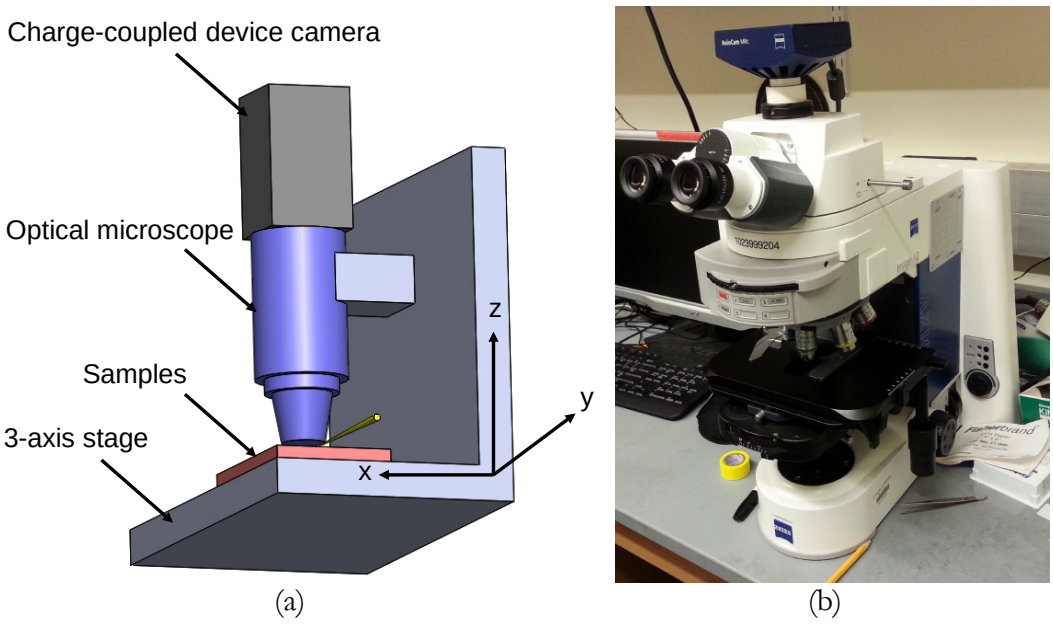

Figure 3.7 (a) Schematic and (b) photograph of an optical microscope set up.

was performed through an opening of the steel plate.

For scratch testing, the normal load was varied in the range of 20–700 mN, while the scratch length was fixed at 1 mm. Measurements of the scratch depth, normal load, friction force, and coefficient of friction were acquired *in situ* at a rate of 100 measurements/s using a data acquisition system interfaced with the experimental setup. Figures 3.6(a) and 3.6(b) show typical optical microscope images of a scratched sample and a stained cross-sectional sample, respectively. All of the cross-sectional samples used in the histology analysis were obtained by cutting the scratched samples perpendicular to the sliding direction, as shown in Figure 3.6(a).

3.4. Optical microscope with charged-coupled device camera

Tested skin surfaces and cross-sectional histology samples were observed with an optical microscope (OM) equipped with a charge-coupled device (CCD) imaging unit (Axio imager 2, Carl Zeiss, Germany) at different magnifications (Figure 3.7).

Chapter 4. The Mechanical Properties of the Skin

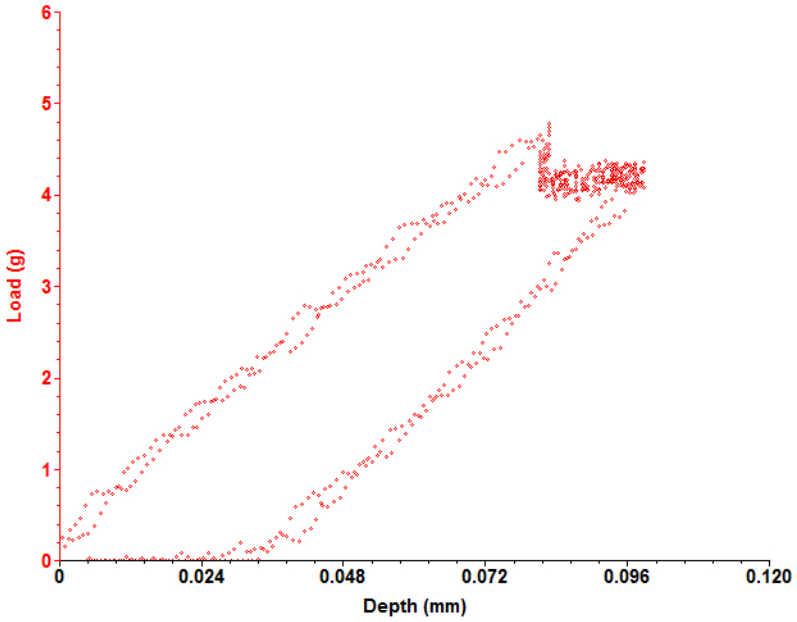

Chapter Opening Photo: Micro-indentation is the technique to measure the mechanical properties of materials, such as elastic modulus and hardness, by microprobe compression. The usually acquired data are in the form of load versus depth response and can be used to determine elastic and plastic material properties. The image on the left is a load-depth response of epidermis obtained from a microindentation test for a maximum load of 4 g.

In this chapter, results for different porcine breeds are contrasted and the effect of the mechanical properties of stratum corneum, viable epidermis, and dermis to the mechanical behavior of skin are discussed in the context of mechanical property

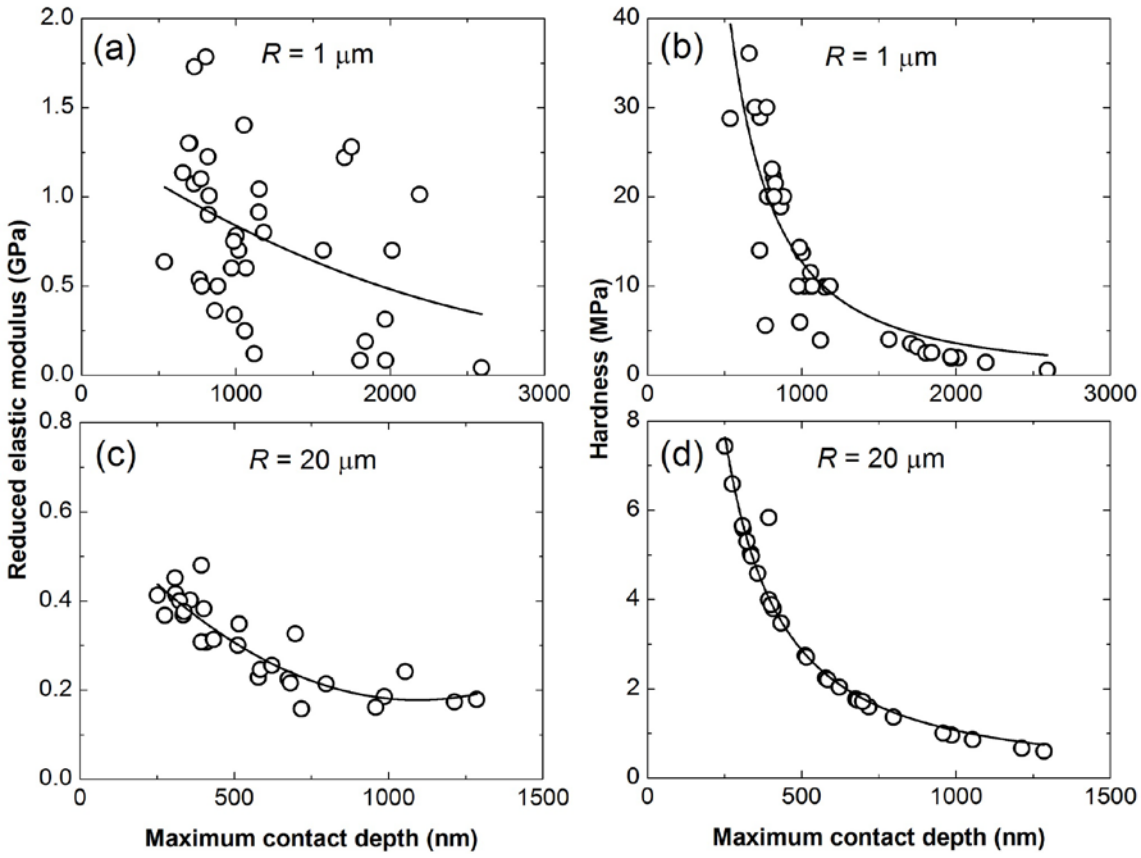

Figure 4.1 Reduced elastic modulus and hardness versus maximum contact depth for stratum corneum obtained with a conospherical diamond indenter of radius of curvature equal to (a, b) 1 μm and (c, d) 20 μm.

measurements obtained from nano/microindentation experiments performed with relatively sharp and blunt diamond tips for different maximum normal loads (maximum contact depths).

4.1 Mechanical properties of stratum corneum

Reduced elastic modulus and hardness of randomly selected skin samples show a nonlinear decrease with the increase of the maximum contact depth for both relatively sharp (1 μm radius) and blunt (20 μm radius) indenters (Figure. 4.1, ~5–10 tests/sample, ~5 samples/breed). This trend is attributed to the deformation effect of the highly

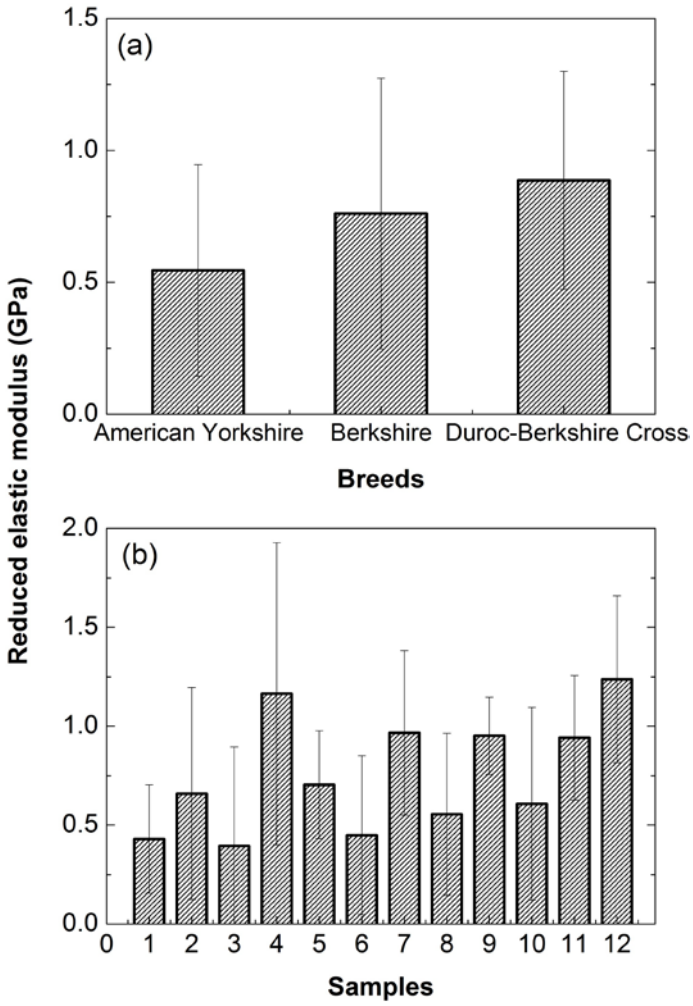

Figure 4.2 Reduced elastic modulus of stratum corneum of (a) American Yorkshire, Berkshire, and Duroc-Berkshire Cross porcine breeds and (b) randomly selected samples of different breeds.

compliant and soft viable epidermis, which becomes more significant with the increase of the contact depth. The reduced elastic modulus and hardness of stratum corneum, obtained by averaging the data in the contact depth range of 500–1000 nm to avoid the effects of the compliant viable epidermis and high surface roughness, are equal to 0.87 ± 0.42 GPa (Figure 4.1 (a)) and 15.6 ± 10 MPa (Figure 4.1 (b)), respectively. Significantly lower values of reduced elastic modulus Figure 4.1 (c)) and hardness (Figure 4.1(d)) of stratum corneum were obtained with the relatively blunt indenter due to biasing of the

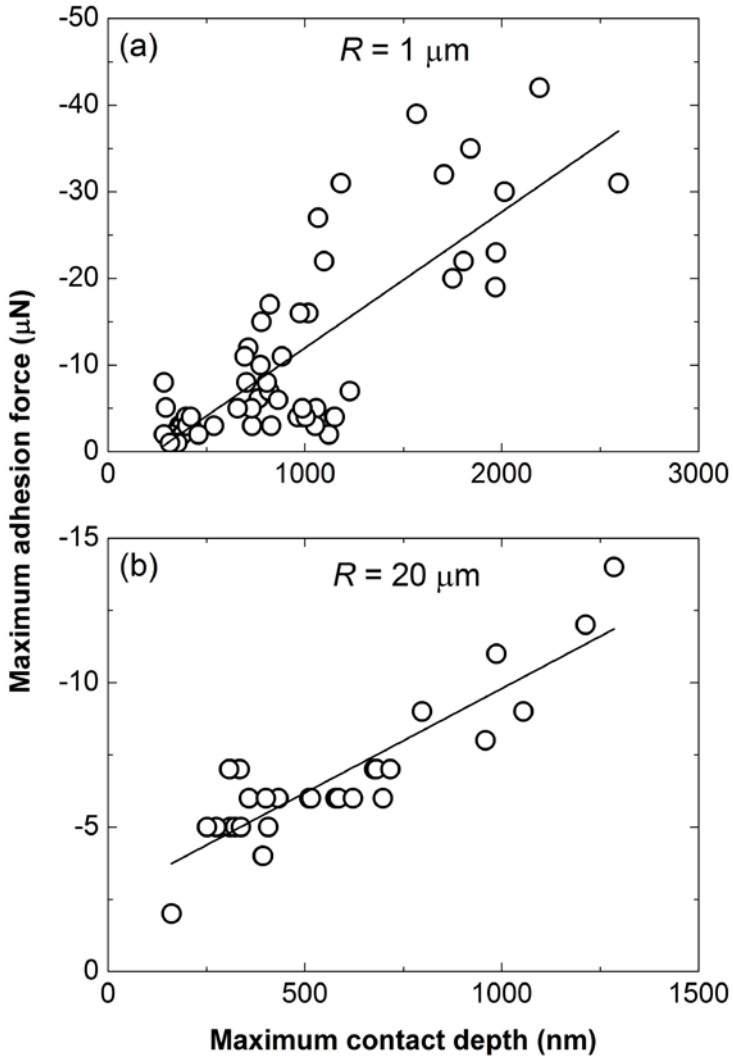

Figure 4.3 Maximum adhesion force versus maximum contact depth obtained with a conospherical diamond indenter of radius of curvature equal to (a) 1 μm and (b) 20 μm.

measurements by the deformation of the viable epidermis. However, extrapolation of the nonlinear curve fit to a contact depth of 1 μm yields a reduced elastic modulus of 0.8 GPa, which is close to the value determined with the sharp indenter. The data for contact depths >500 nm are considered to be indicative of the mechanical properties of the viable epidermis. Consequently, the reduced elastic modulus and hardness of viable epidermis, obtained by averaging the data in the contact depth range of 500–1300 nm, are equal to 0.21 ± 0.05 GPa and 1.3 ± 0.5 MPa, respectively.

Results of the reduced elastic modulus of stratum corneum of different breeds (measured with the sharp indenter for a contact depth of ~1 μm) do not show statistical differences (Figure 4.2(a), k = 3 (3 breeds), $n_j \approx 10$ (~10 samples/breed), F = 1.294, and p = 0.287). A similar observation is made for data obtained from randomly selected samples of different breeds (Figure 4.2(b), k = 12 (12 samples), $n_j \approx 4$ (~4 tests/sample), F = 1.417, and p = 0.226). These results indicate that the stratum corneum of the three breeds exhibits similar elastic properties and that the measured properties are independent of the sample selection and testing order.

4.2 Adhesion force of stratum corneum

A negative load was encountered during unloading (Figure 2.2(b)), which is attributed to the development of an adhesion force. The maximum adhesion force shows a monotonic increase with the maximum contact depth for both sharp (Figure 4.3 (a)) and blunt (Figure 4.3 (b)) indenters. This trend is attributed to the increase of contact area at the inception of surface detachment and, possibly, the exposure of a larger area of the sticky viable epidermis due to the tip penetration through the stratum corneum with the increase of the maximum contact depth. Similar to the reduced elastic modulus and hardness, the blunt nanoindenter shows much lower adhesion. This can be associated with less deformation in the stratum corneum, resulting in a larger spring-back elastic force and the significantly less (if any) exposure of the viable epidermis.

4.3 Mechanical properties of dermis

As explained earlier, the reduced elastic modulus and hardness of dermis was measured with the microindentation apparatus because the contact depth range is beyond the maximum *z*-displacement of the nanoindenter. Both the reduced elastic modulus and the hardness of dermis decrease with the increase of the maximum contact depth, attaining steady-state values of 1.91 ± 0.88 MPa and 0.85 ± 0.45 MPa, respectively, for maximum contact depth >300 μm (Figure 4.4, 7 samples, ~5 tests/sample). Similar to stratum corneum, the reduced elastic modulus of dermis for contact depth fixed at 300 μm does not show a dependence on breed type (Figure 4.5(a), k= 3 (3 breads), $n_j \approx 10$ (~10 tests/breed), F = 0.120, and p = 0.887) and sample selection or test order (Figure 4.5(b), k = 8 (8 samples), $n_j \approx 4$ (~4 tests/sample), F = 0.207, and p = 0.981).

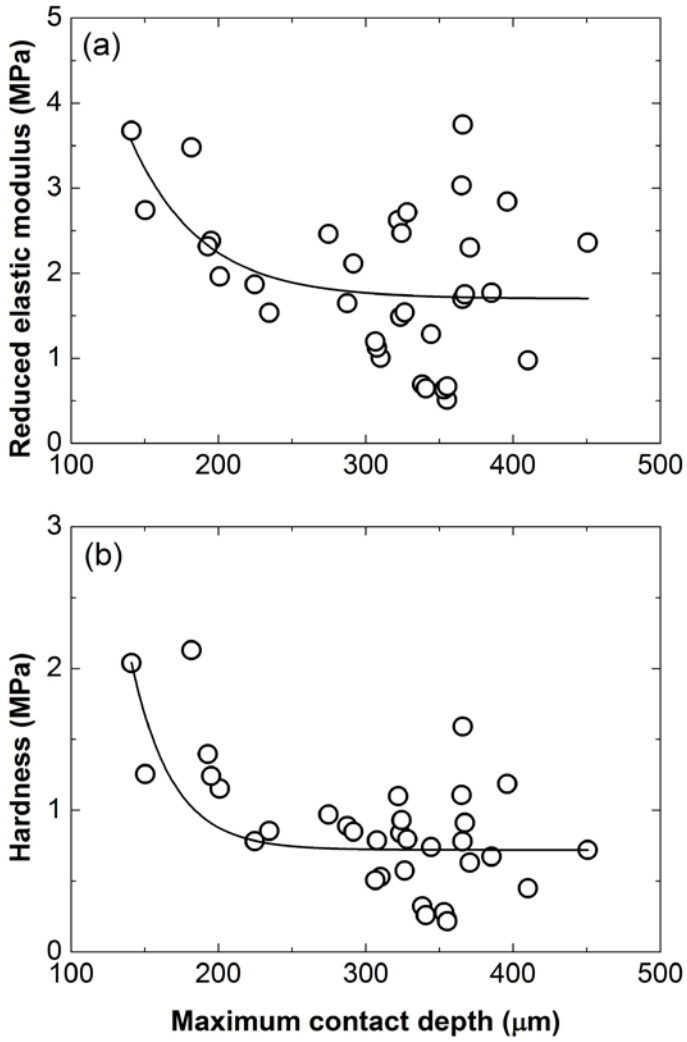

Figure 4.4 Reduced elastic modulus and hardness of dermis versus maximum contact depth obtained with a conospherical diamond indenter of radius of curvature equal to 12.5 μm.

4.4 Mechanical properties of skin

The mechanical properties of skin were also studied with the microindentation apparatus because of the large contact depth range required for these measurements. Both the reduced elastic modulus and hardness of skin sharply decrease with the increase of the maximum contact depth (Figure 4.6, ~5 tests/sample, 15 samples), reaching state-state

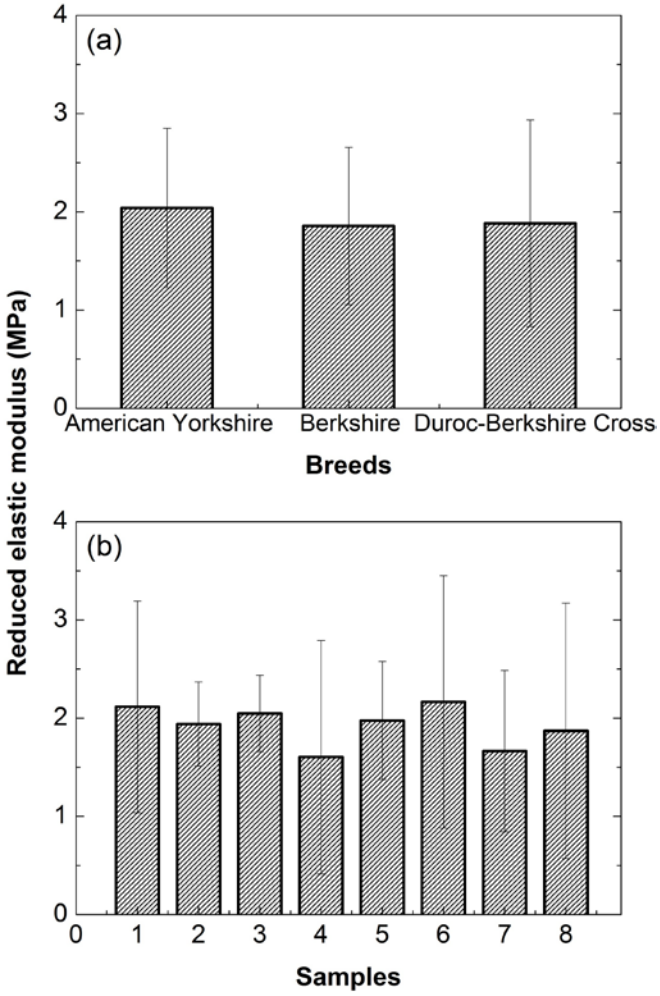

Figure 4.5 Reduced elastic modulus of dermis of (a) American Yorkshire, Berkshire, and Duroc-Berkshire Cross porcine breeds and (b) randomly selected samples of different breeds.

values of 3.77 ± 1.7 MPa and 1.43 ± 0.58 MPa, respectively, for maximum contact depth >100 µm. From a curve-fit approach, the reduced elastic modulus at a maximum contact depth equal to ~5 µm is predicted to be 0.80 GPa, which is close to that of stratum corneum (0.87 GPa), whereas the reduced elastic modulus at a maximum contact depth of ~200 µm is equal to ~2 MPa, which is close to that of dermis (1.91 MPa). Statistical analysis shows insignificant differences in reduced elastic modulus (for contact depth fixed at 70 µm) among porcine breeds (Figure 4.7(a), k= 3 (3 breeds), $n_j \approx 20$ (~20

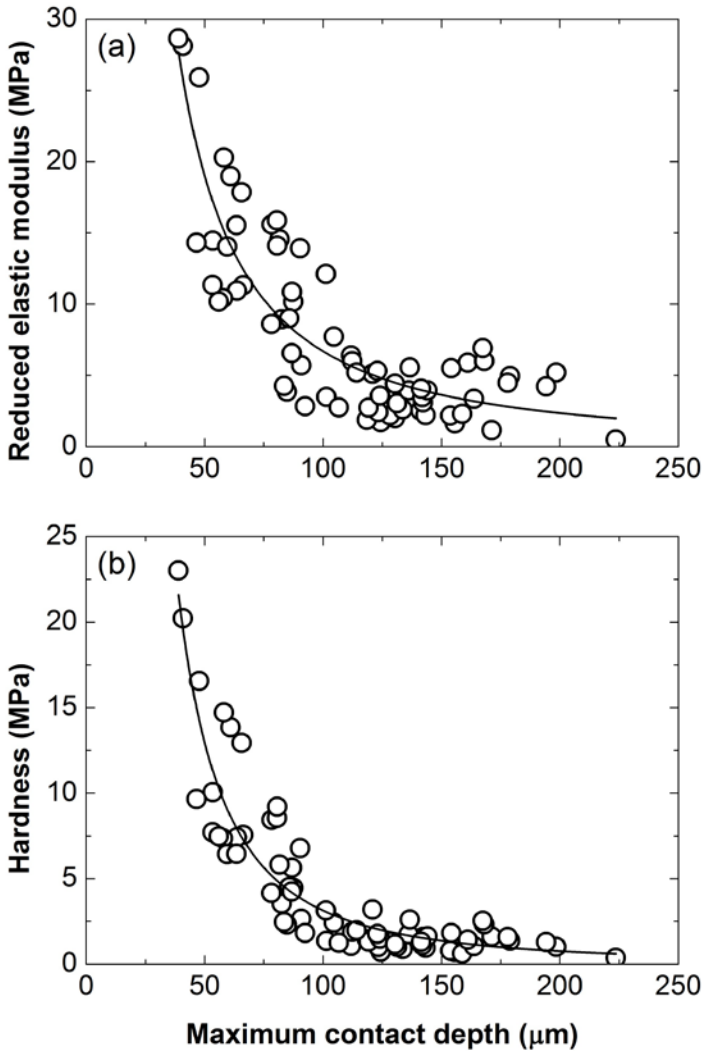

Figure 4.6 Reduced elastic modulus and hardness of skin versus maximum contact depth obtained with a conospherical diamond indenter of radius of curvature equal to 12.5 μm.

samples/breed), F = 0.131, and p = 0.88) and sample selection or test order (Figure 4.7(b), k = 15 (15 samples), $n_j \approx 5$ (~5 tests/sample), F = 0.156 and p = 0.999). However, the corresponding standard deviation (Equation (2.35)) is very high (42 and 49 for Figure 4.7(a) and 4.7(b), respectively) due to the significant scatter of these measurements.

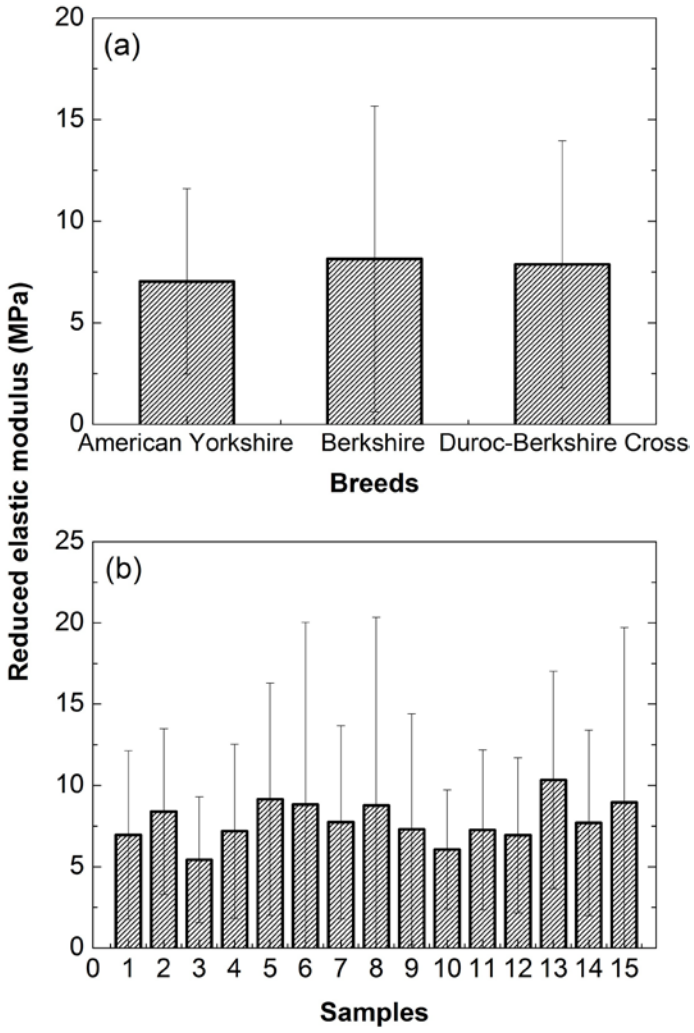

Figure 4.7 Reduced elastic modulus of skin of (a) American Yorkshire, Berkshire, and Duroc-Berkshire Cross porcine breeds and (b) randomly selected samples of different breeds.

4.5 Discussion

One-way ANOVA analysis revealed insignificant differences in the mechanical properties of stratum corneum, dermis, and skin of different porcine breeds and randomly selected samples of each breed, indicating that the measured mechanical properties were

Material	Reduced elastic modulus (GPa)	Hardness (MPa)
Stratum corneum[1]	0.87 ± 0.42	15.6 ± 10.0
Viable epidermis[2]	0.21 ± 0.05	1.30 ± 0.5
Dermis[2]	0.00191 ± 0.00088	0.85 ± 0.45
Skin[2,3]	0.00377 ± 0.0017	1.43 ± 0.58

[1]sharp indenter (R = 1 μm)
[2]blunt indenter (R = 20 μm)
[3]maximum contact depth >100 μm

Table 1. Mechanical properties of individual skin layers and whole skin obtained from nano/microindentation experiments performed with porcine samples of three different breeds.

independent of breed, sample selection, and test order. Table 1 summarizes the mechanical properties of individual layers and whole skin multilayer measured from nano/microindentation experiments, performed with relatively sharp and blunt indenters (to account for significant differences in material compliance and softness that affected the contact depth range) and indentation mechanics analysis (Equations (2.8)–(2.13)). To avoid biasing of the measurements by the high surface roughness (200–300 nm) of the skin samples, nanoindentation measurements were obtained with a sharp (1 μm radius) indenter for maximum contact depth >500 nm. Because of the less significant roughness effect on the measurements obtained with a blunt (20 μm radius) indenter, reliable measurements were obtained for a smaller range of maximum contact depth. However, these measurements were influenced by the high compliance of the viable epidermis. This problem was overcome by using a curve-fitting approach and extrapolating the fitted curve into the low range of maximum contact depth. Using this approach, the reduced elastic modulus of stratum corneum measured with the blunt indenter (0.80 GPa) was found to be very close to the direct measurement obtained with the sharp indenter (0.87 GPa). The reduced elastic modulus of stratum corneum measured in this study is in good agreement with the results of previous studies (Park and Baddiel, 1972; Nicolopoulos et

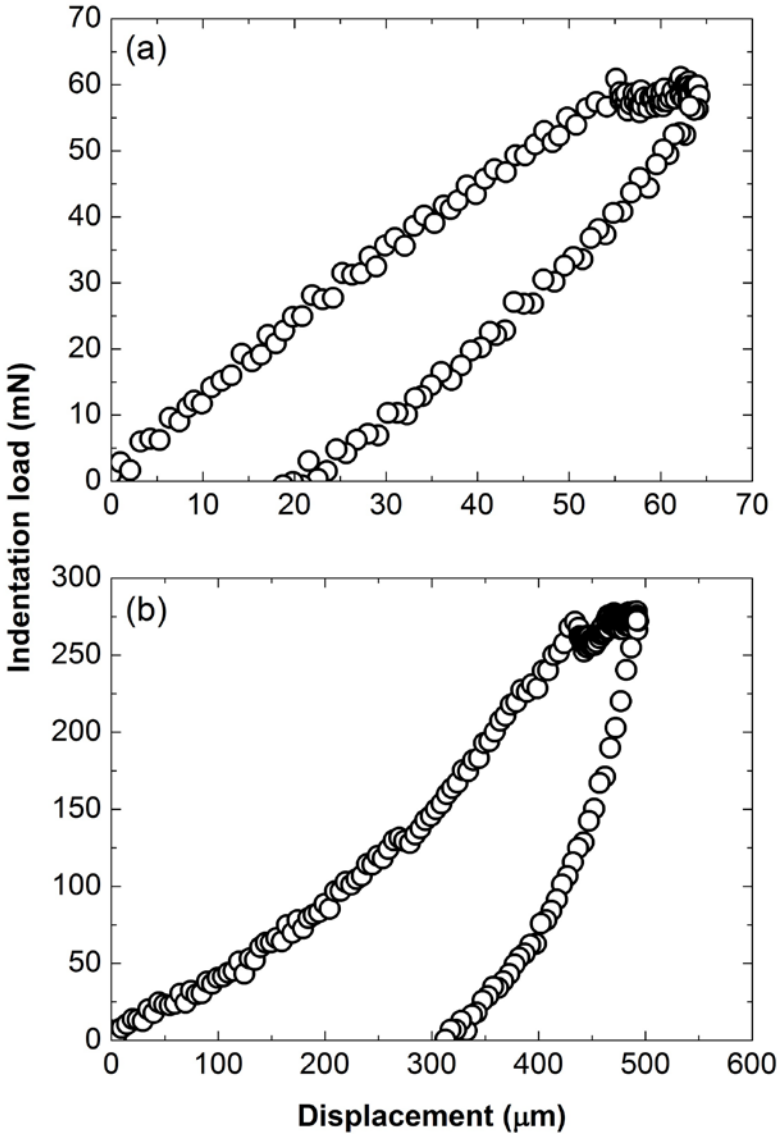

Figure 4.8 Indentation load versus displacement response of skin (American Yorkshire) obtained with a conospherical diamond indenter of radius of curvature equal to 12.5 μm for a maximum displacement equal to (a) 60 and (b) 500 μm.

al., 1998). Using the same curve-fitting/extrapolation approach, the skin hardness was estimated to be 1.43 MPa, which is significantly lower than the hardness of stratum corneum (15.6 MPa) and slightly higher than the hardness of viable epidermis (1.30 MPa). This is attributed to the dominant effect of the significantly thicker and softer viable

epidermis and dermis than stratum corneum.

The lower reduced elastic modulus (1.91 MPa) and hardness (0.85 MPa) of dermis than those of stratum corneum by about three and one orders of magnitude, respectively, explains the sharp decrease of the mechanical properties of skin with increasing maximum contact depth (Figure 4.6). For small contact depths, the mechanical properties of skin are controlled by those of stratum corneum, whereas for relatively large contact depths, the mechanical behavior of skin is dominated by the viable epidermis and dermis properties. Thus, the loading response of skin due to shallow indentation is governed by the mechanical behavior of stratum corneum, while the unloading response of skin subjected to deep indentation is mostly influenced by the elastic behaviors of the viable epidermis and dermis.

A comparison of representative indentation load-displacement responses due to relatively shallow (Figure 4.8(a)) and deep (Figure 4.8(b)) indentation shows significant differences in both loading and unloading behavior. Shallow indentation produces a linear loading response (stratum corneum effect), while deep indentation yields a highly nonlinear loading response (viable epidermis/dermis effect). A linear loading response is not typical of contact deformation. This counterintuitive response can be explained by a simple bending plate model. Considering the significantly lower stiffness and strength of viable epidermis and dermis than those of stratum corneum, irreversible deformation in the viable epidermis and, possibly, dermis (depending on the maximum contact depth) below the rigid indenter yields a situation approximately analogous to that of a circumferentially clamped circular plate (stratum corneum) undergoing elastic bending due to a force applied to its center point. This problem yields a linear force-displacement response intrinsic of the elastic deformation of the stronger material (stratum corneum). Deep indentation induces irreversible deformation in both stratum corneum and viable epidermis/dermis, resulting in a nonlinear deformation response characteristic of an indented elastic-plastic layered medium consisting of a stiff and hard layer (stratum corneum) and a compliant and soft substrate (viable epidermis/dermis). This interpretation is supported by the linear and nonlinear unloading responses of the shallow and deep indentations and the significantly larger hysteresis area in the deep-indentation case.

Additional evidence of the indentation (contact) depth effect on the deformation behavior of skin was obtained from optical microscopy observations made after one hour from indentation. Shallow indentation caused only slight burnishing on the stratum corneum surface (Figure 4.9(a)), presumably because of local sliding against the indenter, indicating mainly elastic deformation in the bulk of stratum corneum. Alternatively, deep indentation induced gross plastic deformation, resulting in localized fracture of the stratum corneum after unloading (Figure 4.9(b)).

The presented results indicate that irreversible skin damage commences beyond a critical contact depth (on the order of the thickness of stratum corneum, i.e., ~10 μm) because of the inadequate support provided by the high compliance and weakness of viable epidermis/dermis. Because the rate of cell and tissue regeneration in injured viable

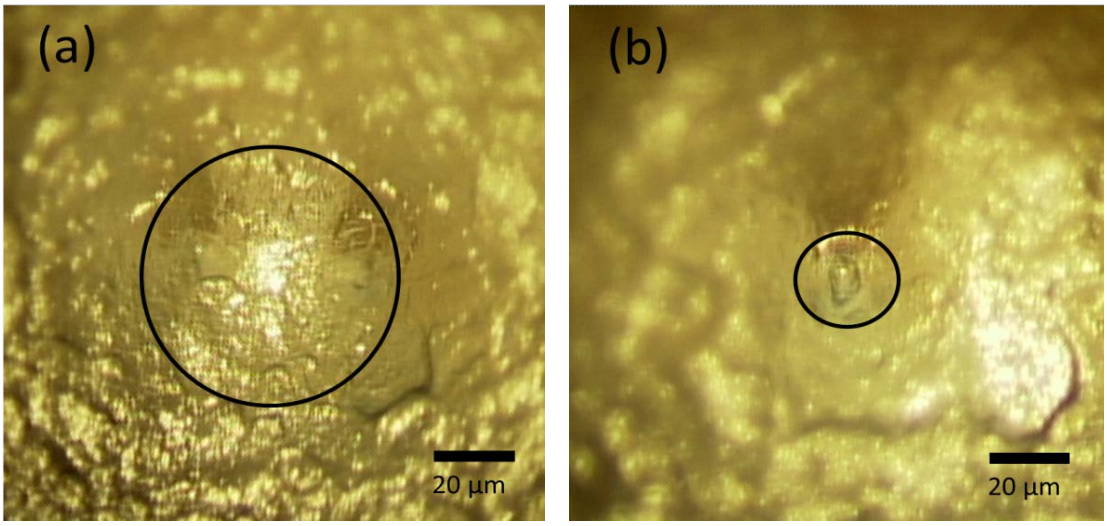

Figure 4.9 Optical microscope images of skin (American Yorkshire) obtained after 1 h from indentation with a conospherical diamond indenter of radius of curvature equal to 12.5 µm for a maximum displacement equal to (a) 60 and (b) 500 µm. (Indentation load-displacement responses corresponding to (a) and (b) are shown in Figures 4.8(a) and 4.8(b), respectively.).

epidermis is much faster than the replenishment rate of stratum corneum by the viable epidermis (Candi et al., 2005), understanding the role of the mechanical properties of individual layers on skin damage is of paramount importance to skin repair. The results presented in this chapter provide qualitative information for avoiding gross skin damage during minimally invasive procedures relying on the disruption of stratum corneum, such as transdermal drug delivery, local tissue and gene delivery, and blood or interstitial fluid sampling using microneedles.

Chapter 5. The Viscoelastic Behavior of the Skin

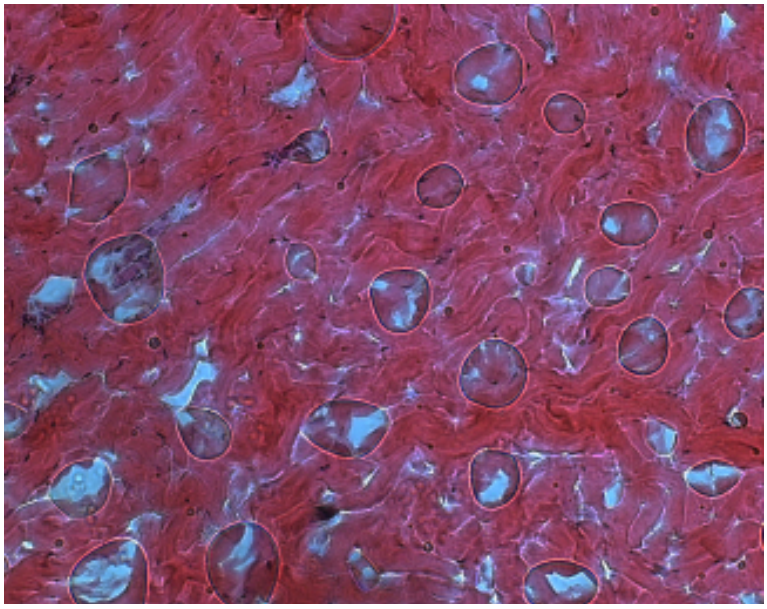

Chapter Opening Photo: Image of dermis layer (porcine skin specimen) was captured by an optical microscope at 40X magnification. Hematoxylin and eosin (H&E) staining was used for histology analysis. Ground substance of dermis layer is mainly responsible for the skin viscous behavior containing a high volume of moisture. Elastic and collagen fibrils from dermis layer are also responsible for skin elasticity and stiffness, respectively.

Mechanical testing was performed with microprobe-based instruments equipped with force transducers capable of applying normal loads in the range of 0.1–500 mN at loading/unloading rates of 5–20 μN/s. Light-load/low-depth indentation tests were performed with a surface force microscope (SFM) consisting of a capacitive force-displacement transducer (Triboscope, Hysitron, Minneapolis, MN) that replaces the original cantilever of an atomic force microscope (AFM, Nanoscope II, Digital

Instruments, Santa Barbara, CA), a detector assembly as the head, and the AFM scanner, and uses the software of a scanning tunneling microscope. The force transducer is a three-plate capacitor with the middle-plate supported by calibrated springs. The force exerted by the sample to a sharp tip attached to the center of the middle-plate of the force transducer is calculated from the capacitance change induced by the vertical displacement of the middle-plate. The projected contact area between the tip and the indented sample, referred to as the tip-shape function, is obtained as a polynomial function of indentation depth, using elastic modulus measurements obtained with a calibration material of known elastic modulus (e.g., quartz). All SFM tests were performed with a conospherical diamond tip of radius equal to 1 μm.

High-load/large-depth indentation tests were performed with a custom-made microprobe force apparatus (MFA, Bruker, Campbell, CA) equipped with a load sensor of 0.5 mN resolution and 4.9 N maximum load capacity and a capacitive displacement sensor of 0.1 μm depth resolution and >250 μm maximum indentation depth. An optical displacement sensor was used to measure the indentation depth in the micrometer-to-millimeter range. During MFA testing, the sample was kept under tension by a steel plate attached to the sample holder by four screws. Horizontal leveling of the sample was accomplished with a level bubble. Indentation testing was performed through a through-thickness hole of the steel plate, using a conospherical diamond-coated tip with a radius of curvature equal to 12.5 μm. The force and displacement sensors of the MFA were calibrated by applying known loads, using the correlation between the actuator movement and the output from the two depth sensors, respectively.

Because of the viscoelastic material behavior, trapezoidal load profiles were used in all the tests in order to avoid the so-called “nose” effect at the inception of unloading, an intrinsic phenomenon of viscoelastic materials, which prevents the calculation of the contact stiffness from the slope of the force response at the inception of unloading. Indentation load versus depth responses revealed a time-dependent deformation effect on the loading/unloading profile. While the specified trapezoidal load profile was observed for relatively shallow indentations (Figure 5.1(a)), the profile exhibited nonlinear loading and unloading paths in the case of relatively deep indentations (Figure 5.1(c)), revealing a time-dependent deformation that could not be quickly compensated by the load transducer. Thus, to maintain a constant loading/unloading rate, depth control was used during the loading and unloading phases of testing, while load control was used during the hold time in all the MFA experiments. However, load control was used in all the SFM tests.

To obtain insight into time-dependent deformation under constant load (creep tests) for different values of the hold time t_h, loading/unloading rate $\dot{L} = dL/dt$, and maximum indentation depth $h_{\max}$ (corresponding to the maximum load $L_{\max}$ applied during the hold time), a creep deformation parameter, hereafter referred to as creep strain, $\varepsilon_c = (h_f - h_i)/h_i$, where h_i and h_f are the initial and final indentation depths measured at the start and the end of a creep test, respectively, was used in the results presented next. Viscoelastic material constants and elastic contact stiffness of individual

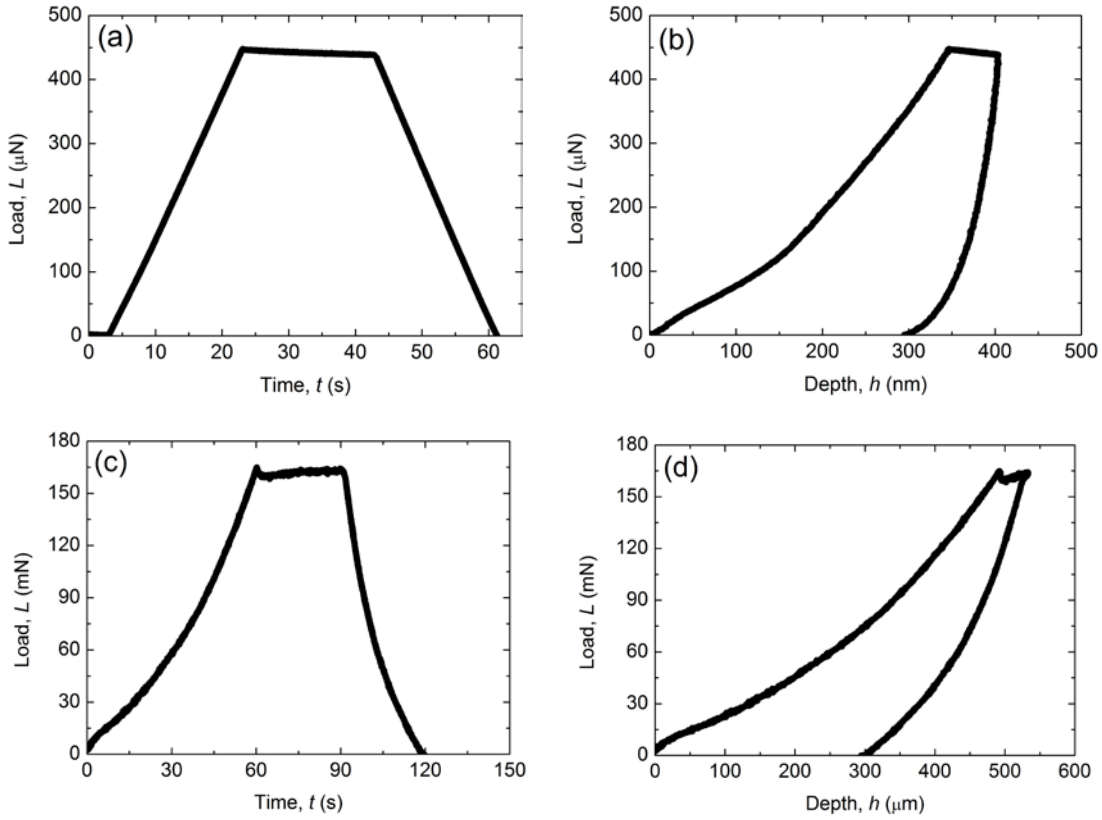

Figure 5.1 Indentation load L versus time t (left) and depth h (right) of porcine skin for $\dot{L}_l = \dot{L}_u =$ 22 μN/s and $L_{\max}$ equal to (a,b) 450 μN and (c,d) 150 mN. The nonlinear loading and unloading paths shown in (c) indicate a time-dependent deformation behavior, which cannot be compensated by the load transducer for the applied loading/unloading rate.

skin layers and whole skin were determined by curve fitting the ε_c data and the contact stiffness, $S = dL/dh$, measured at the inception of unloading, respectively. However, to accurately measure the elastic contact stiffness of viscoelastic materials, it is necessary to account for viscous effects on the unloading response. Thus, the elastic contact stiffness S^e was determined from the measured contact stiffness S at the onset of unloading using the relation (Tang and Ngan, 2003):

$$\frac{1}{S^e} = \frac{1}{S} - \frac{\dot{h}}{\dot{L}_u} \tag{5.1}$$

where $\dot{h}$ is the rate of depth change during the hold period (creep test) and $\dot{L}_u$ is the

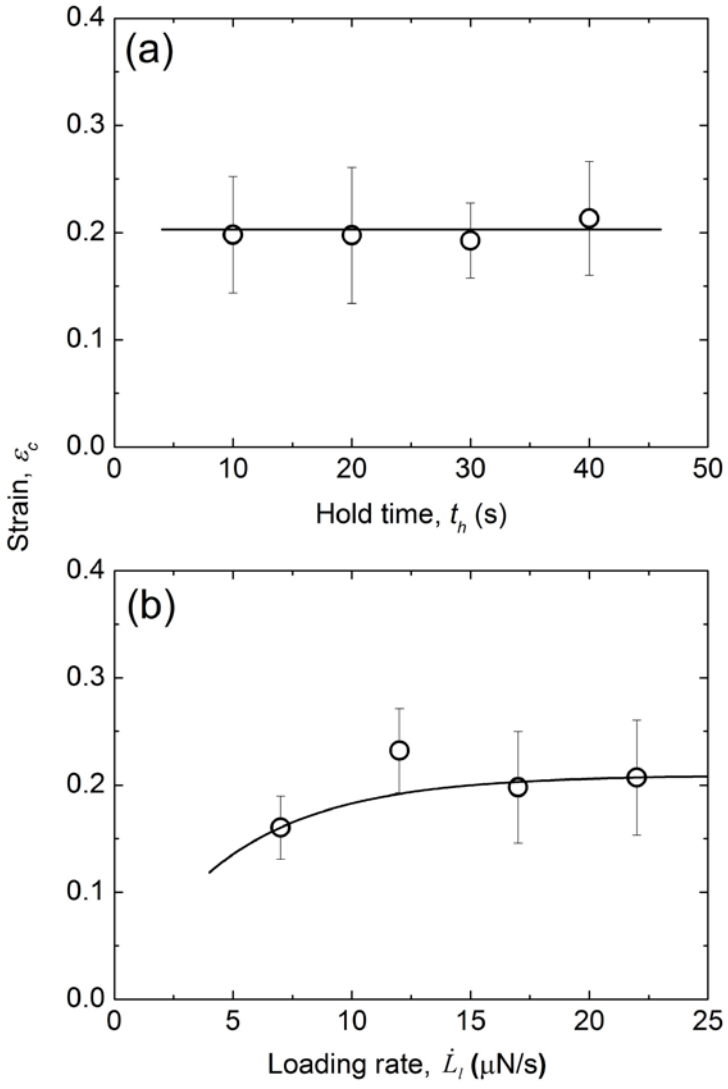

Figure 5.2 (a) Strain ε_c versus hold time t_h ($L_{\max}$ = 350 μN, $\dot{L}_l = \dot{L}_u$ = 17 μN/s) and (b) strain ε_c versus loading rate $\dot{L}_l$ ($L_{\max}$ = 350 μN, t_h = 20 s) for stratum corneum.

unloading rate at the inception of unloading. Equation (5.1) and the relation of the contact stiffness at the onset of unloading (Oliver and Pharr, 1992) have been previously used to extract the elastic modulus of indented viscoelastic materials, such as polymers (Zhou and Komvopoulos, 2006).

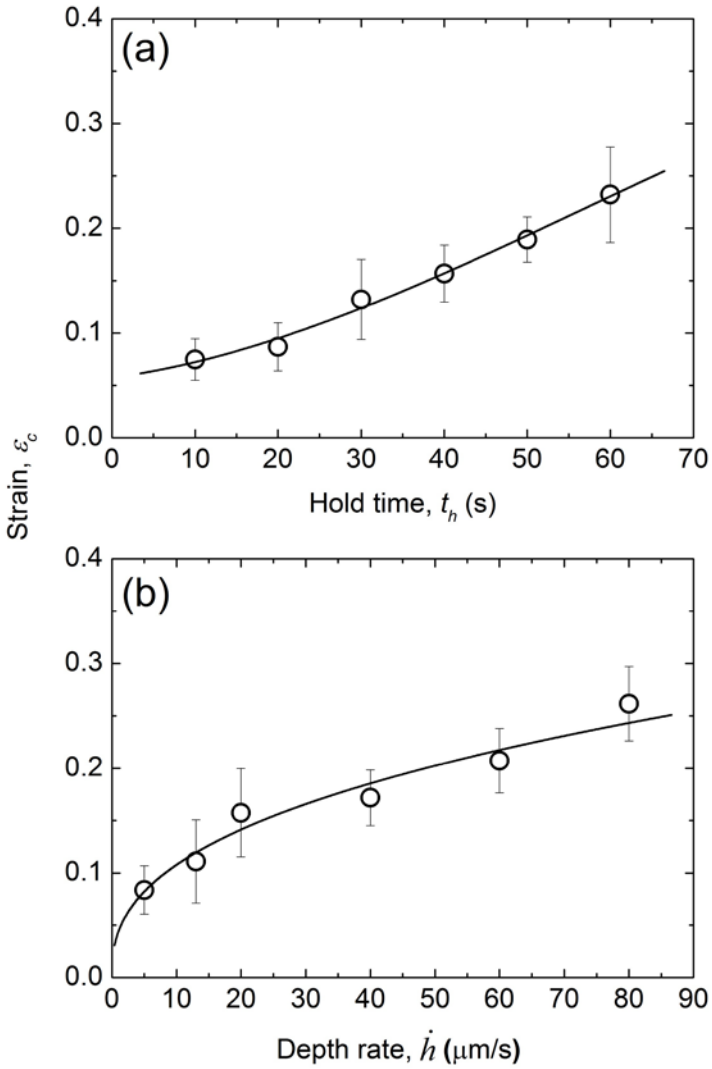

Figure 5.3 (a) Strain ε_c versus hold time t_h (h_0 = 400 μm, $\dot{h}$ =13 μm/s) and (b) strain ε_c versus depth rate $\dot{h}$ (h_0 = 400 μm, t_h = 30 s) for dermis.

5.1. Time-dependent deformation behavior

SFM tests with stratum corneum samples showed that ε_c is not a function t_h (Figure 5.2(a), k = 4, $n_j \approx$ 12 measurements/hold time, F = 0.237, p = 0.870), while initially tends to marginally increase with the loading rate $\dot{L}_l$ (Figure 5.2(b), k = 4, $n_j \approx$ 12, F = 2.735, p = 0.055). From the measured ε_c data, it may be inferred that stratum corneum

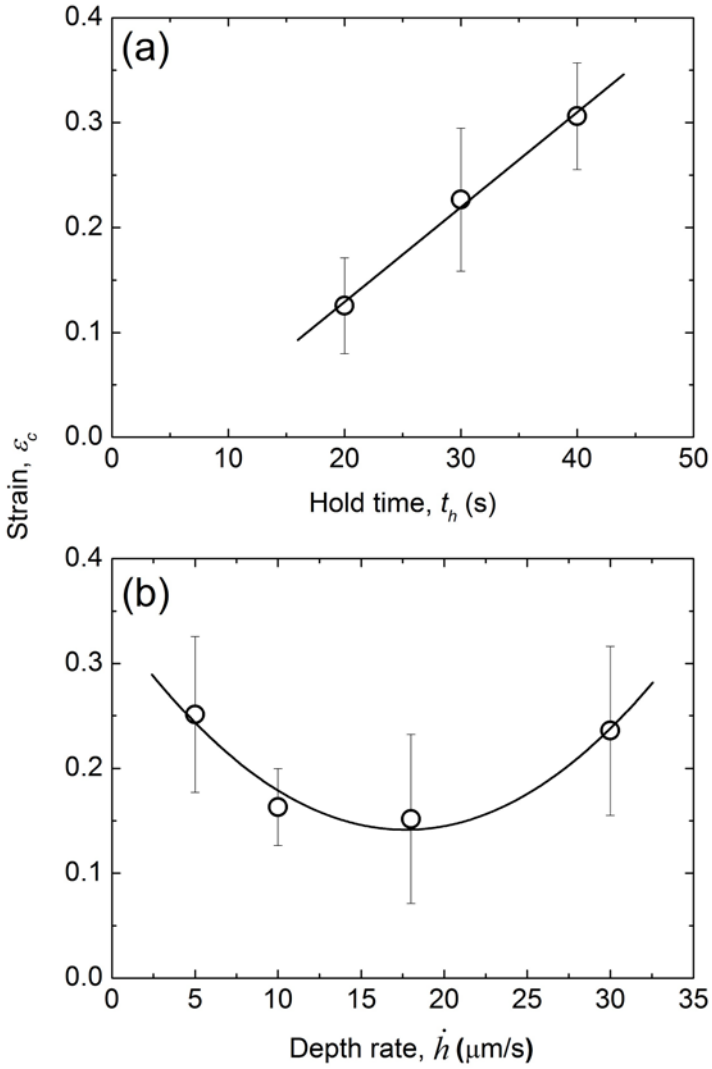

Figure 5.4 (a) Strain ε_c versus hold time t_h (h_0 = 150 μm, $\dot{h}$ =5 μm/s) and (b) strain ε_c versus depth rate $\dot{h}$ (h_0 = 150 μm, t_h = 30 s) for skin.

demonstrates essentially time-independent deformation. For $L_{\max}$ = 350 μN, ε_c in the stratum corneum is equal to ~0.20 ± 0.05.

MFA tests revealed a time-dependent deformation for dermis and skin. A monotonic increase of ε_c from ~0.08 to ~0.25 was found in the dermis samples with the increase of t_h in the range of 10–60 s (Figure 5.3(a), k = 6, $n_j \approx$ 11 measurements/hold time, F = 43.066, $p \approx 0$), $\bar{e}$ (average rms error) = 0.031) and $\dot{h}$ from 5 to 80 μm/s (Figure 5.3(b), k = 6, $n_j \approx$ 11 measurements/depth rate, F = 34.418, $p \approx 0$, $\bar{e}$ = 0.034). The

sensitivity of the dermis deformation to variations in hold time (Figure. 5.3(a)) and depth rate or indentation speed (Figure 5.3(b)) shows a strong time-dependent deformation behavior.

A similar variation of ε_c with t_h was observed with skin samples (Figure 5.4(a), k = 3, $n_j \approx$ 30 measurements/hold time, F = 47.783, $p \approx 0$), i.e., ε_c increased from ~0.12 to ~0.32 ($\bar{e}$ = 0.06) with the increase of t_h by twofold. However, the variation of ε_c with $\dot{h}$ significantly differed from that observed with stratum corneum and dermis, i.e., ε_c initially decreased from ~0.25 to ~0.15 and then increased to ~0.24 with the increase of $\dot{h}$ in the range of 5–30 μm/s (Figure 5.4(b), k = 4, $n_j \approx$ 25 measurements/depth rate, F = 13.237, $p \approx 0$). For the examined $\dot{h}$ range, the average ε_c in skin is ~0.216 ± 0.072, which is close to the strain in the stratum corneum (Figure 5.2). The initial decrease of ε_c with the increase of $\dot{h}$ is attributed to viscoelastic stretching of the skin to accommodate the accumulating deformation, while the increase of ε_c in the high range of $\dot{h}$ is associated with gross deformation in the stratum corneum and the upper region of the cellular epidermis, as shown by histology results (see section 5.3). Thus, for the ranges of indentation depth and depth rate investigated, skin deformation is controlled by the stratum corneum, whereas time-dependent deformation of skin is mainly due to the viscoelastic behavior of the cellular epidermis and the dermis.

5.2. Viscoelastic constants and elastic contact stiffness

A nonlinear variation of the maximum depth $h_{\max}$ with time t under constant $L_{\max}$ (hold period) was observed with stratum corneum (Figure 5.5(a)), dermis (Figure 5.5(b)), and skin (data are not shown as they were very similar to those of dermis). From a curve-fitting analysis, the function showing the best fit to the data ($R^2 \geq 0.99$ for all samples) was found to be in the form:

$$h_{\max} = h_0 + C_i t^{1/2} \tag{5.2}$$

where h_0 is the maximum depth at the start of the hold period (t = 0) and C_i ($i = sc$ (stratum corneum), de (dermis), sk (skin)) is a viscoelastic material constant determined by curve fitting.

Initial unloading shows a linear variation of load with time for stratum corneum (Figure 5.6(a), R^2 = 0.999) and a nonlinear load variation with time for dermis (Figure 5.6(b), R^2 = 0.999). Consequently, for stratum corneum, the initial unloading rate $\dot{L}_u$ can be obtained as

$$\dot{L}_u = \frac{L_{\max} - L}{t} \cong \frac{L_{\max}}{t_u} \tag{5.3}$$

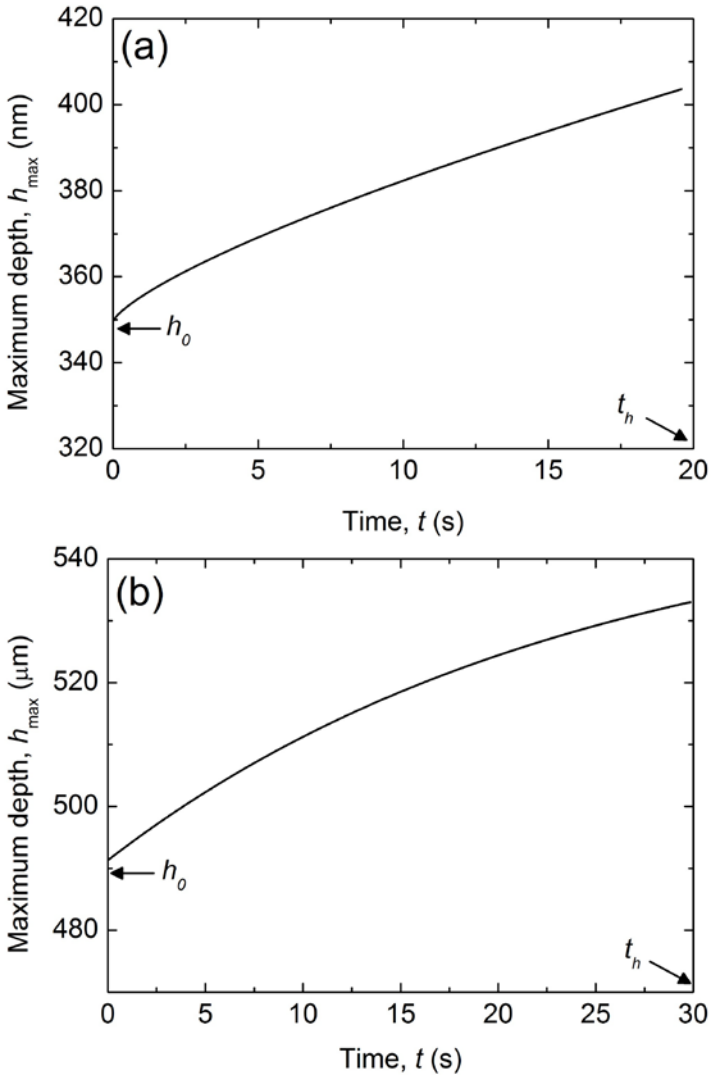

Figure 5.5 Variation of maximum depth $h_{\max}$ with time t under constant $L_{\max}$ (hold period) for (a) stratum corneum ($L_{\max}$ = 350 μN) and (b) dermis ($L_{\max}$ ≈ 150 mN).

where t_u is the time for full unloading. Thus, from Equations (5.1), (5.2), and (5.3), the elastic contact stiffness of stratum corneum S_{sc}^e can be expressed as

$$S_{sc}^e = \left[\frac{1}{S} + \frac{C_{sc} t_u}{2 t_h^{1/2} L_{\max}}\right]^{-1} \tag{5.4}$$

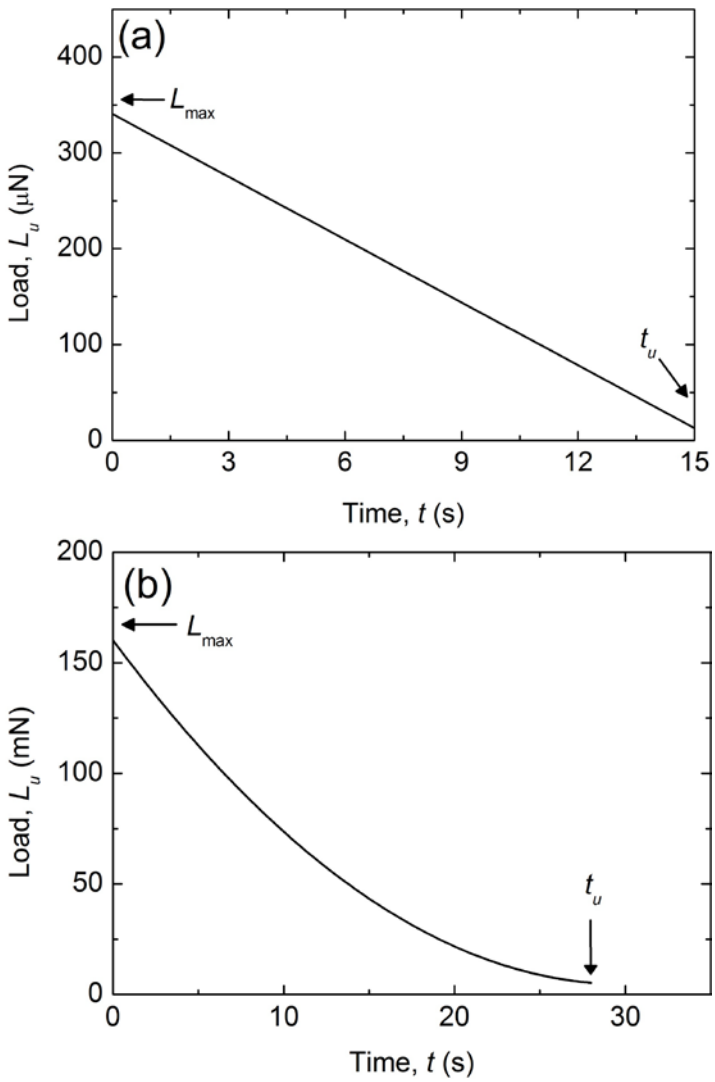

Figure 5.6 Variation of load L with time t during unloading for (a) stratum corneum and (b) dermis.

where C_{sc} is the viscoelastic constant of stratum corneum in Equation (5.2).

SFM measurements for loading/unloading and hold time fixed at 20 s did not show a dependence of C_{sc} on $L_{\max}$ applied during the hold period (Figure 5.7(a), k = 4, $n_j \approx 9$ measurements/maximum load, F = 0.888, p = 0.458). From the measured data, the mean value of C_{sc} is 20.8 ± 0.062 nm/s$^{1/2}$. These experiments also revealed a nonlinear decrease of S_{sc}^{e} (Equation (5.4)) with increasing $h_{\max}$ (or $L_{\max}$) (Figure 5.7(b), k = 5, $n_j \approx 7$ measurements/maximum depth, F = 4.0112, p = 0.01). This trend is attributed to the

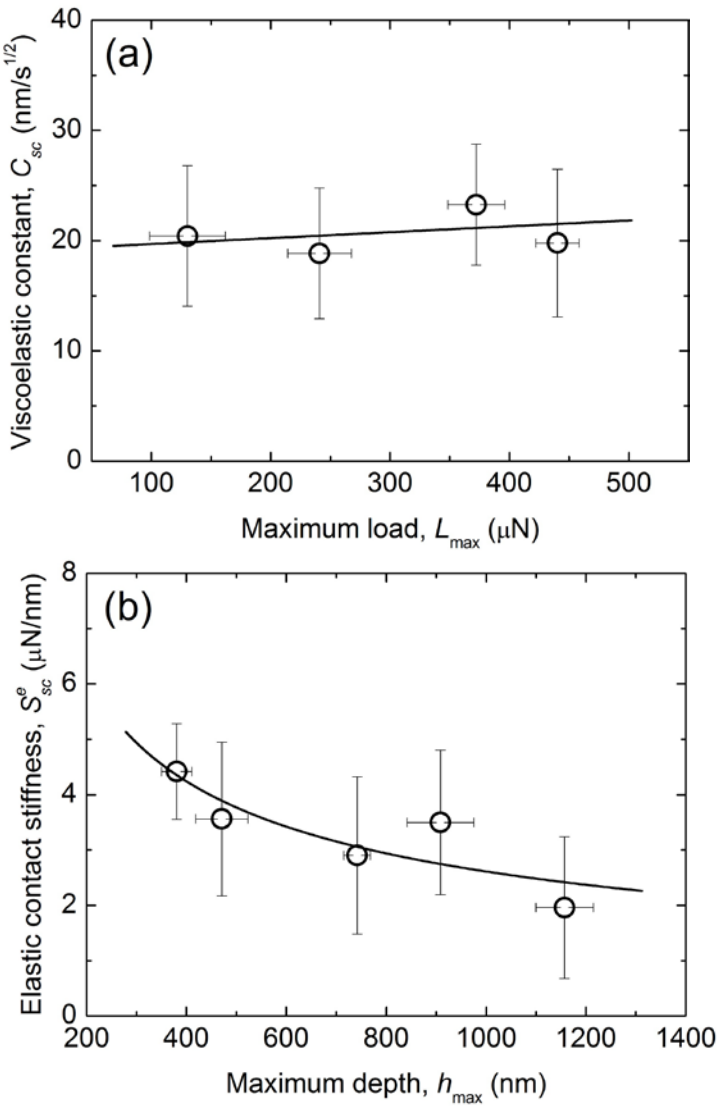

Figure 5.7 (a) Viscoelastic constant of stratum corneum C_{sc} versus maximum load $L_{\max}$ and (b) elastic contact stiffness of stratum corneum S^e_{sc} versus maximum depth $h_{\max}$ for $t_l = t_u = t_h = 20$ s.

intensifying effect of the soft cellular epidermis with increasing $h_{\max}$. From measurements obtained in the 400–1200 nm range of $h_{\max}$, the average S^e_{sc} is equal to ~3.47 ± 0.012 μN/nm.

Because of the nonlinear unloading response of dermis (Figure 5.6(b)), the initial unloading rate was obtained as the limit of a second-order polynomial function of time

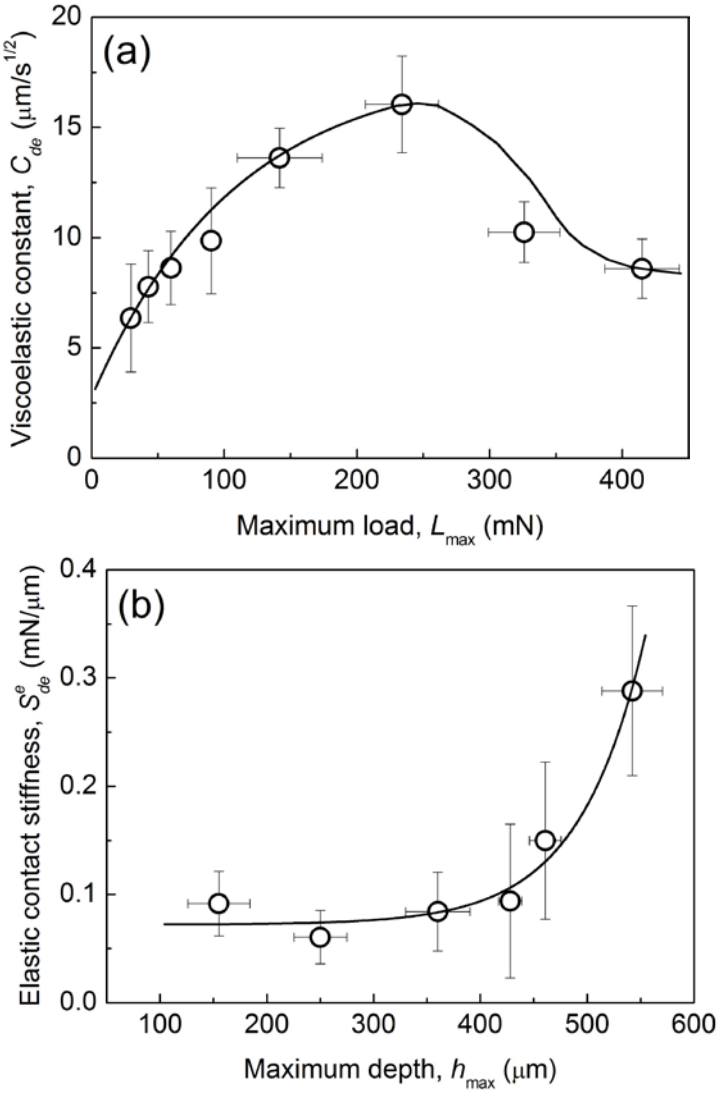

Figure 5.8 (a) Viscoelastic constant of dermis C_{de} versus maximum load $L_{\max}$ and (b) elastic contact stiffness of dermis S^e_{de} versus maximum depth $h_{\max}$ for t_h = 40 s and $\dot{h}$ =10 μm/s.

(R^2 = 0.997), i.e.,

$$\dot{L}_u = \lim_{t\to 0}\left\{\frac{d}{dt}(L_{\max} + D_1 t + D_2 t^2)\right\} \tag{5.5}$$

where constants D_1 and D_2 can be obtained by curve fitting. Combining Equations (5.1), (5.2), and (5.5), the elastic contact stiffness of dermis S^e_{de} is obtained as

$$S_{de}^{e} = \left[\frac{1}{S} + \frac{C_{de}}{2D_{de}t_h^{1/2}}\right]^{-1} \tag{5.6}$$

where C_{de} and D_{de} are the dermis viscoelastic constants in Equations (5.2) and (5.5), respectively.

MFA tests performed with dermis samples for $\dot{h}$ = 10 μm/s and t_h = 40 s showed a strong dependence of the dermis viscoelastic behavior and elastic contact stiffness on $L_{\max}$ and $h_{\max}$, respectively. In particular, C_{de} initially increased from 6 to 16 μm/s$^{1/2}$ in the range of ~25 ≤ $L_{\max}$ ≤ 230 mN and then decreased to a plateau of ~9 μm/s$^{1/2}$ in the range of $L_{\max}$ ≥ 400 mN (Figure 5.8(a), k = 8, n_j ≈ 9 measurements/maximum depth, F = 25.213, p ≈ 0), while S_{de}^{e} increased monotonically in the range of 150 ≤ $h_{\max}$ ≤ 550 μm (Figure 5.8(b), k = 6, n_j ≈ 12 measurements/maximum depth, F = 27.79, p ≈ 0). It is noted that the critical depth ($h_{\max}$= 400 μm) beyond which S_{de}^{e} sharply increases correlates to $L_{\max}$ = 230 mN, which corresponds to the peak value of C_{de}. The increase of C_{de} in the range 0 ≤ $L_{\max}$ ≤ 230 mN is attributed to the intensifying viscoelastic behavior of dermis with increasing load, while the gradual decrease of C_{de} in the range $L_{\max}$ ≥ 230 mN is due to fluid being squeezed out of the compressed dermis, which becomes significant above a critical load (pressure). This explanation is in agreement with the trend of S_{de}^{e} to sharply increase in the maximum depth range $h_{\max}$ ≳ 400 μm, which corresponds to the load range $L_{\max}$ ≥ 230 mN, due to the significant loss of fluid from the dermis. The fact that C_{de} (Figure 5.8(a)) is about three orders of magnitude higher than C_{sc} (Figure 5.7(a)) implies a dominant dermis effect on skin viscoelasticity, whereas the asymptotic increase of S_{de}^{e} (Figure 5.8(b)) toward values approaching those of S_{sc}^{e} (Figure 5.7(b)) indicates a dominant effect of stratum corneum on the elastic contact stiffness of skin. Thus, time-dependent deformation is mostly due to the dermis, while elastic contact stiffness is mainly provided by the stratum corneum.

Considering the similar elastic contact behavior of the dermis and the skin, the elastic contact stiffness of skin S_{sk}^{e} can be expressed by a relation similar to that given by Equation (5.6), i.e.,

$$S_{sk}^{e} = \left[\frac{1}{S} + \frac{C_{sk}}{2D_{sk}t_h^{1/2}}\right]^{-1} \tag{5.7}$$

where C_{sk} and D_{sk} are skin viscoelastic constants in Equations (5.2) and (5.5), respectively. C_{sk} shows an increasing trend similar to that of dermis up to $L_{\max}$ ≈ 130 mN, a plateau of ~11.5 μm/s$^{1/2}$ in the intermediate range 130 ≤ $L_{\max}$ ≤ 350 mN, and a tendency to increase in the range $L_{\max}$ > 350 mN (Figure 5.9(a), k = 8, n_j ≈ 13 measurements/maximum load, F = 65.885, p ≈ 0).

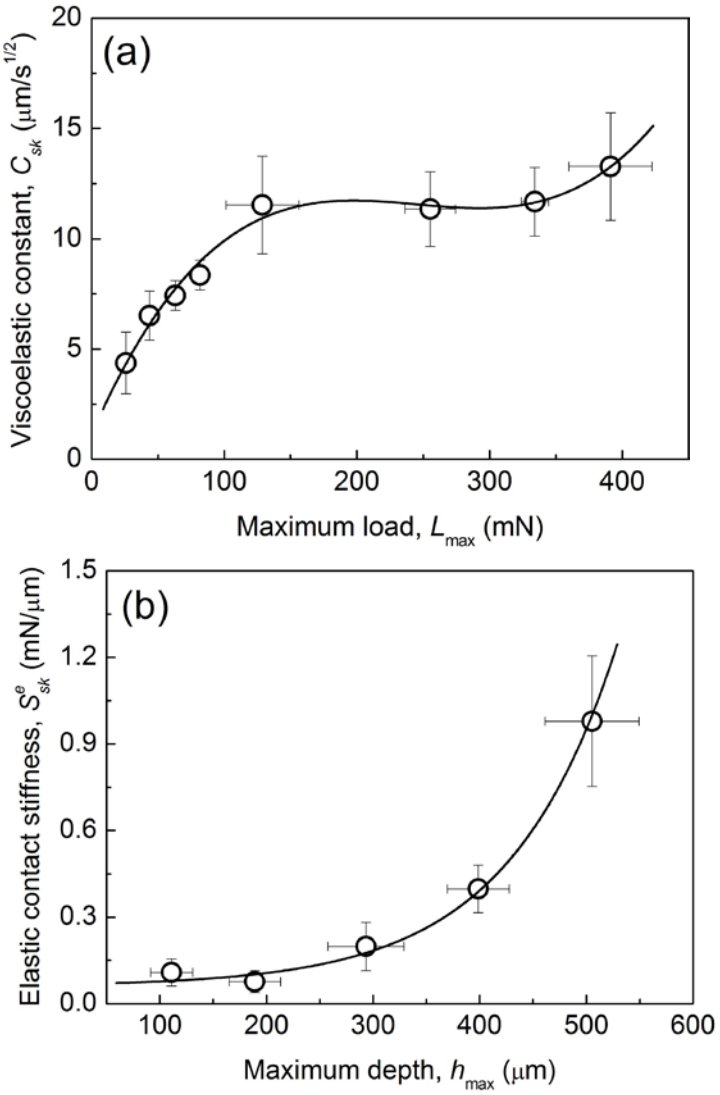

Figure 5.9 (a) Viscoelastic constant of skin C_{sk} versus maximum load $L_{\max}$ and (b) elastic contact stiffness of skin S^e_{sk} versus maximum depth $h_{\max}$ for t_h = 40 s and $\dot{h}$ =10 μm/s.

S^e_{sk} demonstrates a trend very similar to that of dermis, assuming values between those of the dermis and stratum corneum (Figure 5.9(b), k = 5, n_j ≈ 13 measurements/maximum depth, F = 247.436, p ≈ 0). In the range $h_{\max} \leq$ 190 μm, S^e_{sk} ≈ 0.09 mN/μm, which is close to S^e_{de} for the same range (Figure 5.8(b)), while in the range $h_{\max} >$ 190 μm, S^e_{sk} assumes much higher values, which are close to those asymptotically approached by S^e_{sc} in the same range (i.e., on the order of ~1 mN/μm or ~1 μN/nm).

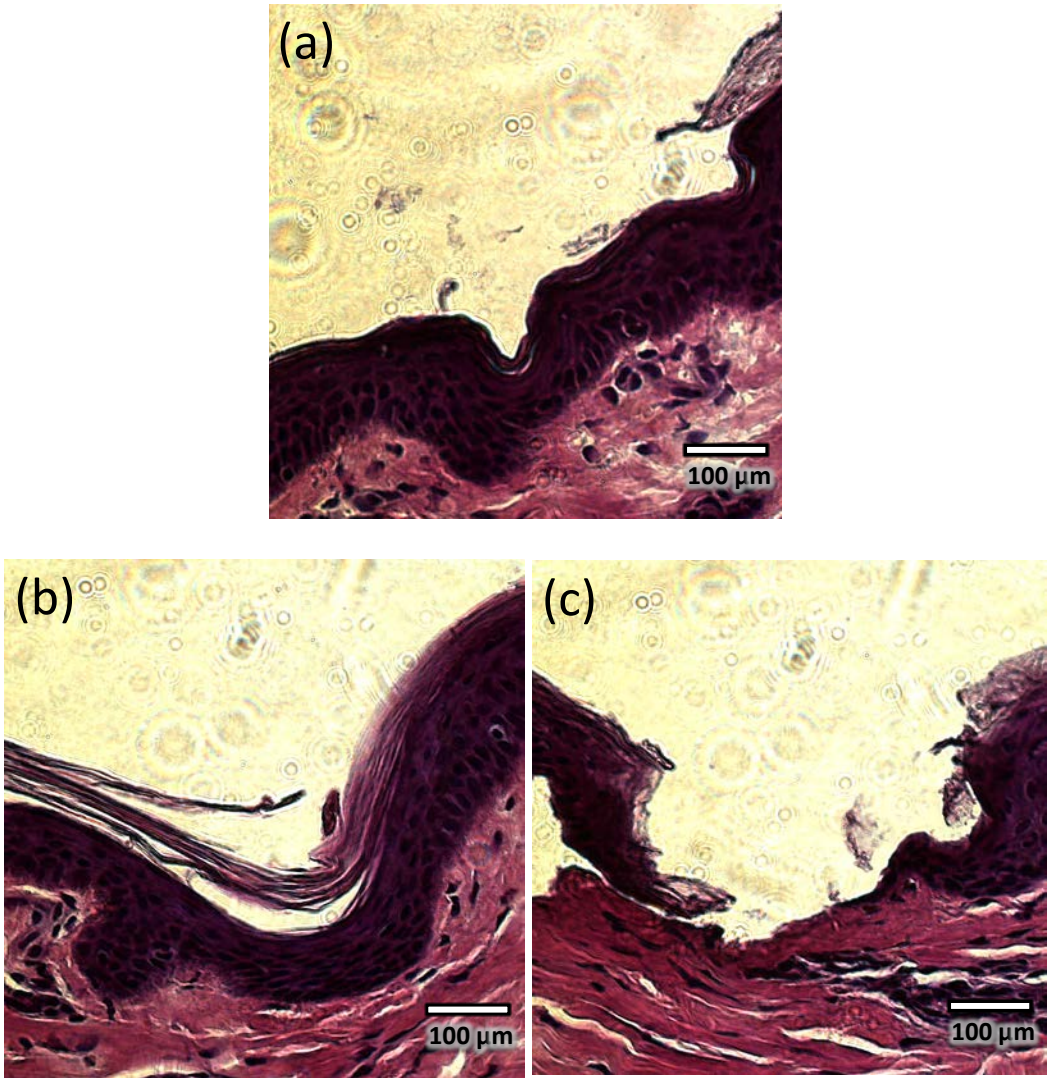

Figure 5.10 Cross-sectional optical microscope images of skin scratched under a load of (a) 50, (b) 200, and (c) 400 mN (scratch length = 1 mm, scratch time = 200 s).

Thus, S_{sk}^{e} demonstrates a dramatic increase with $h_{\max}$ (by about an order of magnitude) with S_{de}^{e} and S_{sc}^{e} representing lower and upper bounds.

5.3. Cross-sectional histology

Cross-sectional histology provided additional insight into the deformation behavior of

different skin layers. Because obtaining cross-sectional samples from indented skin specimens *in situ* is extremely cumbersome, slow speed (5 μm/s) scratch tests were performed with the MFA in the 50–400 mN load range, and cross-sectional samples were obtained perpendicular to the residual scratch produced on the scratched skin samples. Although the loads applied in the scratch tests do not exactly match the $L_{\max}$ applied during the hold period, the histology results provide a useful qualitative means of evaluating the role of stratum corneum, cellular epidermis, and dermis in skin deformation and shear-induced damage. For relatively light loads (i.e., 50 mN), deformation leads to shallow sinking of the skin tissue without excessive damage in the epidermis and/or delamination at the stratum corneum/cellular epidermis interface (Figure 5.10(a)). Dark-red spots in the dermis represent hard fibrils and nuclei. The absence of notable changes in the epidermis suggests that under light-load scratching conditions, skin deformation is mainly controlled by the dermis.

Significant skin damage can be observed for intermediate loads (e.g., 200 mN). In addition to more pronounced irreversible sinking of the skin, there is excessive cohesive failure and delamination of the hard stratum corneum from the soft cellular epidermis, apparently due to the development of high tensile stresses in the downward bended stratum corneum and significant viscoelastic-plastic property mismatch of stratum corneum and cellular epidermis (Figure 5.10(b)). Skin scratching under high loads (e.g., 400 mN) leads to severe scaring of the skin, characterized by the complete removal of the stratum corneum and cellular epidermis (Figure 5.10(c)).

The deformation behavior revealed by the histology results provides explanation for the viscoelastic response and elastic contact stiffness of skin (Figure 5.9). Because light-load skin deformation is mainly controlled by dermis deformation (Figure 5.10(a)), in the low range of $L_{\max}$ and $h_{\max}$, C_{sk} and S_{sk}^{e} are mainly affected by C_{de} and S_{de}^{e} (Figure 5.8), respectively. In the intermediate range of $L_{\max}$, C_{sk} remains almost constant because skin deformation is controlled by the deformation in stratum corneum, which does not exhibit a viscoelastic behavior (Figure 5.2(a)). Both C_{sk} and S_{sk}^{e} increase in the high range of $L_{\max}$ and $h_{\max}$, respectively, due to the enhanced viscous behavior of dermis at high contact pressures. Loss of fluid from the heavily compressed tissue is restricted by the rigid tip, which acts as a seal for the severely damaged skin, and the practically impermeable stratum corneum at the skin surface outside the tip/sample contact region.

5.4. Creep and stress relaxation

Long-term creep and stress-relaxation experiments yielded additional insight into the deformation behavior of dermis. Creep tests (5 samples, L = 90 mN) revealed a viscoelastic-plastic response, characteristic of a rheological model including elastic, steady-state creep, and transient creep elements (Figure 5.11(a)). The sharp depth decrease upon full unloading (t = 300 s) is mostly attributed to stratum corneum, whereas

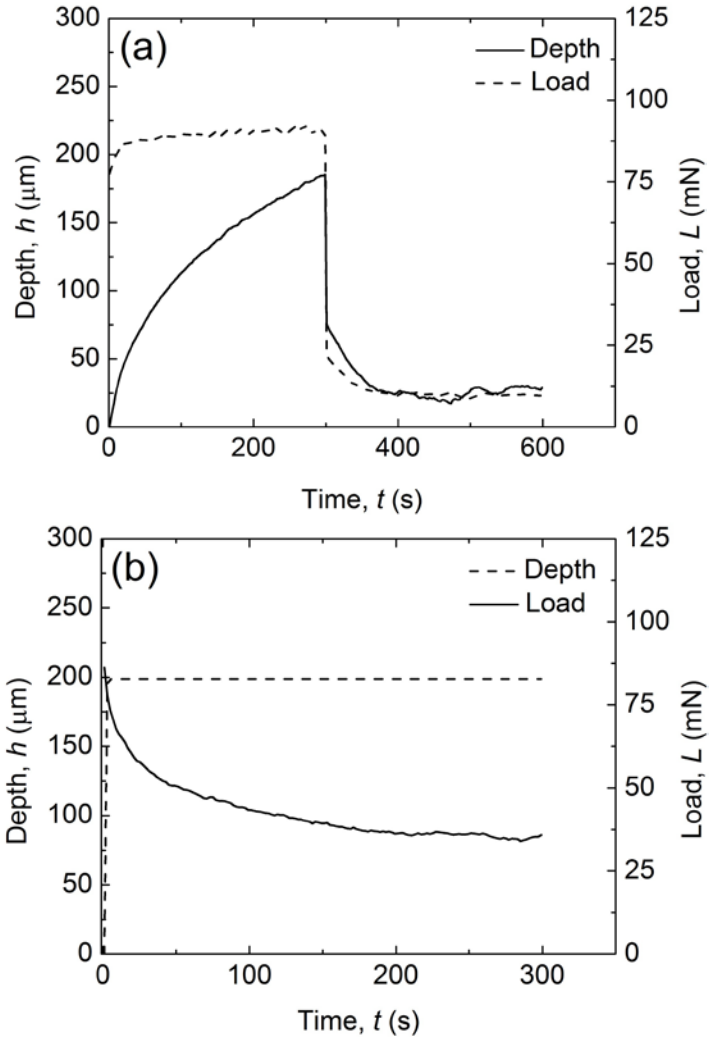

Figure 5.11 Depth h and load L versus time t response of dermis due to (a) creep and (b) stress relaxation.

subsequent transient creep (recovery) is attributed to the viscoelastic behaviors of the cellular epidermis and dermis. From 25 creep tests, it was found that C_{de} = 10.42 ± 0.844 μm/s$^{1/2}$, which is in good agreement with the value determined from short-term tests under a 90 mN load (Figure 5.8(a)).

Long-term stress relaxation experiments (Figure 5.11(b)), i.e., fixed indentation depth, showed a response characterized by steady-state creep and elastic behavior, which follows the relation

$$L = L_0\left(1 - \frac{1}{\lambda}\ln t\right) \tag{5.8}$$

where L_0 is the load measured at t = 0 and λ is a time relaxation constant expressed in units of ln(time). From 20 stress-relaxation tests, it was found that λ = 11.84 ± 0.934 ln(s).

5.5 Summary

Time-dependent deformation of skin was examined by SFA and MFA methods. The evolution of deformation in the stratum corneum, dermis, and skin was tracked in terms of the creep strain measured under constant maximum load (hold period) and varying loading rate (or depth rate). Stratum corneum demonstrated practically time independent deformation and a gradual decrease in elastic contact stiffness with increasing depth distance. Dermis showed strong viscoelastic deformation, which strongly affected the time-dependent deformation of skin. Dermis viscoelasticity and elastic contact stiffness showed a nonlinear dependence on the maximum load applied during the hold period and depth rate (indentation speed), respectively. Skin stiffness increased with load (penetration depth), showing a transition from a low stiffness typical of the dermis to a high stiffness approaching that of stratum corneum.

Histology and experimental measurements led to the development of a conceptual deformation in the stratum corneum (intermediate loads), and removal (cohesive and interfacial failure) of the stratum corneum and cellular epidermis in conjunction with significant fluid loss from the dermis (high loads).

Chapter 6. The Tribological Properties of Skin

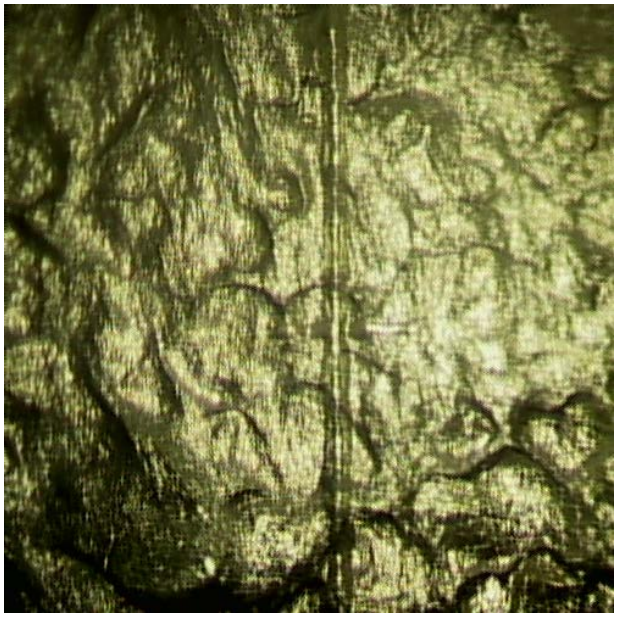

Chapter Opening Photo: Image of a scratched porcine skin surface captured by an optical microscope at 11X magnification. Microscratching is a method for studying the frictional and tribological behavior of materials. The present scratch was produced by scratching under a 5 g normal load using a 12.5-μm-radius conospherical diamond coated tip. A deformed profile obtained after 2 h from testing confirmed that the existence of permanent deformation on the skin surface.

The effect of normal load, scratch time (speed), and scratch cycles on the tribological (friction and wear) properties of porcine skin is examined in this chapter. Representative results from unidirectional and cyclic scratch experiments are contrasted to reveal the role of individual layer properties on the overall skin friction and wear properties.

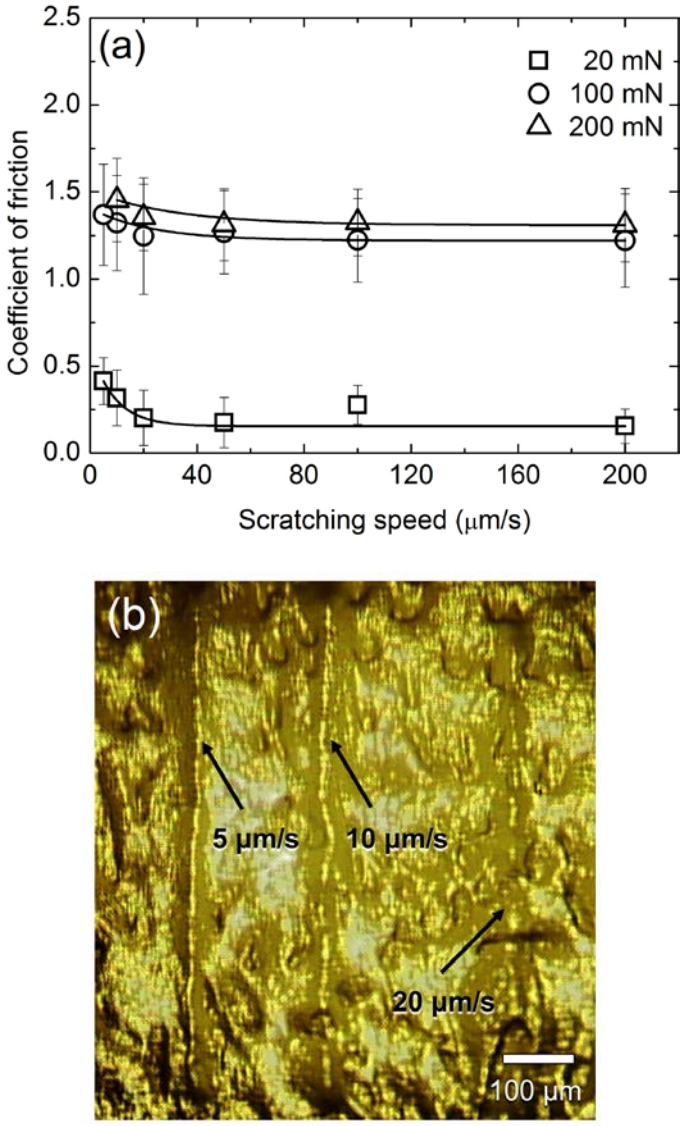

Figure 6.1 (a) Coefficient of friction of skin versus scratch speed (normal load = 20, 100, and 200 mN) and (b) optical microscope image of a scratched skin surface (normal load = 20 mN; scratch speed = 5, 10, and 20 μm/s).

6.1 Coefficient of friction versus scratching speed

Figure 6.1(a) shows the coefficient of friction as a function of scratch time and normal

load (n = 5). The results show a dependence of skin friction on scratch speed and normal load in the low ranges of speed (<40 μm/s) and normal load (20–100 mN). The decrease of friction with the increase of the scratch speed is attributed to the decreasing intimacy of the microprobe tip with the skin surface, which is particularly pronounced at light loads, whereas the increase of friction with the normal load is a consequence of the enhancement of the adhesion and plowing friction mechanisms with the increase of the penetration depth (Komvopoulos, 1986).

Figure 6.1(b) shows an optical microscope image of wear marks produced from scratching at different speeds under a normal load of 20 mN. The formation of a continuous wear track only in the case of the lowest scratch speed (5 μm/s) indicates a decrease in the tip/skin contact intimacy with the increase of the relative sliding speed, in agreement with the decreasing trend of the coefficient of friction observed in the low speed range of Figure 6.1(a). Since the 5 μm/s speed resulted in continuous tip/skin interaction during scratching under a relatively light load (20 mN), in all of the results presented next the scratch speed was fixed at 5 μm/s, to ensure full contact between the tip and the skin surface.

6.2 Microscratching under constant normal load

To obtain further insight into skin friction, the friction characteristics of the epidermis and dermis were studied by applying a moderate normal load of 100 mN. In the case of the epidermis, the penetration depth initially increased, stabilizing after about 50 s at ~100 μm (Figure 6.2(a)), whereas in the case of the dermis, it showed a continuous increasing trend (Figure 6.2(b)). The time-independent deformation of epidermis at steady-state scratching (>50 s) is attributed to the hard stratum corneum and the time-dependent deformation of dermis to its highly viscous character which is largely due to the high water content. These different deformation behaviors of the epidermis and dermis affect their friction characteristics in different ways.

While the coefficient of friction of epidermis increased to an average steady state of ~1.0 (Figure 6.2(c)), that of dermis increased to a peak value of ~4.5 and then gradually decreased to a steady state of ~0.6 (Figure 6.2(d)). The initial increase of the coefficient of friction of epidermis and dermis is due to the increase of the penetration depth, which resulted in the enhancement of the adhesion and plowing friction mechanisms. Fluctuations in the steady-state friction behavior of epidermis are indicative of wear debris formation (mostly from the stratum corneum, as shown by cross-sectional histology), resulting in continuous changes in the real area of contact. The decrease of the coefficient of friction of dermis after the initial rise is most likely due to a squeeze lubrication mechanism, similar to that encountered with pressurized articular cartilage, leading to the entrapment of fluid between the tip and the dermis surface, causing a transition from boundary lubrication to mixed lubrication scratching conditions.

Epidermis and dermis also exhibited significantly different friction variations with

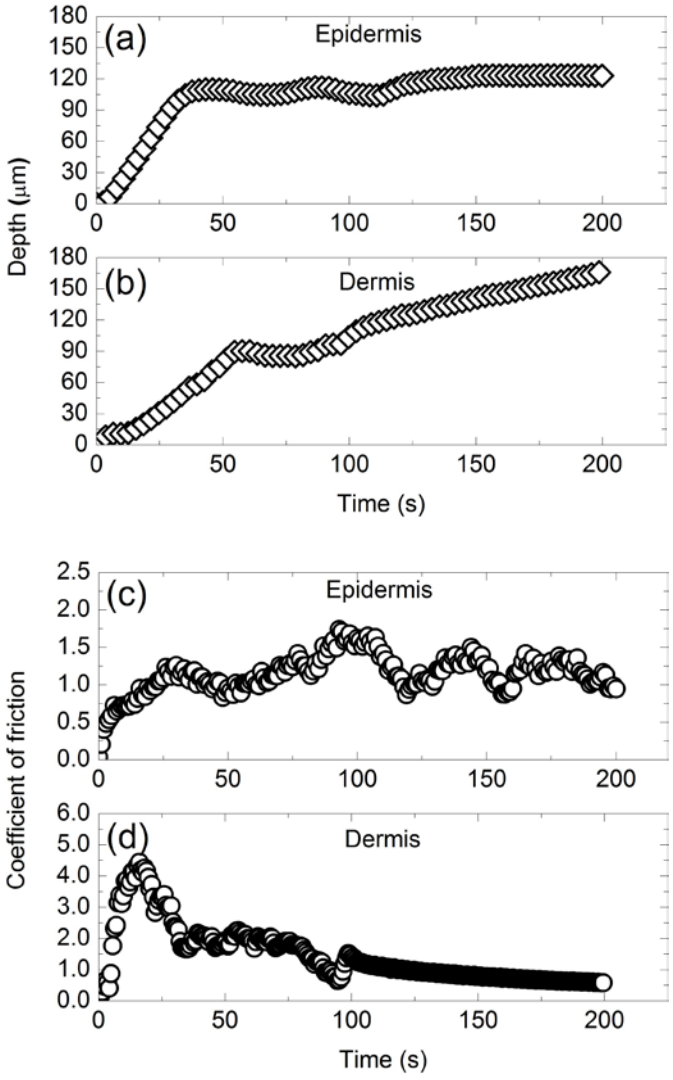

Figure 6.2 (a) Depth versus scratch time for (a) epidermis and (b) dermis and coefficient of friction versus scratch time for (c) epidermis and (d) dermis (normal load = 100 mN, scratch speed = 5 μm/s).

normal load. The effect of normal load on the coefficient of friction of epidermis and dermis is shown in Figure 6.3(a) ($n = 5, p \approx 0$) and Figure 6.3(b) ($n = 5, p = 0.00086$), respectively. Epidermis friction increased with normal load because the resulting larger penetration depths intensified the adhesion and plowing friction mechanisms, while dermis friction demonstrated a decreasing trend, attributed to the effect of squeeze film lubrication. The profoundly higher coefficient of friction of epidermis than that of dermis

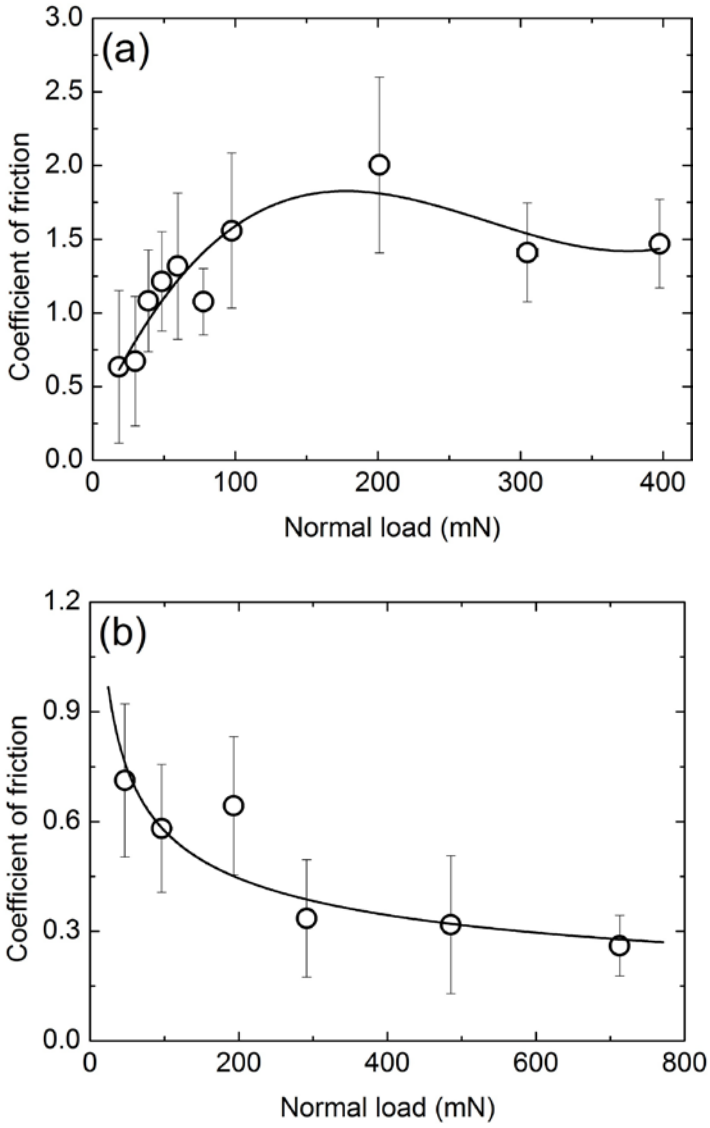

Figure 6.3 (a) Coefficient of friction of (a) epidermis and (b) dermis versus normal load (scratch speed = 5 μm/s).

is illustrative of the high shear resistance of the skin surface, which is largely due to the strength of the hard stratum corneum.

Microscopy observations yielded insight into the effect of normal load on shear-induced skin damage. Figure 6.4 shows images of worn skin samples for different normal loads. Light-load damage is characterized by plastic flow (plowing) of the skin surface (Figure 6.4(a)), revealing mostly irreversible deformation with minimal tissue removal.

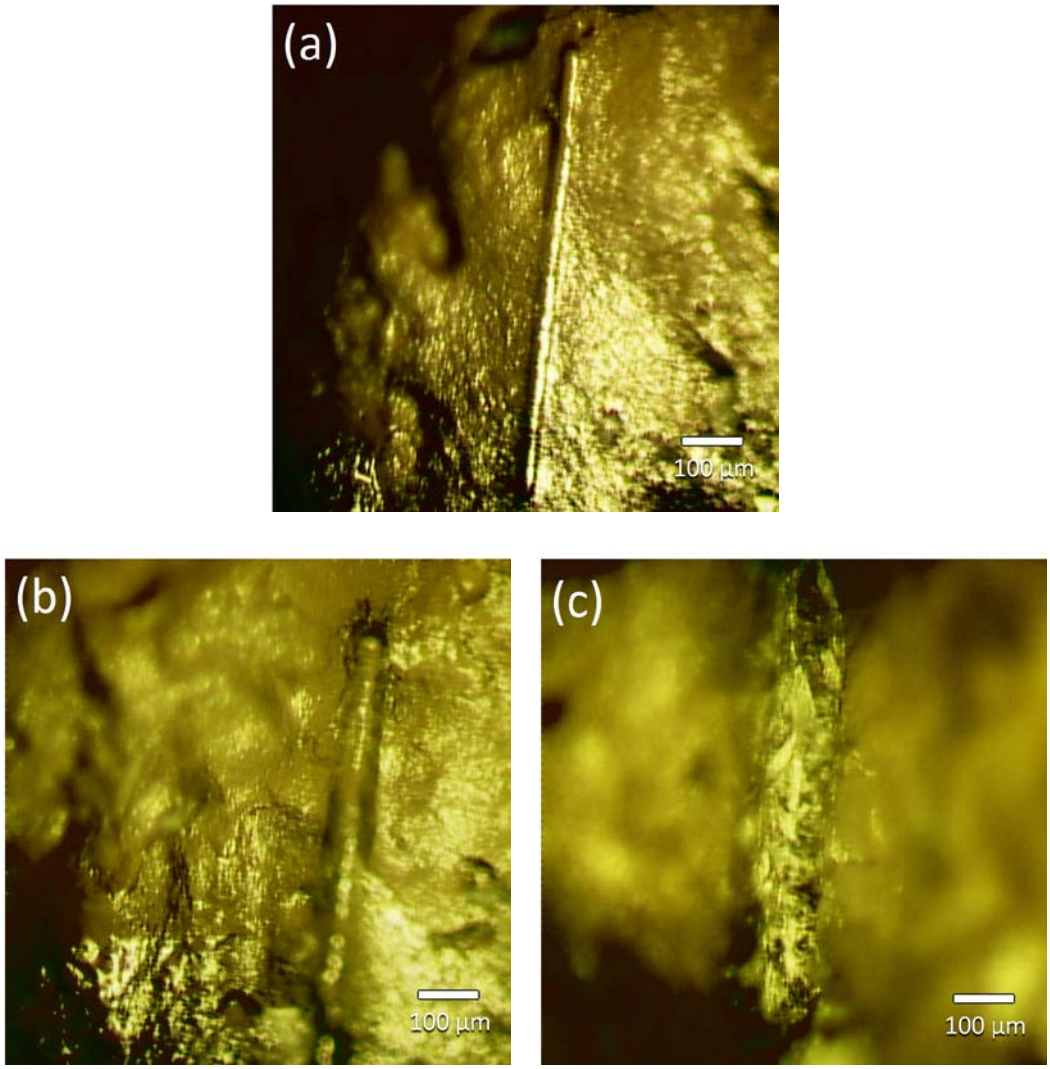

Figure 6.4 (a) Optical microscope images of scratched skin surfaces for normal load equal to (a) 20, (b) 50, and (c) 400 mN (scratch speed = 5 µm/s).

Moderate loads produced wider and less uniform wear marks and revealed the onset of tissue tearing (Figure 6.4(b)). Heavy-load scratching resulted in extensive skin damage and material removal mainly by the tearing wear mode (Figure 6.4(c)).

More detailed information about the effect of normal load on the prevailing skin damage (wear) mechanism in unidirectional scratching can be derived from the cross-sectional histology images shown in Figure 6.5. A transition from a plowing process comprising plastic sinking of the skin surface (Figure 6.5(a)) to interfacial delamination (Figure 6.5(b)) and cohesive failure (Figure 6.5(c)) of the stratum corneum, followed by

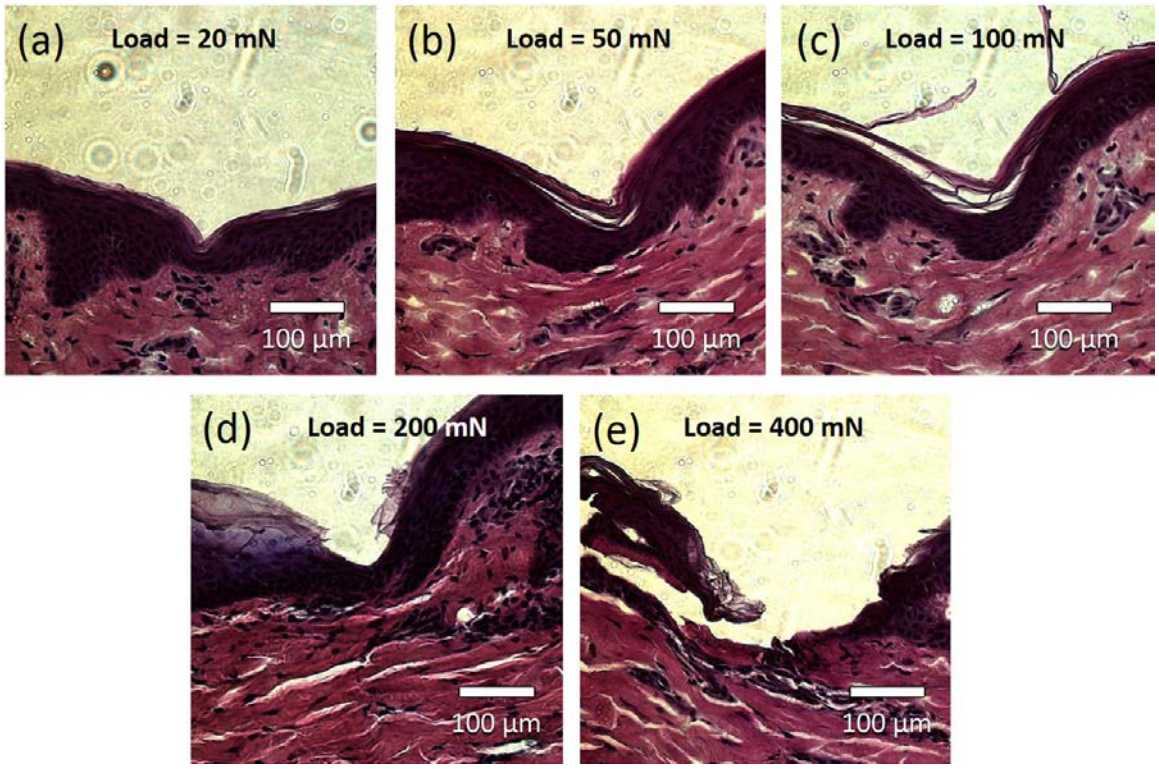

Figure 6.5 (a) Cross-sectional histology images of scratched skin for normal load equal to (a) 20, (b) 50, (c) 100, (d) 200, and (e) 400 mN (scratch speed = 5 µm/s).

the complete removal of stratum corneum (Figure 6.5(d)) and tearing of the cellular epidermis (Figure 6.5(e)) were observed with the increase of the normal load in the range 20–400 mN. These results suggest that low-load skin damage is mainly due to irreversible deformation accumulating in the dermis, while high-load skin damage is a manifestation of several wear processes, including delamination and cohesive failure in the stratum corneum and tearing in the cellular epidermis. The transition from mild to severe skin damage with the load increase, characterized by a change from surface plasticity (sinking) to subsurface cohesive failure, delamination, and rupture, provides explanation for the increasing and decreasing friction trends observed in Figure 6.3(a) and 6.3(b), respectively. In particular, the sharp rise of skin friction in the 25–100 mN load range is due to the enhancement of shear-induced damage, leading to the separation of stratum corneum from the cellular epidermis, whereas the decreasing friction trend for loads higher than 200 mN is attributed to the exposure of the soft dermis and the effect of squeeze film lubrication.

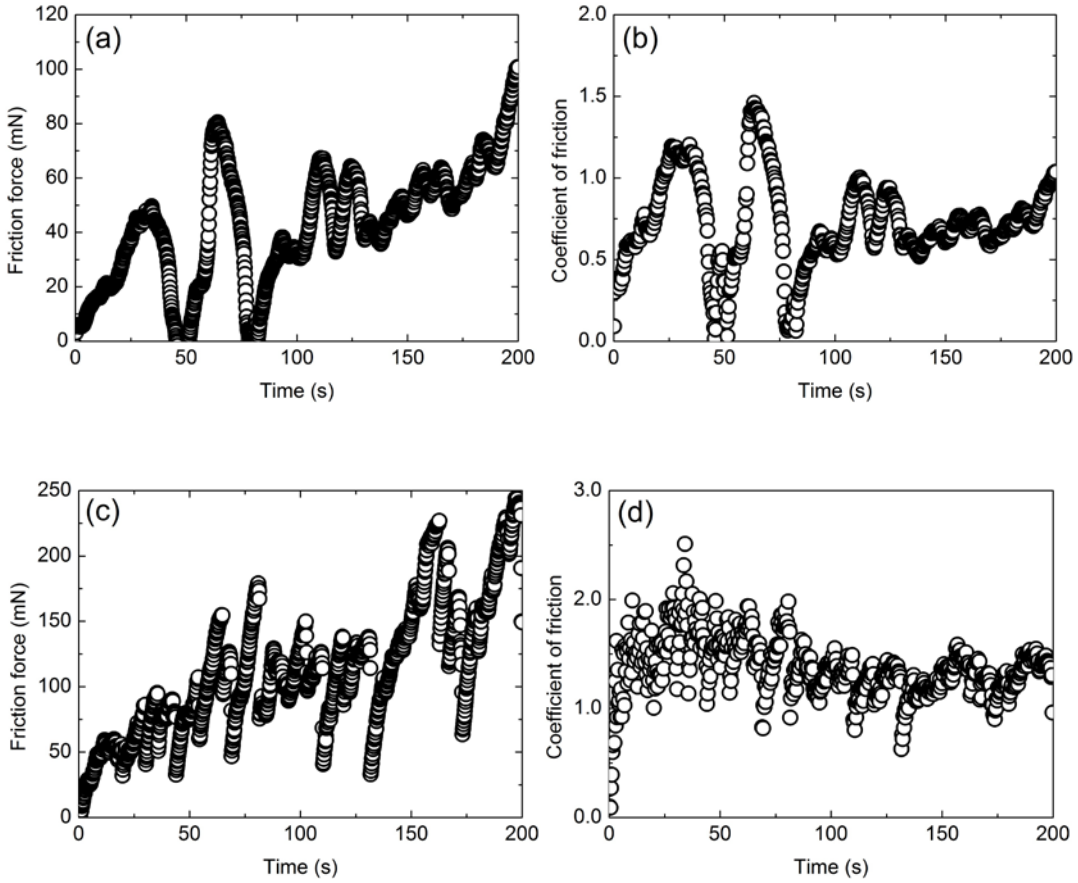

Figure 6.6 (a) Friction force and (b) coefficient of friction of skin versus scratch time for normal load gradually increasing from 0 to 100 mN and (c) friction force and (d) coefficient of friction of skin versus scratch time for normal load gradually increasing from 0 to 200 mN (scratch speed = 5 μm/s).

6.3 Microscratching under a linearly increasing normal load

In all previous tests, the normal load was kept constant during testing. Scratch experiments in which the load was linearly increased revealed significantly different skin friction and wear characteristics. Figure 6.6 shows representative friction force and coefficient of friction results from these experiments. Large friction fluctuations were observed with the increase of the normal load in the ranges 0–100 mN (Figures 6.6(a) and 6.6(b)) and 0–200 mN (Figures 6.6(c) and 6.6(d)). These abrupt changes in skin friction indicate the evolution of tissue damaging events. Indeed, cross-sectional histology images

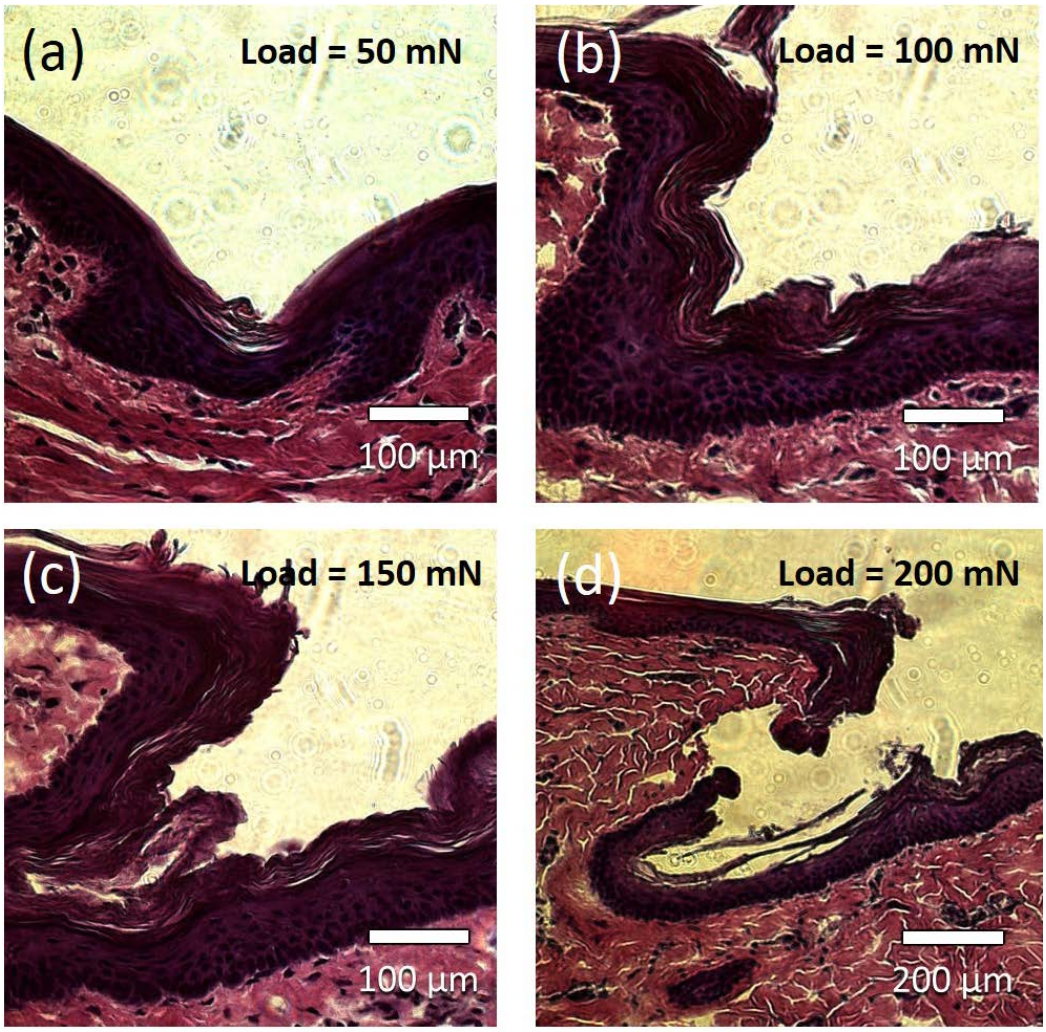

Figure 6.7 Cross-sectional histology images of scratched skin for normal load equal to (a) 50, (b) 100, (c) 150, and (d) 200 mN (scratch speed = 5 µm/s). In these experiments, the normal load was linearly increased from 0 to 200 mN at a rate of 1 mN/s.

demonstrated extensive damage in the epidermis as the load was increased at a rate of 1 mN/s. The images shown in Figure 6.7 correspond to some of the friction peaks shown in Figures 6.6(c) and 6.6(d). Thus, the abrupt peaks encountered at 50, 100, 150, and 200 ms (Figures 6.6(c) and 6.6(d)), corresponding to a normal load of 50, 100, 150, and 200 mN, may be correlated to cohesive failure and delamination in the stratum corneum (Figure 6.7(a)), removal of the stratum corneum and tearing of the exposed cellular epidermis (Figure 6.7(b)), evolution of gross plastic shearing in the cellular epidermis (Figure 6.7 (c)), and rupture of the epidermis resulting in the exposure of the dermis (Figure 6.7(d)).

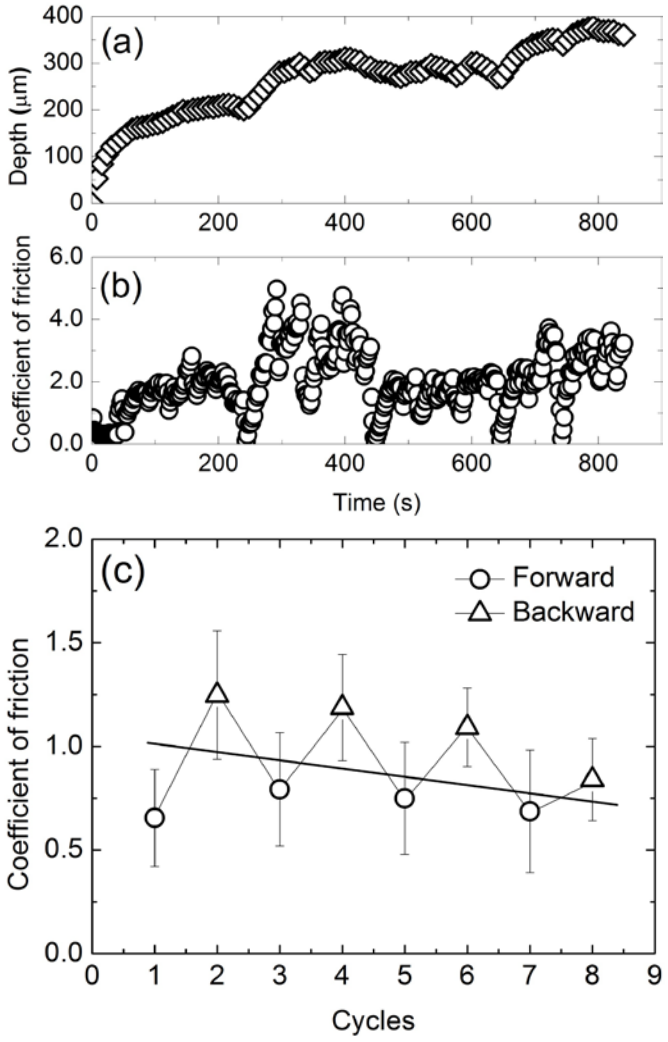

Figure 6.8 (a) Scratch depth and (b) coefficient of friction of skin versus scratch time for four sequential scratch cycles (two forward and two backward) and (c) coefficient of friction of skin versus sequential forward-backward scratch cycles (normal load = 20 mN; scratch speed = 5 μm/s; cycle duration = 200 s).

A comparison of Figures 6.6 and 6.7 with Figures 6.2 and 6.5 shows higher friction, more pronounced friction fluctuations, significantly more severe damage in the epidermis, and, interestingly, different wear mechanisms for scratching under increasing normal load than under constant load. It appears that the increase of the scratch load triggered a peel-off wear process, resulting in layer-by-layer removal of the epidermis as opposed to adhesion and plowing for constant scratch load. Thus, in the case of constant scratch load, the probe tip instantaneously punched through the skin, resulting in plowing and tearing

of the tissue upon subsequent scratching, whereas skin scratching under a linearly increasing load promoted a cutting process, leading to layer-by-layer tissue wear and significant friction fluctuations attributed to the shearing and breaking-off of tissue material.

6.4 Microscratching under a cyclic normal load

In addition to unidirectional scratching, experiments were also performed in reciprocating (cyclic) mode of scratching. In these experiments, the loaded tip was repetitively traversed back and forth over the same area on the skin surface. The duration of each scratch cycle, defined as the forward or backward traversal of the tip, was fixed at 200 s. Because of the much higher damage caused by cyclic scratching, the normal load in these tests was fixed at 20 mN. Figures 6.8(a) and 6.8(b) show representative results of the depth and coefficient of friction obtained from a cyclic scratch test. While the depth varies almost linearly with time, which is typical of adhesive and abrasive wear (Rabinowicz, 1995), the coefficient of friction rises and exhibits significant fluctuations at the onset of each backward cycle. In addition, backward scratching consistently produced higher friction, as confirmed by the statistical data of the coefficient of friction shown in Figure 6.8(c) (n = 5). The difference between forward and backward sliding friction gradually decreased with the increase of scratch cycles. This trend is attributed to progressive surface smoothening and the decrease of the contact pressure due to the increase of the surface conformity with scratch cycles.

Tissue transfer to the back of the tip during forward scratching (Figure 6.9(b)) with more worn tissue transferring during backward scratching (Figure 6.9(c)) is another reason for the trend observed in Figure 6.8(c). The built-up of tissue material at the tip front during backward sliding may have contributed to the higher friction and marked friction fluctuations observed in Figure 6.8(b). It is likely that this material built-up effect became secondary with the increase of the surface conformity in subsequent scratch cycles.

Figure 6.10 shows cross-sectional histology images that provide insight into skin damage due to low-load cyclic scratching. In the early stage of cyclic scratching, damage is mainly due to deformation in the dermis, resulting in the formation of a residual scratch (Figure 6.10(a)) without significant loss of tissue (surface plasticity), similar to unidirectional scratching (Figure 6.5(a)). However, the increase of plastic deformation in the dermis with scratch cycles compromised the integrity of the stiff and hard stratum corneum, which begun to exhibit cohesive failure (Figure 6.10(b)). The increase of the wear scar dimensions with further cyclic scratching led to extensive cohesive failure and the detachment of stratum corneum form the cellular epidermis (Figure 6.10(c)), followed by the removal of stratum corneum and severe tearing in the cellular epidermis (Figure 6.10(d)). Thus, low-load cyclic scratching led to the formation of wider wear scar and skin damage similar to that observed in high-load unidirectional scratching.

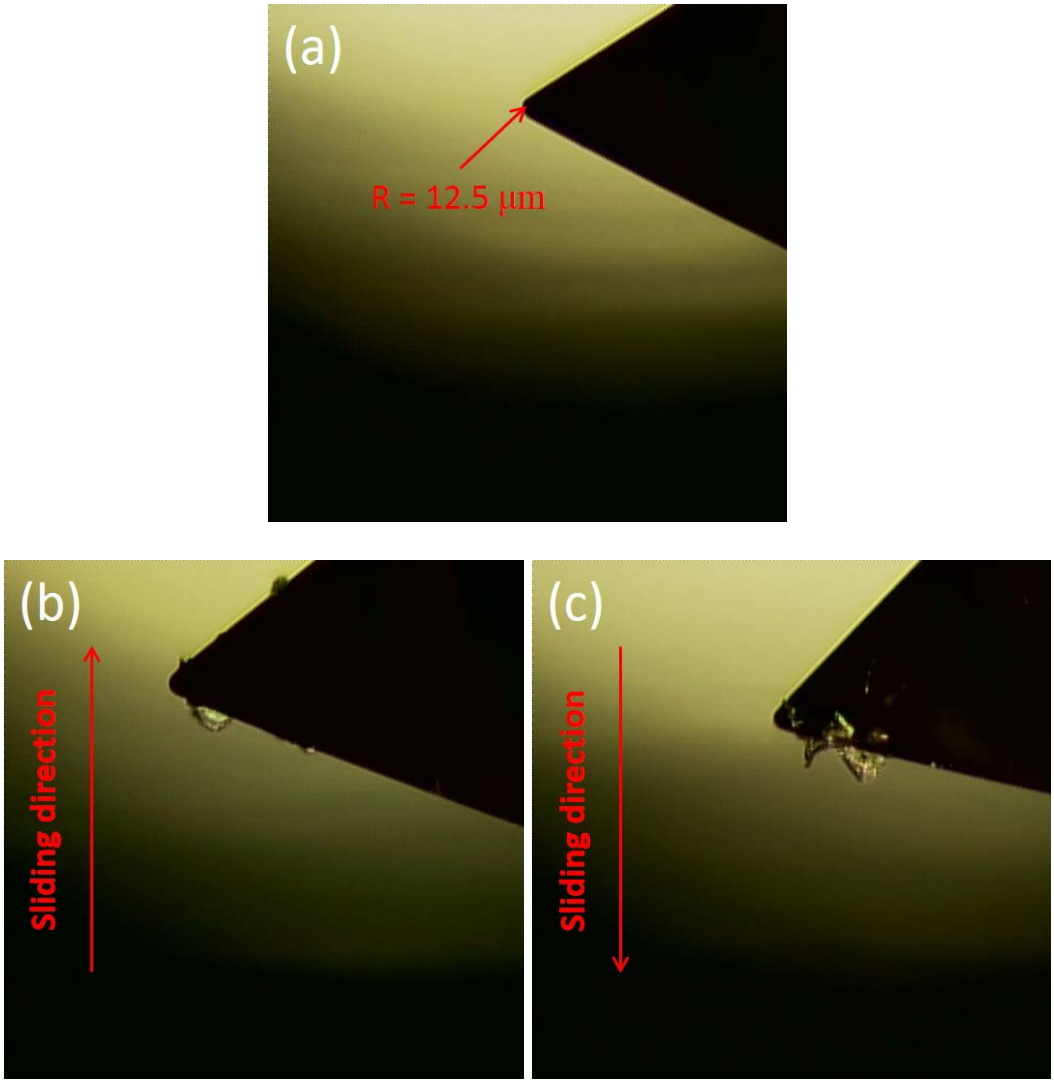

Figure 6.9 Optical microscope images of microprobe tip obtained (a) before testing and after (b) forward and (c) backward scratching (normal load = 20 mN; scratch speed = 5 μm/s; cycle duration = 200 s).

6.5 Summary

Skin deformation, friction, and wear were examined in the context of results obtained from *in vitro* micromechanical testing, optical microscopy, and histology analysis using porcine samples. Based on the presented results and discussion, the following main

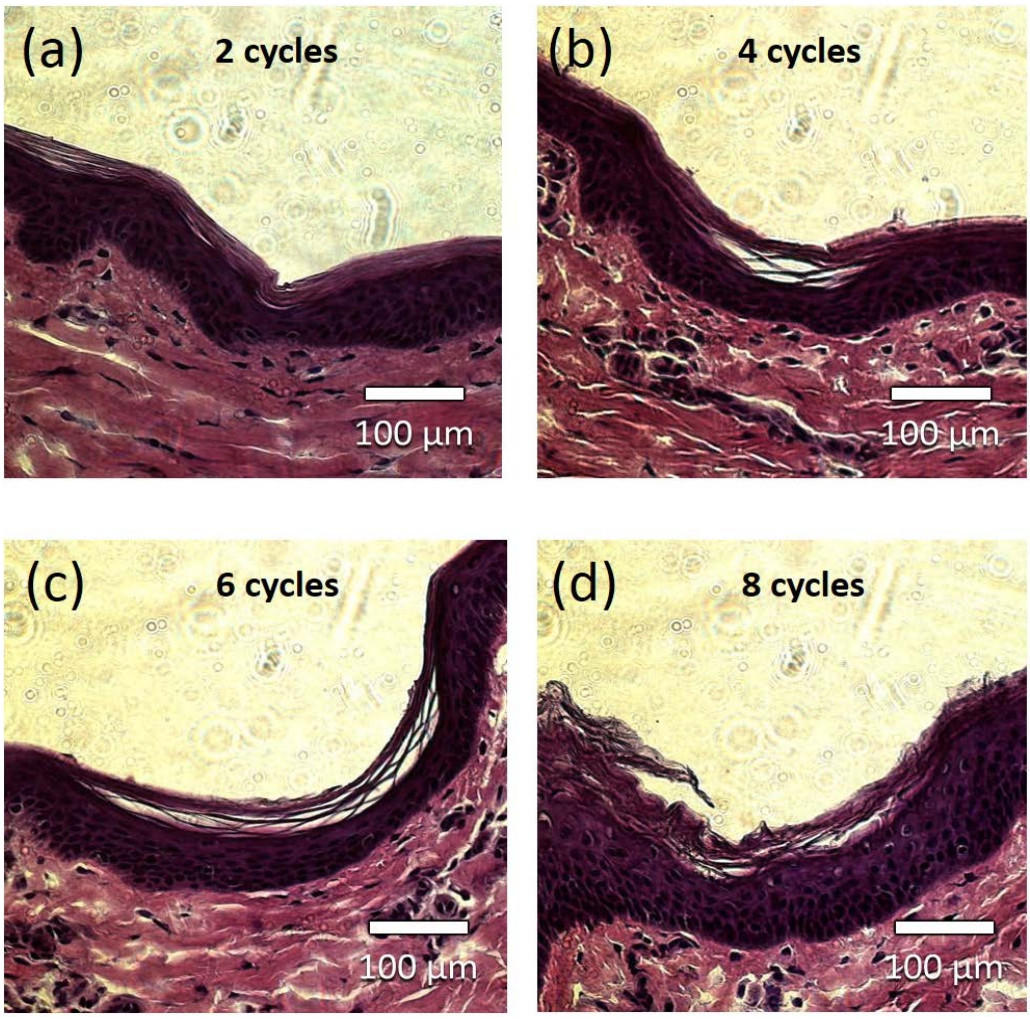

Figure 6.10 Cross-sectional histology images of cyclically scratched skin obtained after (a) 2, (b) 4, (c) 6, and (d) 8 sequential forward/backward scratch cycles (normal load = 20 mN; scratch speed = 5 μm/s; cycle duration = 200 s).

conclusions can be drawn.

(1) Time-independent deformation of the epidermis at steady-state scratching was largely due to the hard stratum corneum, whereas time-dependent deformation of dermis was due to its intrinsic viscoelastic behavior.

(2) Epidermis friction increased with the normal load due to the enhancement of the adhesion and plowing friction mechanisms, while dermis friction decreased with the increase of normal load due to the effect of squeeze film lubrication.

(3) A transition from mild to severe skin damage was encountered with increasing normal load in unidirectional scratching, characterized by a transition from surface plasticity/plowing (sinking) to bulk cohesive damage, delamination, and rupture.

(4) Unidirectional scratching under a linearly increasing normal load produced significantly higher and more fluctuating friction and more severe wear than constant-load unidirectional scratching; most notably, large friction fluctuations due to cohesive damage, delamination, and removal of the stratum corneum, extensive plastic shearing in the cellular epidermis, and eventual exposure of the dermis. The intensification of friction and wear due to a gradually increasing scratch load were attributed to the development of a peel-off wear process, resulting in layer-by-layer tissue removal as opposed to adhesion, plowing, and tearing in constant-load scratching.

(5) Reciprocating (cyclic) scratching revealed skin friction anisotropy. Consistently lower friction was observed during forward than backward scratching; however, the difference tended to decrease with increasing scratch cycles because of surface smoothening and the decrease of the mean contact pressure due to the enhancement of the surface conformity.

(6) Low-load cyclic scratching resulted in wider wear scars and skin damage similar to that observed in high-load unidirectional scratching. During the initial scratch cycles, damage was controlled by deformation in the dermis, resulting in a residual scratch mark (plowing) without notable loss of tissue. However, the increase of plasticity in the dermis with the scratch cycles led to cohesive failure in the stratum corneum and its eventual detachment form the cellular epidermis, resulting in severe tearing in the cellular epidermis.

Chapter 7. Summary

This dissertation is concerned with the mechanical properties of individual skin layers. One-way ANOVA analysis revealed insignificant differences in the mechanical properties of stratum corneum, dermis, and skin of different porcine breeds and randomly selected samples of each breed, indicating that the measured mechanical properties were independent of breed, sample selection, and test order. Mechanical behavior of individual skin layers and whole skin multilayer were studied in the light of nano/microindentation experiments, performed with relatively sharp and blunt indenters, and indentation mechanics analysis.

To avoid biasing of the measurements by the high surface roughness (200–300 nm) of the skin samples, nanoindentation measurements were obtained with a sharp (1 μm radius) indenter for a maximum contact depth larger than 500 nm. Because of the less significant roughness effect on the measurements obtained with a blunt (20 μm radius) indenter, reliable measurements were obtained for a smaller range of maximum contact depth. However, these measurements were influenced by the high compliance of the viable epidermis. This problem was overcome by using a curve-fitting approach and extrapolating the fitted curve into the low range of maximum contact depth. Using this approach, the reduced elastic modulus of stratum corneum measured with the blunt indenter (0.80 GPa) was found to be very close to the direct measurement obtained with the sharp indenter (0.87 GPa). The reduced elastic modulus of stratum corneum measured in this study is in good agreement with the results of previous studies (Park and Baddiel, 1972; Nicolopoulos et al., 1998). Using the same curve-fitting/extrapolation approach, the skin hardness was estimated to be 1.43 MPa, which is significantly lower than the hardness of stratum corneum (15.6 MPa) and slightly higher than the hardness of viable epidermis (1.30 MPa). This is attributed to the dominant effect of the significantly thicker and softer viable epidermis and dermis than stratum corneum.

The lower reduced elastic modulus (1.91 MPa) and hardness (0.85 MPa) of dermis than those of stratum corneum by about three and one orders of magnitude, respectively, provides an explanation for the sharp decrease of the mechanical properties of skin with increasing maximum contact depth. For small contact depths, the mechanical properties of skin are controlled by those of stratum corneum, whereas for relatively large contact depths, the mechanical behavior of skin is dominated by the viable epidermis and dermis properties. Thus, the loading response of skin due to shallow indentation is governed by the mechanical behavior of stratum corneum, while the unloading response of skin subjected to deep indentation is mostly influenced by the elastic behaviors of the viable

epidermis and dermis.

Time-dependent deformation of individual skin layers was another major objective of this dissertation. The evolution of deformation in stratum corneum, dermis, and skin was tracked in terms of the creep strain measured under constant maximum load (hold period) and varying loading rate (or depth rate). Stratum corneum demonstrated practically time independent deformation and a gradual decrease in elastic contact stiffness with increasing depth distance. Dermis exhibited viscoelastic deformation, which strongly affected the time-dependent deformation of skin. Dermis viscoelasticity and elastic contact stiffness showed a nonlinear dependence on maximum load applied during the hold period and depth rate (indentation speed), respectively. Skin stiffness increased with load (penetration depth), showing a transition from a low stiffness typical of the dermis to a high stiffness approaching that of stratum corneum. Histology and experimental measurements led to the development of a conceptual deformation model, which explains skin viscoelastic behavior under constant load (creep) and zero load (stress relaxation) conditions. It was shown that skin deformation is controlled by the mechanical behavior of dermis (light loads), deformation in the stratum corneum (intermediate loads), and removal (cohesive and interfacial failure) of the stratum corneum and cellular epidermis in conjunction with significant fluid loss from the dermis (high loads).

Another major goal of this work was the deformation and wear characteristics due to microprobe scratching. Skin deformation, friction, and wear were examined in the context of results obtained from *in vitro* micromechanical testing, optical microscopy, and histology analysis using porcine samples. Time-independent deformation of the epidermis at steady-state scratching was largely due to the hard stratum corneum, whereas time-dependent deformation of dermis was due to its intrinsic viscoelastic behavior. Epidermis friction increased with normal load due to the enhancement of the adhesion and plowing friction mechanisms, while dermis friction decreased with the increase of normal load due to the effect of squeeze film lubrication.

A transition from mild to severe skin damage was encountered with increasing normal load in unidirectional scratching, characterized by a transition from surface plasticity/plowing (sinking) to bulk cohesive damage, delamination, and rupture. Unidirectional scratching under a linearly increasing normal load produced significantly higher and more fluctuating friction and more severe wear than constant-load unidirectional scratching; most notably, large friction fluctuations due to cohesive damage, delamination, and removal of the stratum corneum, extensive plastic shearing in the cellular epidermis, and eventual exposure of the dermis. The intensification of friction and wear due to a gradually increasing scratch load were attributed to the development of a peel-off wear process, resulting in layer-by-layer tissue removal as opposed to adhesion, plowing, and tearing in constant-load scratching.

Reciprocating (cyclic) scratching revealed skin friction anisotropy. Consistently lower friction was observed during forward than backward scratching; however, the difference tended to decrease with increasing scratch cycles because of surface smoothening and the decrease of the mean contact pressure due to the enhancement of

the surface conformity. Low-load cyclic scratching resulted in wider wear scars and skin damage similar to that observed in high-load unidirectional scratching. During the initial scratch cycles, damage was controlled by deformation in the dermis, resulting in a residual scratch mark (plowing) without notable loss of tissue. However, the increase of plasticity in the dermis with scratch cycles led to cohesive failure in the stratum corneum and its eventual detachment form the cellular epidermis, resulting in severe tearing in the cellular epidermis.

The results of this dissertation provide insight into the mechanical and tribological properties of skin, in particular the contributions of individual skin layers to overall skin behavior. This information is of particular importance to minimally invasive procedures relying on effective penetration of the stratum corneum, such as transdermal drug delivery, local tissue and gene delivery, and blood or interstitial fluid sampling using microneedle-based procedures.

Bibliography

Adams, M.J., Briscoe, B.J., and Johnson, S.A., 2007. Friction and Lubrication of Human Skin. Tribol. Lett. 26, 239–253.

Agache, P.G., Monneur, C., Leveque, J.L., De Rigal, J., 1980. Mechanical properties and Young's modulus of human skin in vivo. Arch. Dermatol. Res. 269, 221–232.

Agner, T., Serup J., 1990. Sodium lauryl sulphate for irritant patch testing – a dose-response study using bioengineering methods for determination of skin irritation. J. Invest. Dermatol. 95, 543–547.

Akers, C. W. A., 1985. Measurements of Friction Injuries in Man. Am. J. Ind. Med., 8, 473–481.

Alexander, H., Cook, T.H., 1977. Accounting for natural tension in the mechanical testing of human skin. J. Invest. Dermatol. 69, 310–314.

Archer, C.B., 2010. Functions of the skin. In Rook's Textbook of Dermatology, Eighth edition, edited by Burns, D.A., Breathnach, S.M., Cox, N.H., Griffiths, C.E.M., Willey-Blackwell, Oxford, UK, Chapter 3, pp. 1–11.

Armstrong, T. J., 1985. Mechanical Considerations of Skin in Work. Am. J. Ind. Med. 8, 463–472.

Auriol, F., Vaillant, L., Machet, L., Diridollou, S., Lorette G., 1993. Effects of short-time hydration on skin extensibility. Acta Dermato-Venereologica 73, 344–347.

Bader, D. L., Bowker, P., 1983. Mechanical characteristics of skin and underlying tissues in vivo. Biomaterials 4, 305–308.

Barry, B.W., 1991. Lipid-protein-partitioning theory of skin penetration enhancement. J. Controlled Release 15, 237–248.

Berardesca, E., Borroni, G., Gabba, P., Borlone, R., Rabbiosi, G., 1986. Evidence for elastic changes in aged skin revealed in an in vivo extensometric study at low loads. Bioeng. and the Skin 2, 261–270.

Bhushan, B., Wei, G., and Haddad, P., 2005. Friction and Wear Studies of Human Hair and Skin. Wear, 259, 1012–1021.

Bouten, C.V., Oomens, C.W., Baaijens, F.P., Bader, D.L., 2003. The etiology of pressure ulcers: skin deep or muscle bound. Arch. Phys. Med. Rehabil. 84, 616–619.

Brazzelli, V., Borroni, G., Vignoli, G.P., Rabbiosi, G., Cavagnino, A., Berardesca, E., 1994. Effects of fluid volume changes during hemodialysis on the biophysical parameters of the skin. Dermatology 188, 113–116.

Candi, E., Schmidt, R., Melino, G. 2005. The cornified envelope: a model of cell death in the skin. Nature Rev.: Molec. Cell Biol. 6, 328–340.

Clemente, C.D., 1985, Gray's Anatomy. Lea & Febiger, Philadelphia.

Comaish, S., and Bottoms, E., 1971. The Skin and Friction: Deviations from Amonton's Laws, and the Effects of Hydration and Lubrication. Br. J. Dermatol., 84, 37–43.

Cooper, E.R., Missel, P.J., Hannon, D.P., Albright G.B., 1985. Mechanical properties of dry, normal, and glycerol-treated skin as measured by the gas-bearing electrodynamometer. J. Soc. Cosmet. Chem. 36, 335–348.

Cua, A.B., Wilhelm, K.-P., and Maibach, H.I., 1990. Frictional Properties of Human Skin: Relation to Age, Sex and Anatomical Region, Stratum Corneum Hydration and Transepidermal Water Loss. Br. J. Dermatol., 123, 473–479.

Cua, A.B., Wilhelm, K.-P., Maibach, I.H., 1990. Elastic properties of human skin: relation to age, sex, and anatomical region. Arch. Dermatol. Res. 282, 283–288.

Davis, S.P., Landis, B.J., Adams, Z.H., Allen M.G., Prausnitz, M.R., 2004. Insertion of microneedles into skin: measurement and prediction of insertion force and needle fracture force. J. Biomech. 37, 1155–1163.

Delalleau, A., Josse, G., Lagarde, J.M., Zahouani, H., Bergheau, J.M., 2006. Characterization of the mechanical properties of skin by inverse analysis combined with the indentation test. J. Biomech. 39, 1603–1610.

Derler, S., Schrade, U., and Gerhardt, L.-C., 2007. Tribology of Human Skin and Mechanical Skin Equivalents in Contact with Textiles. Wear, 263, 1112–1116.

Dikstein, S., Hartzshtark, A., Bercovici, P., 1984. The dependence of low-pressure indentation, slackness, and surface pH on age in forehead skin of women. J. Soc. Cosmet. Chem. 35, 221–228.

Diridollou, S., Berson, M., Vabre, V., Black, D., Karlsson, B., Auriol, F., Gregoire, J.M., Yvon, C., Vaillant, L., Gall, Y., Patat, F., 1998. An in vivo method for measuring the mechanical properties of the skin using ultrasound. Ultrasound Med. Biol. 24, 215–224.

Diridollou, S., Patat, F., Gens, F., Vaillant, L., Black, D., Lagarde, J.M., Gall Y., Berson M., 2000. In vivo model of the mechanical properties of the human skin under suction. Skin Res. Technol. 6, 214–221.

Elsner, P., Wilhelm, D., and Maibach, H.I., 1990. Frictional Properties of Human Forearm and Vulvar Skin: Influence of Age and Correlation with Transepidermal Water Loss and Capacitance. Dermatologica, 181, 88–91.

Falanga, V., Bucalo B., 1993. Use of a durometer to assess skin hardness. J. Am. Acad. Dermatol. 29, 47–51.

Finlay B., 1971. The torsional characteristics of human skin in vivo. Biomed. Eng. 6, 567–573.

Fischer-Cripps, A.C., 2004, Nanoindentation, Springer, New York.

Fry, P., Harkness, M.L.R., Harkness, R.D., 1964. Mechanical properties of the collagenous framework of skin in rats of different ages. Am. J. Physiol. 206, 1425–1429.

Geerligs, M., van Breemen, L., Peters, G., Ackermans, P., Baaijens, F., Oomens, C., 2011. *In vitro* indentation to determine the mechanical properties of epidermis. J. Biomech. 44, 1176–1181.

Gibson, T., Stark, H., Evans, J.H., 1969. Directional variation in extensibility of human skin *in vivo*. J. Biomech. 2, 201–204.

Glaser, A.A., Marangoni, R.D., Must, J.S., Beckwith, T.G., Brody, G.S., Walker, G.R., White, W.L., 1965. Refinements in the methods for the measurement of the mechanical properties of unwounded and wounded skin. Med. Electron. Biol. Eng. 3, 411–419.

Grahame, R., 1969. Elasticity of human skin *in vivo*. A study of the physical properties of the skin in rheumatoid arthritis and the effect of corticosteroids. Ann. Phys. Med. 10, 130–136.

Grahame, R., Holt, P.J.L., 1969. The influence of ageing on the in vivo elasticity of human skin. Gerontologia 15, 121–139.

Gunner, C.W., Hutton, W.C., Burlin T.E., 1979. The mechanical properties of skin *in vivo* – a portable hand-held extensometer. Br. J. Dermatol. 100, 161–163.

Haddad, Y.M., 1995, Viscoelasticity of engineering materials, Chapman & Hall, London, UK.

Hendriks, F.M., Brokken, D., Oomens, C.W.J., Bader, D.L., Baaijens, F.P.T., 2006. The relative contributions of different skin layers to the mechanical behavior of human skin in vivo using suction experiments. Med. Eng. Phys. 28, 259–266.

Jachowicz, J., McMullen, R., Prettypaul, D., 2007. Indentometric analysis of *in vivo* skin and comparison with artificial skin models. Skin Res. Technol. 13, 299–309.

Jee, T., and Komvopoulos, K., 2013. *In vitro* Measurement of the Mechanical Properties of Skin by Nano/microindentation Methods. J. Biomech. (submitted).

Kalis, B., De Rigal, J., Léonard, F., Lévêque, J.L., Riche, O., Le Corre, Y., De Lacharriere, O., 1990. *In vivo* study of scleroderma by non-invasive techniques. Br. J. Dermatol. 122, 785–791.

Kendall, M.A.F., Chong, Y.-F., Cock A., 2007. The mechanical properties of the skin epidermis in relation to targeted gene and drug delivery. Biomaterials 28, 4968–4977.

Khatyr, F., Imberdis, C., Vescovo, P., Varchon, D., Lagarde, J.-M., 2004. Model of the viscoelastic behaviour of skin *in vivo* and study of anisotropy. Skin Res. Technol. 10, 96–103.

Komvopoulos, K., Saka, N., and Suh, N.P., 1986. Plowing Friction in Dry and Lubricated Metal Sliding. ASME J. Tribol., 108, 301–313.

Kwiatkowska, M., Franklin, S.E., Hendriks, C.P., and Kwiatkowski, K., 2009. Friction and Deformation Behaviour of Human Skin. Wear, 267, 1264–1273.

Lanir, Y., Dikstein, S., Hartzshtark, A., Manny, V., 1990. In-vivo indentation of human skin. J. Biomech. Eng. 112, 63–69.

LaTorre, C., and Bhushan, B., 2005. Nanotribological Characterization of Human Hair and Skin Using Atomic Force Microscopy. Ultramicroscopy, 105, 155–175.

Leveque, J.L., de Rigal, J., Agache, P.G., Monneur, C., 1980. Influence of ageing on the in vivo extensibility of human skin at a low stress. Arch. Dermatol. Res. 269, 127–135.

Lu, W., Komvopoulos, K., 1999. Microstructure and nanomechanical properties of nitrogenated amorphous carbon thin films synthesized by reactive radio frequency sputtering. J. Appl. Phys. 85, 2642–2651.

McGrath, J.A., Uitto, J., 2010. Anatomy and organization of human skin. In Rook's Textbook of Dermatology, Eighth edition, edited by Burns, D.A., Breathnach, S.M., Cox, N.H., Griffiths, C.E.M., Willey-Blackwell, Oxford, UK, Chapter 3, 1–53.

Naylor, P.F.D., 1955. The Skin Surface and Friction. Br. J. Dermatol. 67, 239–248.

Nicolopoulos, C.S., Giannoudis, P.V., Glaros, K.D., Barbenel, J.C., 1998. In vitro study of the failure of skin surface after influence of hydration and preconditioning. Arch. Dermatol. Res. 290, 638–640.

Ohura, T., Sugihara, T., Honda, K., 1980. Postoperative evaluation in plastic surgery using the bio-skin tension meter. Ann. Plast. Surg. 5, 74–82.

Oliver, W.C., Pharr, G.M., 1992. An improved technique for determining hardness and elastic modulus using load and displacement sensing indentation experiment. J. Mater. Res. 7, 1564–1583.

Pailler-Mattei, C., Bec, S., Zahouani, H., 2008. In vivo measurements of the elastic mechanical properties of human skin by indentation tests. Med. Eng. Phys. 30, 599–606.

Park, A.C., Baddiel, C.B., 1972. Rheology of stratum corneum–I: a molecular interpretation of the stress-strain curve. J. Soc. Cosmet. Chem. 23, 3–12.

Park, J.H., Allen, Mark G., Prausnitz, Mark R., 2005. Biodegradable polymer microneedles: Fabrication, mechanics and transdermal drug delivery. J. Control. Release. 104, 51–66.

Parker, E.R., Rao, M.P., Turner, K.L., Meinhart, C.D., MacDonald, N.C., 2007. Bulk micromachined titanium microneedles. J. Microelectromech. S. 16, 289–295.

Peck, S.M., Glick, A.W., 1956. A new method for measuring the hardness of keratin. J. Soc. Cosmet. Chem. 7, 530–540.

Rabinowicz, E., 1995, Friction and Wear of Materials, 2nd ed., Wiley, New York.

Ridge, M.D., Wright, V., 1966a. The directional effects of skin. A bio-engineering study of skin with particular reference to Langer's lines. J. Invest. Dermatol. 46, 341–346.

Ridge, M.D., Wright, V., 1966b. Mechanical properties of skin: a bioengineering study of skin structure. J. Appl. Physiol. 21, 1602–1606.

Ridge, M.D., Wright, V., 1966c. Rheological analysis of connective tissue. A bio-engineering analysis of the skin. Ann. Rheum. Dis. 25, 509–515.

Salter, D.C., McArthur, H.C., Crosse, J.E., Dickens A.D., 1993. Skin mechanics measured *in vivo* using torsion: a new and accurate model more sensitive to age, sex and moisturizing treatment. Int. J. Cosmet. Sci. 15, 200–218.

Sanders, R., 1973. Torsional elasticity of human skin in vivo. Pflügers Arch. 342, 255–260.

Schmook, F.P., Meingassner, J.G., Billich, A., 2001. Comparison of human skin or epidermis models with human and animal skin in in-vitro percutaneous absorption. Int. J. Pharm. 215, 51–56.

Sivamani, R.K., Goodman, J., Gitis, N.V., and Maibach, H.I., 2003. Friction Coefficient of Skin in Real-Time. Skin Res. Technol. 9, 235–239.

Sivamani, R.K., Goodman, J., Gitis, N.V., and Maibach, H.I., 2003, Coefficient of Friction: Tribological Studies in Man – An Overview. Skin Res. Technol. 9, 227–234.

Sivamani, R.K., Wu, G.C., Gitis, N.V., and Maibach, H.I., 2003. Tribological Testing of Skin Products: Gender, Age, and Ethnicity on the Volar Forearm. Skin Res. Technol. 9, 299–305.

Sugihara, T., Ohura, T., Homma, K., Igawa H.H., 1991. The extensibility in human skin: variation according to age and site. Br. J. Plast. Surg. 44, 418–422.

Sulzberger, M.B., Cortese, T.A., Fishman, L., and Wiley, H.S., 1966. Studies on Blisters Produced by Friction. I. Results of Linear Rubbing and Twisting Technics. J. Invest. Dermatol. 47, 456–465.

Tang, B., Ngan, A.H.W., 2003. Accurate measurement of tip–sample contact size during nanoindentation of viscoelastic materials. J. Mater. Res. 18, 1141–1148.

Tang, W., and Bhushan, B., 2010. Adhesion, Friction and Wear Characterization of Skin and Skin Cream Using Atomic Force Microscope. Colloid Surf. B: Biointerf. 76, 1–15.

Veronda, D.R., Westmann, R.A., 1970. Mechanical characterization of skin–Finite deformations. J. Biomech. 3, 111–124.

Warren, R., Gartstein, V., Kligman, A.M., Montagna, W., Allendorf, R.A., Ridder, G.M., 1991. Age, sunlight, and facial skin: A histologic and quantitative study. J. Am. Acad. Dermatol. 25, 751–760.

Wilkinson, D.S., 1985. Dermatitis from Repeated Trauma to the Skin. Am. J. Ind. Med. 8, 307–317.

Yuan, Y., Verma, R., 2006. Measuring microelastic properties of stratum corneum. Colloids Surf. B: Biointerf. 48, 6–12.

Zhang, M., and Mak, A.F.T., 1999. *In Vivo* Friction Properties of Human Skin. Prosthet. Orthot. Int. 23, 135–141.

Zhou, J., Komvopoulos, K., 2006. Surface and interface viscoelastic behaviors of thin polymer films investigated by nanoindentation. J. Appl. Phys. 100, 114329.